Rheology of Filled and Unfilled Polyurethanes for Reactive Extrusion-Based Applications

by

John Page Reynolds

Dissertation submitted to the faculty of Virginia Polytechnic Institute and State University in partial fulfillment of the requirements for the degree of

DOCTOR OF PHILOSOPHY

In

Chemical Engineering

Michael J. Bortner, Chair

Christopher B. Williams

Blake N. Johnson

Stephen M. Martin

October 20, 2023

Blacksburg, VA 24061, USA

Keywords: rheology, high solids content, polyurethane, additive manufacturing, material extrusion, curing kinetics

Rheology of Filled and Unfilled Polyurethanes for Reactive Extrusion-Based Applications

John Page Reynolds

Abstract

Additive manufacturing (AM) is a form of production that directly processes raw materials into their final form by building the product in a layer-by-layer fashion. Numerous types of AM exist, including selective laser sintering (SLS) of polymeric powders, vat polymerization (VP) of low viscosity photocurable resins, and material extrusion (MatEx) of thermoplastic or high viscosity composite materials. Because of its ability to reduce material waste while printing complex geometries, AM has the potential to revolutionize the manufacturing industry for a diverse set of materials and products.

MatEx of thermoplastic feedstocks is most commonly performed using fused filament fabrication (FFF) – a form of melt extrusion. A solid filament is fed directly into a heated nozzle, where it melts onto a build bed before resolidifying in a matter of seconds. While this is the most common form of AM, especially among hobbyists, the material catalog is limited to thermoplastic polymers, and difficulties arise when fillers are introduced (e.g. reactions at elevated temperatures, clogging, disruption of polymer chain diffusion, and large increases in viscoelastic properties). To combat these challenges, direct ink write (DIW) AM extrudes highly viscous composites by applying pneumatic backpressure to a syringe, such that the material can be extruded in ambient conditions. This method enables processing of unreacted, thermosetting resins which have been filled with a large proportion of solid particulate fillers, called “highly filled” inks. The interparticle network formed from particle-particle interactions in the form of weak surface forces (e.g. Van der Waals forces) provides structural stability of the printed lines, such that they can sustain the weight of subsequent layers.

In the realm of DIW 3D printing material discovery and processing, there are currently three major challenges. First, the high shear region of the nozzle frequently disrupts the interparticle network through a de-agglomeration process, such that there is a finite timescale for the interparticle network to reestablish itself. During this timeframe, the deformation/reformation process causes printed lines to sag, which negatively impacts both print quality and mechanical properties. Second, printed parts require a post-processing step to develop adequate mechanical properties suitable for the final product. The kinetics of this cure process are extremely slow, often taking multiple days or weeks to reach completion. Third, high shear rheological characterization of highly filled inks is challenging because of the numerous artifacts of error associated with high shear testing environments (e.g. sample loss/edge fracture, slip, and large sample size requirements). A literature review in Chapter 2 outlines the most recent advances in highly filled polyurethane processing for DIW, with a particular focus on how interparticle network recovery – in the form of thixotropy – can be tailored using a variety of reactive inks.

The subsequent chapters of this dissertation address these challenges by systematically downselecting reactive inks appropriate for highly filled DIW extrusion while introducing numerous process relevant rheological protocols. An initial discussion in Chapter 3 covers the potential drawbacks of thermoplastic polyurethane (TPU) processing as it relates to industrial scale melt extrusion. Specifically, multiple side reactions and degradation processes are identified for a variety of TPU manufacturers. Such reactions elicit undesirable solid-like particulate buildup within the extrusion line, and the impacts/causes of these reactions are quantified using rheological criteria. These protocols offer evidence that differences in processability can arise not just between manufacturers, but also between lots of TPU from the same manufacturer.

To address these concerns, Chapter 4 offers an alternative form of polyurethane processing in the form of a thermosetting reaction between hydroxyl-terminated polybutadiene (HTPB) and isophorone diisocyanate (IPDI). When uncatalyzed at room temperature, full conversion takes place over the course of multiple weeks which necessitates an accelerated kinetic analysis. Hence, a combination of chemorheological and spectroscopic methods are used to rapidly probe for changes in isocyanate reactivity using limited sample quantities, which substantiate the advantages and disadvantages of chemorheology and spectroscopy in the context of curing studies.

While this synthetic pathway provides mechanical properties appropriate for the final printed product, a major concern is retention of green body strength post deposition. In order to maintain the shape of printed beads, ultraviolet (UV) light can be shined *in-situ* onto the nozzle of a DIW printhead, which actively cures the urethane acrylate ink through free radical polymerization. This technique, termed UV-assisted direct ink write (UV-DIW), assists recovery of the interparticle network. A novel rheological method proposed in Chapter 5, termed the "UV-assisted three interval thixotropy test" (UV-3ITT), quantifies the contribution of UV light towards structural stability and printability. This is accomplished by applying stepwise changes in strain on a torsional photorheometer, optionally applying UV light in the third interval, and then quantifying the contribution of UV light towards process-relevant recovery parameters. Resultingly, the threshold of solid particulate fillers required for UV light to improve print fidelity is determined.

While most discussions revolve around torsional rheology, this method has one major drawback: it cannot probe the high shear properties of high solids content materials due to sample loss/edge fracture during steady shear measurement. Capillary rheometers are able to probe the viscosity profiles of highly filled materials in high shear environments, but the cost of the device

and the sample requirements are burdensome. To resolve this challenge, the “microcapillary rheometer” is developed in Chapter 6 using common laboratory equipment at a fraction of the cost of a full-scale capillary rheometer, which enables rapid characterization of high solids content materials at extrusion-relevant conditions while exploiting small sample quantities. This study illustrates the accuracy and precision of the microcapillary rheometer when comparing the high shear properties of several highly filled systems to the full-scale capillary rheometer. Results highlight that application of the Bagley and Weissenberg-Rabinowitsch corrections is possible using this novel device, which facilitates calculation of true shear viscosity of high solids content systems. The limited sample requirement facilitates characterization of novel or potentially hazardous materials in a much safer, efficient manner, which accelerates material discovery while improving safety standards.

Rheology of Filled and Unfilled Polyurethanes for Reactive Extrusion-Based Applications

John Page Reynolds

General Audience Abstract

Subtractive manufacturing technologies, which reduce raw materials down from their bulk state into a final product, make up a significant portion of the manufacturing sector today due to the convenience and ease of material processing. Some of the most common forms of subtractive manufacturing include lathing, milling, cutting, drilling, and grinding; these methods are applicable for a diverse set of materials ranging from metals to plastics. By the nature of this process, subtractive manufacturing yields substantial material waste, while limiting the complexity of a final product's design. To combat these unintended consequences, a novel form of production termed additive manufacturing (AM) has grown dramatically in the past several decades. AM directly processes raw materials into their final form which reduces material waste while enabling complex geometries to be "printed." Although there are numerous types of additive manufacturing, the most common forms utilize material extrusion, whereby the raw material is deposited through a nozzle and stacked in a layer-by-layer fashion onto a build bed, thus constructing a final product.

For materials that melt and flow at elevated temperatures (i.e. thermoplastic materials), fused filament fabrication (FFF) is ideal since a solid filament can be fed into a heated nozzle, melted onto a build bed, and then quickly re-solidified. However, many polymers do not melt at elevated temperatures, and instead degrade; these materials are termed "thermosetting." To print these materials, unreacted thermosetting precursors, which are filled with a large proportion of solid fillers ("highly filled inks"), can be extruded by applying pneumatic back pressure to a syringe at ambient conditions. The process of extruding these materials layer-by-layer describes the direct ink write (DIW) technique.

The solid particulate fillers form structural “networks” due to weak electrostatic forces on the surface of the fillers. These forces provide structural stability and enable the printed lines to hold the weight of subsequent layers. Unfortunately, the high-pressure region of the nozzle disrupts this network, causing the printed lines to sag over time. This effect can be reduced by actively applying ultraviolet (UV) light onto the nozzle during extrusion, which helps to hold the particles in place by curing the resin, thus increasing the capacity for a line to sustain the weight of subsequent layers. This form of material extrusion is termed UV-assisted direct ink write (UV-DIW). Because UV light only partially cures the material during prints, a separate, slower thermosetting reaction can occur as the material rests in an oven or in ambient conditions, which completely cures the printed part and provides sufficient mechanical properties. The combination of UV-curable resins, thermosetting resins, and sufficiently large amounts of solid particulate fillers for material extrusion describes the dual-cure nature of this highly filled UV-DIW process.

To understand the curing patterns, flow behavior, and the amount of structural deformation that occurs within the nozzle, rheology becomes a powerful characterization tool. This branch of physics deals with the deformation and flow of matter ranging from simple fluids to complex polymer melts. As such, it is possible to probe reaction progress (chemorheology), structural deformation/reformation (thixotropy), and high-shear regimes representative of the DIW process.

The research contained within this dissertation provides a holistic understanding of the overlap between rheology and DIW material extrusion for dual-reactive materials. This process begins by evaluating challenges during melt extrusion of thermoplastic polyurethane while quantifying the rate of degradation side reactions. An alternative form of polyurethane synthesis in the form of a thermosetting reaction is then introduced, whereby the reaction progress is evaluated using both rheological and spectroscopic techniques. Next, a novel rheological protocol

is introduced which can predict the structural deformation/reformation of an ink during UV-DIW. This research concludes by proposing a downscaled version of the high-shear capillary rheometer which requires only several grams of material in contrast to the dozens of grams required for full-scale capillary rheometry. In essence, the work presented here rapidly evaluates the complex flow behavior and cure progression of various materials relevant for extrusion processes by utilizing limited sample quantities, thus preserving valuable resources while improving the economics of material discovery.

Acknowledgments

I want to first and foremost thank my research advisor Dr. Michael Bortner for his guidance, support, and encouragement during the course of my Ph.D. He has consistently motivated me to push the boundaries of what I think is possible in my career while affirming my abilities as a researcher, leader, and academic. The scholarly, social, and professional communities he has fostered around him do not go unnoticed. In addition, I greatly appreciate the time and expertise granted by my committee members Dr. Christopher Williams, Dr. Blake Johnson, and Dr. Steven Martin. They have created an environment that enables students to succeed through high-level scientific discussion, while also providing valuable connections throughout the polymer science and engineering community.

I would like to also acknowledge the multiple research laboratories and collaborators who were essential to my success. The Polymer Composite and Materials Laboratory, the DREAMS laboratory, the Schultz group, and the Long group have all aided me greatly throughout these years. My collaborators at the Army Research Laboratory have also continually provided excellent scientific insight, and I thank them for their gracious financial support of my doctoral degree. While there are dozens of colleagues I wish to thank, two individuals in particular were essential in my research. Dr. Arit Das and Dr. Danny Rau, you have acted as some of my greatest mentors and provided such a positive learning atmosphere since the first time we interacted.

Additionally, I want to acknowledge everyone in the jiu jitsu community who has provided me with an outlet to step away from my research for a few hours a day. My training partners, teammates, and second families at Triple Threat Combat Sports and Team Mannon have enabled me to become confident both as a student and instructor. You all have taught me to be proud of who I am both on and off the mat.

I also want to thank my best friend, wife, and love of my life, Abbey Reynolds. You have advocated for me and lifted me up during the toughest moments of my life. Your passion to help others, willingness to engage in challenging conversations, and self-confidence is absolutely contagious. This dissertation is a product of all the ways you have bettered me.

Of course, I also have to acknowledge Titus "Bubbas" Reynolds. He has brought so much joy to life and allowed me to practice hours of oral presentations during our daily walks.

Finally, none of this would have been possible without the support of my parents Cathy and Scott Reynolds, who have been there for me through every stage of life. From the moment I began my chemical engineering endeavors at University of Delaware, to my dissertation defense at Virginia Tech, you have guided me towards success. I am forever thankful to have you both.

"It's a great day to be a Blue Hen!" and "Let's go Hokies!"

Format of Dissertation

Chapter 3 of this dissertation is presented as a scientific publication currently in progress for submission. Chapter 3 is also a co-first authored publication, and thus some material is altered, excluded, or relocated to the supplementary information to ensure limited overlap between each author's respective dissertation. Chapter 4 of this dissertation is presented as a scientific publication currently under review. Chapter 5 of this dissertation is presented as a peer-reviewed publication, reprinted from its respective journal with permission. Chapter 6 is presented as a scientific publication currently in progress for submission. Each chapter contains individual backgrounds, experimental setups, results, discussions, and conclusions.

Table of Contents

List of Figures

List of Tables

Chapter 1

Introduction

1. Introduction

1.1 Origins/Motivation for High Solids Content 3D Printing & Rheology

Additive manufacturing (AM), colloquially known as 3D printing, has roots dating back to the late 1800s where it was most famously used for topography [1]. It took nearly a century for modern day applications of this technology to arise, specifically at the Battelle Memorial Institute where photopolymerization of 3D objects was conceived in the 1960s [2]. This event marked a turning point for additive manufacturing technologies by introducing stereolithography (SLA), whereby materials are built layer-by-layer using selective curing of low viscosity, photocurable resins. Given the fact that fused deposition modeling (also known as fused filament fabrication, FFF) is one of the most popular forms of AM at the hobbyist level today, it might come as a surprise that SLA was the first commercially available AM method starting in 1987; it wasn't until 1991 that FFF became fully commercialized [2]. Furthermore, photocurable, high viscosity pastes were not even conceived until 2001 [2].

The strong demand to build complex geometries using a wide range of materials has prompted numerous modern day adaptations of these AM techniques [3]. For example, sintering of polymeric/metallic powders via high energy beams is possible through powder bed fusion, sheet lamination is enabled with ultrasonic welding, and liquid binding of powder-based polymers has facilitated binder jetting AM technologies. For highly viscous and/or colloidal systems, however, direct ink write (DIW) additive manufacturing dominates the field due to its ability to print inks with viscosities ranging from 1-1,000,000 cPs [4]. This processing range is permitted because of the pressure driven design, where (typically) a pneumatic piston dispenses the material at a given rate, which facilitates 3D printing of a product layer-by-layer [5]. Novel approaches to DIW AM

are rapidly evolving, including screw-based designs and multi-axis robot-assisted technologies [6, 7]. As a result of these advancements, DIW has found use in the fields of biology, construction, ceramics, energetics, and food [8-12].

The potential for scientific advancement in this area is expansive; exploration of novel materials, testing protocols, and instrumentation is highly sought after [8, 13]. As the need for material selection grows, so do the technologies required for processing. The demand to additively manufacture unreacted, non-thermoplastic materials – typically in the form of polymer precursors – has introduced a variety of DIW techniques. For example, thermal crosslinking, UV crosslinking, ambiently reactive, ionizable, hydratable, and multi-cure approaches are some of the most notable pathways for additively manufacturing polymer precursors [14-19].

Inclusion of solid fillers at volume percentages approaching the max packing fraction (i.e. "highly filled" systems) is especially important when tailoring the rheological properties necessary for printability [20, 21]. In addition, the end-use product may require large loading levels of solid filler for application-based needs, thus driving a need for AM of highly filled inks [22]. At these loading levels, several rheological phenomena occur such as yield stress formation, shear thinning, and thixotropy [23]. These behaviors appear due to interparticle network formation/deformation as a result of weak surface forces (e.g. Van der Waals forces, hydrostatic forces, and interparticle friction) [23]. The agglomeration/de-agglomeration process during high-shear regimes (i.e. in the nozzle of the printer) contributes significantly to interparticle network disruption [20]. Thus, rheology as a tool for establishing material down-selection, printability, and novel cure patterns has become an active field of research for polymer scientists and engineers [21, 24].

1.2 Research Objectives

The research questions and hypotheses presented here aim to characterize a variety of filled and unfilled polyurethanes in terms of applicability for material extrusion additive manufacturing. The core focus is understanding 1) the potential challenges when processing thermoplastic polyurethanes for AM/extrusion, 2) the use of rheology for tracking cure progress in thermosetting polyurethane matrix materials, 3) printability criteria of reactive, highly filled polyurethane precursors, and 4) novel tools for testing high-shear processes in reduced quantities. These goals are summarized by the following research questions/hypotheses:

1) Rapid chemorheological screening protocols can be established such that undesirable extrusion induced morphological changes of PTMO-based TPUs can be predicted over a short timeframe.
2) Chemorheology measurements can enable an accelerated kinetic analysis of multi-day crosslinking reactions via rheokinetic modeling, which facilitates prediction of processability timeframes for slow-reacting polyurethanes.
3) Rheological methods to predict printability and accelerate material discovery for ultraviolet-assisted material extrusion inks, using stepwise changes in strain during photorheology experiments, can quantify the contributions of 1) filler concentration and 2) *in-situ* UV light towards print height/quality improvements.
4) A low-cost version of the capillary rheometer can be developed to enable rapid, high-shear characterization of high solids content inks, while exploiting small material quantities.

1.3 References

[1] W. Gao, Y. Zhang, D. Ramanujan, K. Ramani, Y. Chen, C.B. Williams, C.C. Wang, Y.C. Shin, S. Zhang, P.D. Zavattieri, The status, challenges, and future of additive manufacturing in

engineering, Computer-Aided Design 69 (2015) 65-89. https://doi.org/10.1016/j.cad.2015.04.001.
[2] T. Wohlers, T. Gornet, History of additive manufacturing, Wohlers report 24 (2015) 118.
[3] S.A. Adekanye, R.M. Mahamood, E.T. Akinlabi, M.G. Owolabi, Additive manufacturing: the future of manufacturing, Addit. Manuf. 709 (2017) 715. https://doi.org/10.17222/mit.2016.261.
[4] I. Gibson, D. Rosen, B. Stucker, M. Khorasani, Direct write technologies, Additive Manufacturing Technologies, Springer2015, pp. 319-345.
[5] D.A. Rau, M. Forgiarini, C.B. Williams, Hybridizing Direct Ink Write and mask-projection Vat Photopolymerization to enable additive manufacturing of high viscosity photopolymer resins, Addit. Manuf. 42 (2021) 101996. https://doi.org/10.1016/j.addma.2021.101996.
[6] M. Ntagios, H. Nassar, R. Dahiya, Closed-Loop Direct Ink Extruder System with Multi-Part Materials Mixing, Addit. Manuf. (2023) 103437. https://doi.org/10.1016/j.addma.2023.103437.
[7] A. De Marzi, M. Vibrante, M. Bottin, G. Franchin, Development of robot assisted hybrid additive manufacturing technology for the freeform fabrication of lattice structures, Addit. Manuf. (2023) 103456. https://doi.org/10.1016/j.addma.2023.103456.
[8] Y. Chen, Y. Wang, Q. Yang, Y. Liao, B. Zhu, G. Zhao, R. Shen, X. Lu, S. Qu, A novel thixotropic magnesium phosphate-based bioink with excellent printability for application in 3D printing, J. Mater. Chem. B 6(27) (2018) 4502-4513. https://doi.org/10.1039/c8tb01196f.
[9] B. Nematollahi, M. Xia, J. Sanjayan, Current progress of 3D concrete printing technologies, ISARC. Proceedings of the international symposium on automation and robotics in construction, IAARC Publications, 2017.
[10] A. Zocca, G. Franchin, H. Elsayed, E. Gioffredi, E. Bernardo, P. Colombo, Direct ink writing of a preceramic polymer and fillers to produce hardystonite (Ca2ZnSi2O7) bioceramic scaffolds, J. Am. Ceram. Soc. 99(6) (2016) 1960-1967. https://doi.org/10.1111/jace.14213.
[11] H. Woods, A. Boddorff, E. Ewaldz, Z. Adams, M. Ketcham, D.J. Jang, E. Sinner, N. Thadhani, B. Brettmann, Rheological considerations for binder development in direct ink writing of energetic materials, Propellants Explos. Pyrotech. 45(1) (2020) 26-35. https://doi.org/10.1002/prep.201900159.
[12] O.S. Toker, S. Karasu, M.T. Yilmaz, S. Karaman, Three interval thixotropy test (3ITT) in food applications: A novel technique to determine structural regeneration of mayonnaise under different shear conditions, Food Res. Int. 70 (2015) 125-133. https://doi.org/10.1016/j.foodres.2015.02.002.
[13] H. Hong, H. Jiyong, K.-S. Moon, X. Yan, C.-p. Wong, Rheological properties and screen printability of UV curable conductive ink for flexible and washable E-textiles, J. Mater. Sci. Technol. 67 (2021) 145-155. https://doi.org/10.1016/j.jmst.2020.06.033.
[14] R. McKenzie, H. Koerner, Enabling direct writing of an epoxy resin with thermo-activated organic thixotropes, Addit. Manuf. 31 (2020) 100905. https://doi.org/10.1016/j.addma.2019.100905.
[15] F. Jiang, A. Wörz, M. Romeis, D. Drummer, Analysis of UV-Assisted direct ink writing rheological properties and curing degree, Polym. Test. 105 (2022) 107428. https://doi.org/10.1016/j.polymertesting.2021.107428.
[16] O. Rios, W. Carter, B. Post, P. Lloyd, D. Fenn, C. Kutchko, R. Rock, K. Olson, B. Compton, 3D printing via ambient reactive extrusion, Mater. Today Commun. 15 (2018) 333-336. https://doi.org/10.1016/j.mtcomm.2018.02.031.

[17] S. Li, Z. Lu, H. Zhang, Z. Ai, Y. Ran, Y. Li, X. Deng, D. Li, Rheological behavior of multi-sized SiC inks containing polyelectrolyte complexes specifically for direct ink writing, J. Eur. Ceram. Soc. (2022). https://doi.org/10.1016/j.jeurceramsoc.2022.04.048.
[18] A.M. Mostafa, A. Yahia, New approach to assess build-up of cement-based suspensions, Cem. Concr. Res. 85 (2016) 174-182. https://doi.org/10.1016/j.cemconres.2016.03.005.
[19] Q. Chen, T. Sukmanee, L. Rong, M. Yang, J. Ren, S. Ekgasit, R. Advincula, A dual approach in direct ink writing of thermally cured shape memory rubber toughened epoxy, Acs Applied Polymer Materials 2(12) (2020) 5492-5500. https://doi.org/10.1021/acsapm.0c00839.
[20] Y. Eom, F. Kim, S.E. Yang, J.S. Son, H.G. Chae, Rheological design of 3D printable all-inorganic inks using BiSbTe-based thermoelectric materials, J. Rheol. 63(2) (2019) 291-304. https://doi.org/10.1122/1.5058078.
[21] A. Corker, H.C.-H. Ng, R.J. Poole, E. García-Tuñón, 3D printing with 2D colloids: Designing rheology protocols to predict 'printability'of soft-materials, Soft Matter 15(6) (2019) 1444-1456. https://doi.org/10.1039/c8sm01936c.
[22] M.S. McClain, A. Afriat, B.J. Montano, J.F. Rhoads, I.E. Gunduz, S.F. Son, Dynamic combustion of functionally graded additively manufactured composite solid propellant, J. Propul. Power 37(5) (2021) 725-732. https://doi.org/10.2514/1.B38282.
[23] M.M. Rueda, M.-C. Auscher, R. Fulchiron, T. Perie, G. Martin, P. Sonntag, P. Cassagnau, Rheology and applications of highly filled polymers: A review of current understanding, Prog. Polym. Sci. 66 (2017) 22-53. https://doi.org/10.1016/j.progpolymsci.2016.12.007 0079-6700.
[24] L. del-Mazo-Barbara, M.-P. Ginebra, Rheological characterisation of ceramic inks for 3D direct ink writing: A review, J. Eur. Ceram. Soc. 41(16) (2021) 18-33. https://doi.org/10.1016/j.jeurceramsoc.2021.08.031.

Chapter 2

Literature Review

2. Literature Review

2.1 Motivation for Direct Ink Write Additive Manufacturing

Using the concepts of thermoplasticity, fused filament fabrication (FFF) has become the most popular method for rapidly prototyping potential engineering designs. Given the affordability, weight-efficiency, and availability of FFF printers, this technique makes up nearly 70% of the additive manufacturing (AM) market [1]. While the nozzle-based design allows for accurate start-stop deposition, a consistent drawback of this fabrication method is the difficulty in optimizing interlayer adhesion and porosity during the re-solidification process [2]. As such, mechanical properties of parts printed via FFF are often limited by sufficient diffusion of polymer chains between successive layers [3]. Materials for FFF must also be thermoplastic, which restricts material selection heavily while imposing limitations on the temperature-use range of the final product.

An alternative to this printing method is stereolithography (SLA). As one of the oldest forms of additive manufacturing, SLA uses exothermic reactions initiated by ultraviolet (UV) light to selectively cure a photoresin [4]. The UV light cleaves photoinitiators, thus forming free radicals, which polymerize low molecular weight monomers causing solidification [5]. One form of SLA – projection SLA – requires a vat of low-viscosity photoresin, whereby thin layers are cured by projecting a two-dimensional "mask" of the desired image onto a build platform before lowering the platform to introduce the next layer of photoresin [5]. Conversely, laser scanning SLA utilizes a single laser to selectively cure a UV-reactive material using galvanometric mirrors [4]. While these materials can be high strength and resolute at the micron- or nano-scale, overcuring is a prevalent issue that results in warping and inaccurate part dimensions without proper exposure studies [6].

In an effort to combine the nozzle-based design of FFF with the reactive nature of SLA, direct ink write (DIW) AM has emerged as a popular 3D printing technique for reactive, highly viscous and/or colloidal systems. These "inks" are extruded using pressure-driven designs, which enables dispensing of high viscosity photoresins, thermosetting materials, and composites [7]. DIW inks are extruded layer-by-layer similar to FFF, and as long as they possess sufficiently high dynamic stresses (resulting from strong interparticle networks), the internal structure of the extrudate will maintain the shape of the printed bead post-deposition [7]. As stated, the resin itself can also be reactive, which enables *in-situ* and/or post-curing mechanisms to take place (e.g. thermal crosslinking or photopolymerization) [8]. This form of additive manufacturing facilitates vast material selection including fiber reinforced composites [9], foodstuffs [10], energetic materials [11], clays/ceramics [12], cellulose [13], and concrete [14]. To this extent, materials whose rheological, mechanical, and printing properties are governed by the aforementioned interparticle network are termed "highly filled" or "high solids content" systems [15].

The purpose of this review is to outline the fundamentals and state-of-the-art advancements in high solids content rheology. The major focus of this research is interparticle network disruption during direct ink write additive manufacturing, and methods to mitigate this phenomenon using reactive systems. Four distinct sections are included to develop a holistic view of highly filled systems for DIW. Section 2.2 covers fundamentals of polyurethane synthesis/processing, as well as the differentiation between crosslinked and thermoplastic polyurethanes. Section 2.3 discusses the definition, basic rheology, and time-dependent structural recovery (thixotropy) of highly filled composites. The challenges of rheological testing and printing highly filled materials are also considered here. Section 2.4 contains the specific rheological protocols available for probing structural recovery of high solids content inks after experiencing periods of high stress or strain.

An introduction to methods for improving recoverability via chemical reactions is also covered, with a distinct focus on the rheology of these processes – known as "chemorheology." A discussion of rheology as a tool for predicting/assessing printability is used to conclude this section. Finally, section 2.5 provides an extensive account of the most recent advances in preventing structural breakdown during DIW 3D printing of reactive systems. The scope of publishings detailed in this section encompasses reactive, highly filled polymers for DIW AM which experience thixotropy. Using rheological/viscoelastic arguments, this section identifies the five most common methods to improve recovery via resin reactivity. Approaches such as these enable significant reductions in cost and experimentation times since rheological tests often only require a gram of material or less. Hence, this review signifies the importance of rheology for highly filled, reactive systems in the emerging field of direct ink write additive manufacturing.

2.2 Polyurethanes

The versatility of polyurethanes has enabled them to be processed into a variety of products including coatings, adhesives, insulators, and fibers for flexible textiles [16-18]. The reason for this vast set of applications is the multitude of synthetic pathways available for polymerization. Most often, polymerization involves the combination of a polyol and a diisocyanate, although it is also possible to form polyurethanes through free radical polymerization of UV-curable urethane diacrylates [19, 20]. In fact, some studies have eliminated the need for isocyanates altogether by incorporating thiols into the binder (i.e. "click" chemistry) [21].

2.2.1 Crosslinked Polyurethanes

The functionality of the polyol specifically contributes to crosslinking during step growth polymerization, the result of which is a thermosetting polyurethane [22]. This is in part because of vinyl groups which form non-linear urethane linkages [22]. Kinetically, however, the reactivity

and cure progress of polyurethane formation is almost exclusively driven by the choice of diisocyanate due to the relatively high molecular weight of the polyol [23].

In regard to diisocyanate reactivity, the two factors most influential towards cure progression are the electron withdrawing capabilities of the diisocyanate, and the symmetry of isocyanate groups. For example, toluene diisocyanate (TDI) contains aromatic rings which lower the energetic barrier for reactions during the transition state, and also contains asymmetric isocyanate groups which cause a distinct two-stage buildup of molecular weight growth [19]. By contrast, hexamethylene diisocyanate (HMDI) contains cyclohexane rings which slow the cure progression, and the isocyanate groups are axisymmetric, causing single-stage molecular weight growth [19]. By the same token, it is also possible to have fast, single-stage reactions (e.g. methylene diphenyl diisocyanate, MDI) or slow, two-stage reactions (isophorone diisocyanate, IPDI) [19].

Based on the choice of diisocyanate and the ratio of hydroxyl (OH) to isocyanate (NCO) groups, final products will elicit a range of mechanical properties due to variations in the number of hard and soft segments [24]. The hard segments (short-chain diols and chain extenders) are responsible for overall strength and development of mechanical properties, whereas soft segments (typically polyethers and polyesters) provide flexibility and chain mobility; resultingly, polyurethanes are classified as randomly coupled multiblock copolymers [24-26]. Since moderately elevated temperatures (<100 °C) are frequently used for these reactions, the timescale for full conversion can span multiple days; therefore, catalysts or functionalized polybutadienes are often necessary for non-isothermal kinetic studies [27-33].

2.2.2 Thermoplastic Polyurethanes

For linear polyurethanes (i.e. a functionality of 2), attaining a critical temperature threshold permits melt flow deposition [26]. From a molecular standpoint, this phenomenon – termed "thermoplasticity" – is enabled because of the thermally labile, weak intermolecular forces between polymer chains which are disrupted at elevated temperatures [34]. Thermoplastic behavior can be exploited for a variety of processing techniques including fused filament fabrication, selective laser sintering, injection molding, and single/twin-screw extrusion [35-37]. Although thermoplastic polyurethane (TPU) has the advantage of utilizing these manufacturing methods, a persistent issue is mechanical failure due to microphase separation between the thermodynamically incompatible hard and soft segments [38]. This problem has prompted an entire field of research dedicated improving mechanical properties via TPU blends [38].

While chain incompatibility presents one side of processing concerns for TPU, another pervasive challenge is side reactions. Covalently crosslinked polyurethanes in section 2.2.1 are typically synthesized and processed at temperature less than 100 °C; however, thermoplastic polyurethanes are consistently processed at temperatures ranging from 190-220 °C [39]. This is particularly problematic since degradation of the urethane linkage occurs at temperatures as low as 200°C [40]. Resultingly, undesirable side reactions are prominent at elevated temperatures in the presence of air and moisture [40].

A common example of these side reactions is formation of an allophanate branch at temperatures in excess of 150 °C. Especially with excess diisocyanates, the nucleophilic nitrogen in the polyurethane backbone is able to further react with an isocyanate group, thus forming a branch [41]. Similarly, without proper expulsion of air and water using a vacuum oven, moisture can form amine groups via isocyanate decarboxylation, which creates a urea when exposed to carbon dioxide; further reaction with an isocyanate will cause biuret branching [42, 43]. In other

cases, the environment itself is not responsible for side reactions, but rather the reactions naturally occur without proper control via catalysis. A frequent example of this uncontrolled reactivity is dimerization and trimerization of the diisocyanate, which subsequently forms either a uretdione or isocyanurate, respectively [44]. Thus, control of operating conditions during melt flow deposition of TPU has become one of the major challenges faced by polymer scientists and engineers at all stages of production, including synthesis, processing, and end-use.

2.3 Highly Filled Systems

2.3.1 Basics of Rheology

Rheology is a branch of physics covering the deformation and flow of matter [45]. The materials range from simple Newtonian fluids and stiff solids to complex polymers which exhibit both elastic and viscous behavior – termed "viscoelastic" materials. When sheared at a given rate using devices such as viscometers, the ratio of the shear stress to the shear rate defines the viscosity shown in Equation (2.1).

$$\eta = \frac{\sigma}{\dot{\gamma}} \tag{2.1}$$

Where η is the shear viscosity, $\dot{\gamma}$ is the shear rate in s^{-1}, and σ is the imposed shear stress [46]. For solid-like materials, the rigidity modulus *G* (during shear deformation) or elastic modulus E (during tensile deformation) are defined by the ratio of stress "σ" to strain "γ" in Equation (2.2) [46].

$$G \text{ or } E = \frac{\sigma}{\gamma} \tag{2.2}$$

In a laboratory setting, devices such as viscometers can reveal the viscous properties of fluidic substances, while tensile testing devices can unveil the solid-like behavior of elastic

materials. However, when a material (e.g. polyurethane) exhibits both viscous and elastic properties, rheometers are necessary to probe these viscoelastic effects. The most common device – a torsional rheometer – has a top and bottom geometry, one of which freely rotates on a spindle using a nearly frictionless bearing. This spindle is attached to a motor (and often a force transducer) which allows for precise movements of the geometry. A raw force is placed on the spindle, allowing it to oscillate, which is translated into a geometry-dependent torque. This torque elicits strain on the sample, which is transformed into a storage and loss modulus illustrated in Equations (2.3) and (2.4) [47].

$$G' = \frac{\tau_0}{\gamma_0}\cos(\delta) \tag{2.3}$$

$$G'' = \frac{\tau_0}{\gamma_0}\sin(\delta) \tag{2.4}$$

Here, *G'* is the storage modulus, *G''* is the loss modulus, τ_0 and γ_0 are the applied stress and strain, and δ is the phase angle. When the stress is directly proportional to strain, δ is 0°, suggesting the material has an entirely elastic response to stress; for purely viscous materials, the phase angle is completely out of phase at 90° [47]. Any angle in-between implies that the material is "complex" and experiences viscoelasticity. The advantage of oscillating a material instead of steadily shearing it is that modulus data can be used to define the relative solidity/fluidity of sample. Representative viscoelastic properties gained from oscillation experiments are illustrated in Equations (2.5)-(2.8) [47].

$$\tan(\delta) = \frac{G''}{G'} \tag{2.5}$$

$$\eta' = \frac{G''}{\omega} \tag{2.6}$$

$$\eta'' = \frac{G'}{\omega} \tag{2.7}$$

$$|\eta^*| = \sqrt{\eta'^2 + \eta''^2} \tag{2.8}$$

Where tan(δ) is the loss tangent, ω is the oscillation frequency is rad s^{-1}, η' is the dynamic viscosity, η'' is the out-of-phase component of complex viscosity, and η^* is the complex viscosity in Pa-s. In this respect, materials which are fluidic experience loss tangents > 1, and solid-like materials possess loss tangents less than unity.

2.3.2 Definition of Highly Filled

The degree to which polymers can be strained before experiencing potentially irreversible deformation is limited by the linear viscoelastic region (LVR) of the material. For unfilled polymers, this limit is defined by entanglement of polymer chains; as molecular weight increases, polymer chains become longer, creating more intermolecular interactions, thus permanently deforming the system and exiting the region of linearity when excessive strains are introduced [46, 48]. Elevated shear rates can also cause chain alignment, effectively decreasing the viscosity of the polymer while shortening the length of the LVR [46].

Similar to entanglement of polymer chains, another way to produce an internal structure is by introducing solid fillers to a polymer resin. In this respect, fillers create interparticle interactions via Van der Waals forces which form interparticle networks, thus limiting the range of motion a sample can experience before exiting the region of linearity [49]. Though the definition varies widely, a system is considered "highly filled" when interparticle interactions define the rheological properties of a system, such that they outweigh the viscoelastic behavior of the resin in which they are loaded [15, 49-51]. Further, interparticle networks/interactions should drive de-

agglomeration/recovery processes such that time-dependent recovery is driven by network re-agglomeration as opposed to chain re-entanglement [52].

These systems are unique in that they do not follow linear concentration-viscosity relationships, such as Einstein's equation in Equation (2.9) where η_r is the relative viscosity, and Φ is the volume fraction of solids [15].

$$\eta_r = 1 + 2.5\Phi \tag{2.9}$$

Increasing the concentration of solid fillers will indeed decrease the length of the linear viscoelastic region and increase the viscosity of the system, although this often occurs non-linearly [15, 53]. Decreasing the size of the particles at a given concentration will also shorten the LVR and increase the viscosity dramatically due to an increased presence of electrostatic forces [15]. The degree of shear thinning (i.e. the slope of viscosity as a function of shear rate) also increases with concentration, although the effect of particle size on shear thinning is often ambiguous. Some fillers display size-dependent effects on the degree of shear thinning, although this appears material-dependent, and shear thinning capabilities may not always be affected by particle diameter [54-56].

Due to the electrostatic forces of interparticle networks, flocculation and/or aggregation can also result [49]. While often used interchangeably, these terms are complete opposites; flocculates (also called agglomerates) are clusters of particles which can be destroyed and reformed after periods of stress, whereas aggregates are clusters of particles which *cannot* be destroyed during rheological testing [57]. Agglomerates and aggregates alike trap the surrounding resin between clusters of solid fillers, effectively increasing the viscosity beyond what would be predicted using models for dilute suspensions [49]. The presence of these clusters, and the shear-

induced drops in viscosity associated with them, provides an opportunity to discuss thixotropy – a key feature of highly filled systems.

2.3.3 Thixotropy

The International Union of Pure and Applied Chemistry defines thixotropy as “the continuous decrease of viscosity with time when flow is applied to a sample that has been previously at rest, and the subsequent recovery of viscosity when flow is discontinued" [58]. Stress relaxation of thixotropic materials is instantaneous; this is in contrast to viscoelastic aging, which involves elastic, time-dependent stress relaxation after cessation of flow [58]. Especially after flowing through the high shear region of a nozzle during DIW, highly filled composites are some of the most prominent materials to experience a thixotropic response to stress [15].

Both colloidal and non-colloidal systems can experience thixotropy [59]. Unfilled systems, multi-component polymeric liquids, solutions, and blends may exhibit thixotropic effects through chain disentanglement/re-entanglement [59]. Conversely, when a dispersed phase (solid fillers) is present within a continuous phase (the polymeric medium), interparticle interactions form microstructures in the form of an interparticle network [60]. Once composites are sheared, they transition from one microstructure to another as a result of structural breakdown, structural buildup, Brownian motion, or particle collision [61]. In the case of highly filled composites, shear thinning and breakdown of flocs play a large role in microstructural rearrangement. So long as the time scale available for structural recovery exceeds the timescale for data collection, structural breakdown and subsequent recovery (i.e. thixotropy) can be analyzed [61].

To avoid confusion, the terms “shear thinning/shear thickening” and “thixotropy/anti-thixotropy” are defined explicitly here. When a material achieves a lower viscosity as a result of

increased shear rates, strains, or stresses, it is referred to as a "shear thinning material." If the viscosity instead reaches a higher equilibrium value, the material is "shear thickening." Thus, these terms refer to new *equilibrium points* at a given rate. However, as the material is being sheared, the viscosity might asymptotically lower to a new equilibrium point. Whether this equilibrium is lower or higher than the baseline does not matter; if the path to get there lowers the viscosity over time once shear rates/frequencies are increased, the material is thixotropic. Similarly, if the path to reach a new equilibrium results in the viscosity increasing over time (even if the new equilibrium is lower than the baseline), the material is anti-thixotropic. Thus, these terms refer to the *dynamics* as a material approaches a new equilibrium, as illustrated in Figure 2.1 [62].

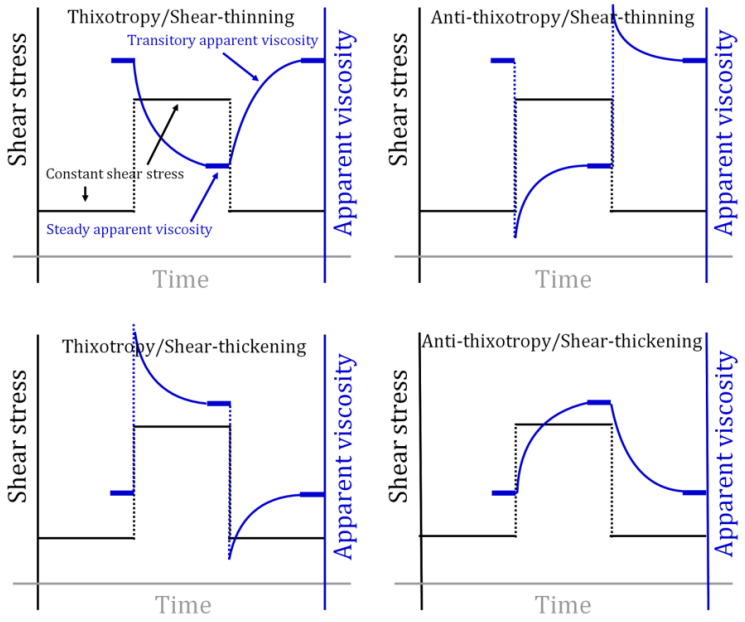

Figure 2.1: Differences between shear thinning/thickening and thixotropy/anti-thixotropy during step-wise increases in shear stress, reprinted with permission from Rubio-Hernández et al. [62].

Empirical equations make up a large portion of literature regarding thixotropic modeling. De Souza Mendes et al. (2012) calculated the change in microstructural organization of a material

λ with respect to shear rate $\dot{\gamma}$ by modeling it as a function of the rate of structural equilibrium T_0, shearing properties α, and shear rate – shown in Equation (2.10) [63].

$$\frac{d\lambda}{d\dot{\gamma}} = \frac{1}{T_0} - \alpha\lambda\dot{\gamma} \tag{2.10}$$

A more generic model of microstructural breakdown/buildup was proposed by Mujumdar et al. (2002). Following a kinetics-based approach of microstructural deformation/reformation, the "rate constants" k_1 and k_2 and "reaction orders" a and b, illustrated in Equation (2.11), were used to balance the effects of shear-induced de-agglomeration against time-dependent viscosity buildup [64].

$$\frac{d\lambda}{dt} = -k_1\lambda\dot{\gamma}^{\alpha} + K_2\lambda\dot{\gamma}^{b} \tag{2.11}$$

As is popular for reaction modeling, second order structural recovery models have also been utilized by Toker et. Al (2015) to elucidate time/rate dependent recovery of emulsions, presented in Equation (2.12) [65]. Here, G_e is the equilibrium storage modulus at long times, G_0 is the initial storage modulus, k is the recovery constant of a sample, t is time, and n is a structural kinetic parameter assumed to be 2.

$$\left(\frac{G' - G_e}{G_0 - G_e}\right)^{1-n} = (n-1)kt + 1 \tag{2.12}$$

The individual thixotropic and phase volume contributions towards viscosity were extensively studied and modeled by Cipriani et al. (2022) [66]. Expectedly, the magnitude of viscosity increase correlated highly with the loading level of filler, which was caused by flocculate formation. Using a variation of the three interval thixotropy (to be discussed in section 2.4.2), this research utilized stepwise changes in shear rate to elucidate the parameters illustrated in equations (2.13)-(2.15).

$$\eta_s(t,\Phi) = f(t)g(\Phi) \tag{2.13}$$

$$f(t) = \frac{\eta_0\eta_\infty}{\eta_\infty + (\eta_0 - \eta_\infty)\exp\left[-\frac{t}{\lambda}\right]} \tag{2.14}$$

$$g(\Phi) = 1 + \alpha_1\Phi + \alpha_2\Phi^2 \tag{2.15}$$

f(t) describes the time-dependent thixotropic contribution to viscosity, while *g(Φ)* represents the contribution of solid fillers. η_0 is the zero-shear viscosity, η_∞ is the infinite shear viscosity, η_s is the total viscosity, t is time, Φ is the volume fraction of solids, α is a constant, and λ is the structural buildup time determined by curve fitting.

For filled, reactive resins, the effects of structural change during thixotropic processes becomes more complicated since physical aging must be balanced against time-dependent chemical reactivity. An example of this is illustrated in Equation (2.16) – where the first half of the equation represents physical aging, and the second half contains chemical aging during precipitation of hydrates [67].

$$\eta(t) = \eta_0\left(1 - e^{\left(-\frac{t}{\tau_1}\right)^\beta}\right)\left(1 + \left(\frac{t}{\tau_2}\right)^\alpha\right) \tag{2.16}$$

Equation (2.16) utilizes the Levenberg-Marquardt adjustment algorithm to model viscosity as an exponential physical aging process and a linear chemical aging process. This process takes part in three stages: the first is governed by physical aging, the second acts as an intermediate transition region, and the third is driven by chemical aging. Here, $\eta(t)$ is the viscosity as a function of time, η_0 is plateaued viscosity during an intermediate regime, τ_1 is an exponential time constant, β is a constant related to the broadness of τ_1, τ_2 is a time constant representing the beginning of the third stage, and α is a power law exponent relating time and viscosity [67].

Thixotropic modeling has been extensively researched for a vast array of materials, and countless empirical equations likely exist in literature [15, 58, 59, 61, 68]. The equations discussed in this review simply represent a set of generalizable equations that can be altered depending on the application of concern and the type of experiment performed. Ideally, microstructural changes of highly filled systems would be visualized using a combination of spectroscopic and light scattering techniques before, during, and after periods of high shear. Unfortunately, as elucidated by Wyss et al., "the refractive index difference between the solid and the liquid phases is usually too high to enable measurement of their microstructure using standard light scattering techniques" [54]. Hence, flow field measurements (rheology) and advanced simulation are essential when capturing the microstructural rearrangement of highly filled composites during macroscale deformation processes (e.g. 3D printing) [58].

2.3.4 Current Rheological Challenges in Direct Ink Write Additive Manufacturing

The rheology of highly filled systems is challenging from a repeatability standpoint, and is prone to several artifacts of experimental error [69]. For moderately concentrated suspensions in low viscosity matrices, wall slip is among the most common artifacts of error [70]. High shear regions of the wall during capillary flow (e.g. capillary rheology or direct ink write extrusion) cause migration of solid fillers to the center of the nozzle, resulting in a "low-viscosity resin-rich" region near the wall [56]. This "slip velocity" increases with larger particles since the fillers cannot get as close to the wall, resulting in larger slip layers [56]. These effects also occur in parallel plate rheology, illustrated in Figure 2.2.

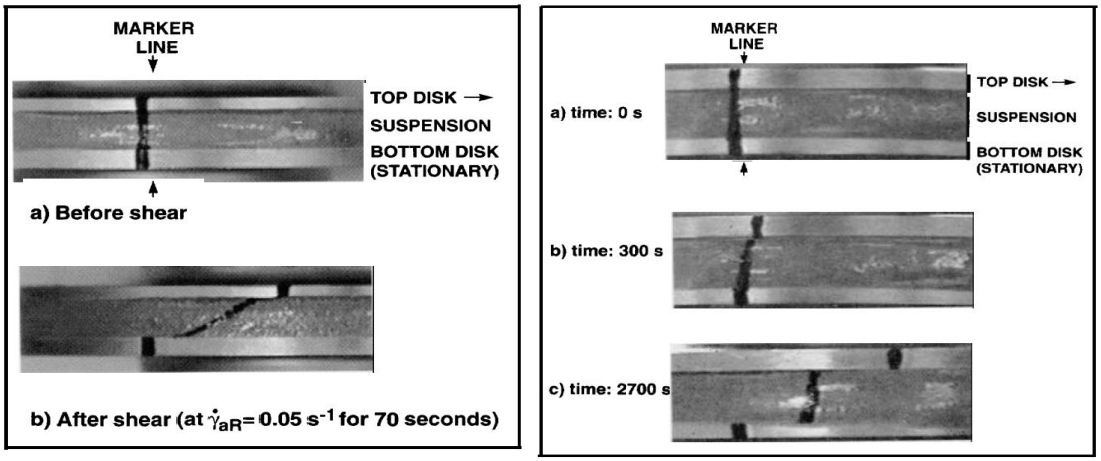

Figure 2.2: (Left) Development of a proper flow field and (Right) evidence of wall slip during steady shear rheology using parallel plates, reprinted with permission from Kalyon et al. [71].

The slip velocity during parallel plate shear flow can be calculated by adding a slip velocity term to the Weissenberg-Rabinowitsch correction, shown in Equation (2.17) [71].

$$\dot{\gamma}_{aR} = \dot{\gamma}_R(\tau_R) + \frac{2U_s(\tau_R)}{H} \tag{2.17}$$

Where $\dot{\gamma}_{aR}$ is the apparent shear rate at the edge of the plate, $\dot{\gamma}_R$ is the true shear rate, τ_R is the true shear stress, U_s is the slip velocity, and H is the gap height. Similar works have been published which effectively create a Weissenberg-Rabinowitsch correction for oscillatory experiments using frequency sweeps at various gap heights [56]. Thus, although an undesirable property during rheological testing, it is possible to understand the contribution of slip towards flow velocity, especially in the DIW setting.

As a highly filled composite continues to flow (i.e. at the high shear regions at the edge during parallel plate rheology or at the wall during capillary flow), an uneven pressure distribution causes regions of solid-like buildup to occur [72]. This effect – denoted as "liquid phase migration" – is illustrated in Figure 2.3.

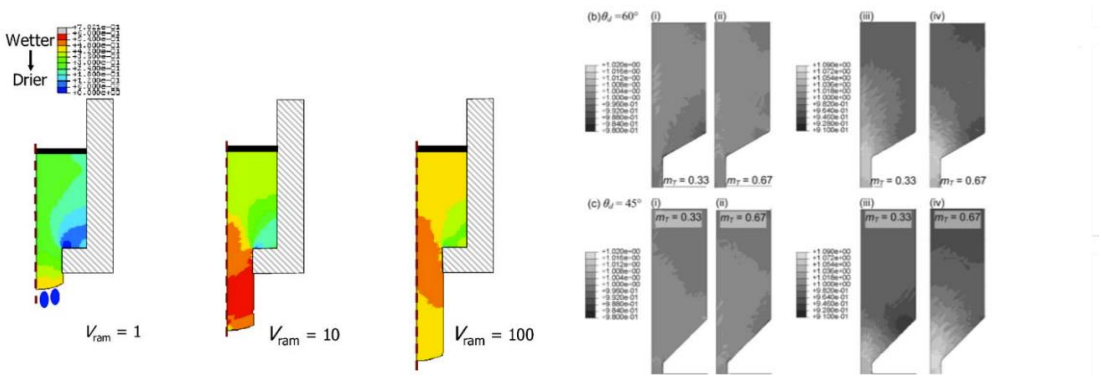

Figure 2.3: Finite element simulation of liquid phase migration during ram extrusion, reprinted with permission from Patel and Wilson [72, 73].

Liquid phase migration is an especially undesirable trait during extrusion since it results in an inhomogeneous extrudate [74]. As the solid filler collects in static regions of the die landing, liquid resin seeps out through the nozzle, although this effect can be mitigated with larger extrusion speeds, steeper die landings, and nozzles with less friction – especially if conical entries are used [72, 74, 75].

In contrast to the occurrence of liquid phase migration during DIW, materials may lack any extrusion capabilities whatsoever due to complete nozzle clogging. As discussed in section 2.3.2, an increase in solids loading reduces the average interparticle distance, effectively increasing the number of closest neighboring particles, thus driving increases in elasticity [12]. As a result, extrusion capabilities diminish without sufficiently large backpressures. Particles have the ability to form bridges across the nozzle via "arching," which can prevent extrusion entirely [76]. Under the assumption of Hagen-Poiseuille flow, particles in the center have increased drag forces compared to those at the wall; this uneven distribution of forces causes agglomeration due to particle-particle interactions. These frictional effects lead to either intermittent or complete cessation of flow during deposition, illustrated in Figure 2.4 [76].

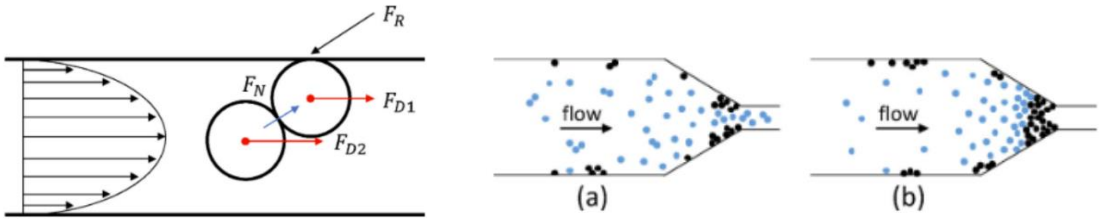

Figure 2.4: Illustration of interparticle interactions causing partial reduction (a) and complete cessation (b) of flow, reprinted with permission from Beran et al. [76].

This finding is troublesome, since most inks require a large resting LVR modulus at or above 2-10 kPa – which can result in clogging due to jamming and excessive extrusion pressure requirements [77-79]. Gunduz et al. (2018) revealed a solution to this problem by using an ultrasonic actuator attached to the nozzle of a DIW printhead [80]. This method, shown in Figure 2.5, successfully deposited 62 vol% polymer clay, natural clay, and aluminum-polymer composites as well as fondant. Since a mechanical force breaks apart the jammed material, it eliminates the potential accumulation of backpressures which often ineffectively break apart jammed material within the nozzle [76].

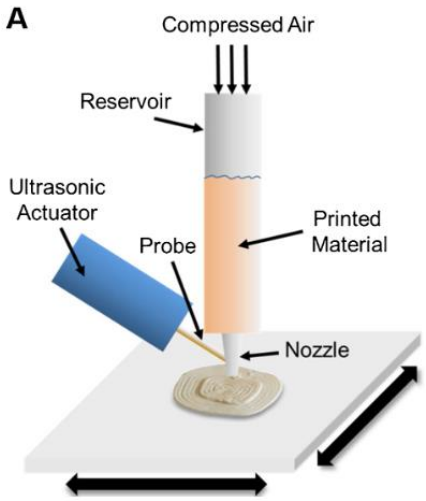

Figure 2.5: Schematic of an ultrasonic actuator-assisted DIW setup, reprinted with permission from Gunduz et al. [80].

To this end, a detailed description of a highly filled ink's microstructure – and how it relates to macroscopic concepts of thixotropy – is heavily desired for DIW extrusion. While crystallographic, neutron scattering, and X-ray scattering techniques may capture the microstructural properties of particulate-filled systems, the link between these findings and their macroscopic counterparts (e.g. rheology and printability) is elusive [54]. As a result, most tests for printability still "rely on visual inspection or image analysis" [81]. This shortcoming provides an opportunity to utilize rheology as a method to predict printability and assess the overall thixotropy of a system. Further, rheology can be used as a tool for tracking the cure progress of chemical reactions in filled and unfilled systems, as outlined in section 2.4.3 [29, 30, 82].

2.4 Quantifying Thixotropy and Reaction Progress

2.4.1 Hysteresis Loop

The "hysteresis loop" or "thixotropic loop" is a widely used rheological technique which raises the shear rate of a rheometer or viscometer in a ramping fashion, measuring the shear stress

at each rate [83]. The shear rate reaches a maximum, and then decreases to the original low rate. The idea of this test is that a material will experience structural deformation at high rates, which takes time to recover, and be reflected as a decrease in viscoelastic properties during the descending rate regime. An example of this method is illustrated in Figure 2.6.

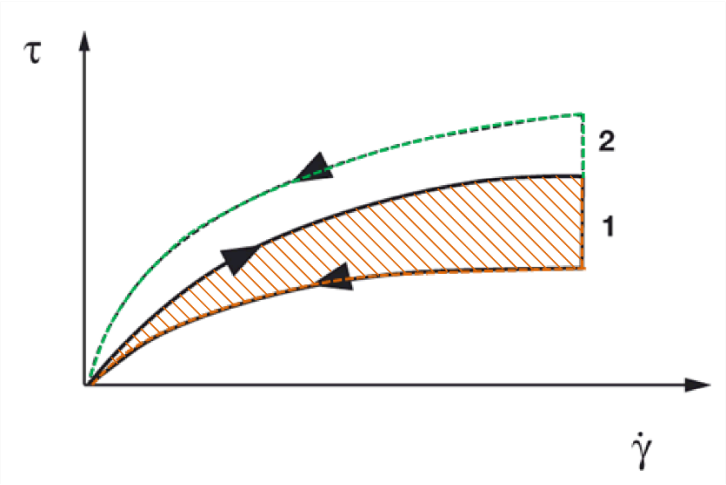

Figure 2.6: Example of a hysteresis loop for (1) structural breakdown and (2) structural buildup, reprinted with permission from Anton Paar [83].

The area between the "up" and "down" curves is used as a quantitative measure of thixotropy, denoted as the "thixotropic index" which enables comparison of like-materials at different testing conditions [84]. The crosshatched area "1" in Figure 2.6 displays characteristic thixotropic behavior, whereas the non-crosshatched area "2" represents an anti-thixotropic material which experiences shear-induced structural buildup. Oftentimes, the thixotropic loop is used to induce dispersive mixing which breaks up agglomerates in thixotropic, yield stress fluids [85].

While hysteresis loops are easy to perform and analyze, the methodology is considered outdated and non-representative for most applications. The progressive ramping of shear rate

means that the process is “non-equilibrium,” suggesting that results heavily depend on the minimum and maximum shear imposed [84]. The shear history of the sample during preparation/loading, in addition to the sampling time, can also influence results [68]. The equipment itself is also subject to rotor inertia, causing noise during stress readings [61]. In regard to DIW, the slow-ramping nature of a hysteresis loop is not representative of the start-stop deposition process. Instead, equilibrium-based stepwise increases in shear stress/strain – known as three interval thixotropy testing (3ITT) – have become a rheological standard for determining the structural breakdown/recovery process of thixotropic materials [57].

2.4.2 Three Interval Thixotropy Testing

Three interval thixotropy tests have quickly become the standard for determining structural breakdown/recovery of highly filled materials, particularly because they are more representative of the application at hand [83]. The test is performed in three successive steps. First, low strain, small amplitude oscillatory shear (SAOS) data within the LVR is gathered for a given time, which represents the material as it rests (e.g. paint sitting on a paint brush or ink sitting in the barrel of a 3D printer). Next, large amplitude oscillatory shear (LAOS) measurements outside of the LVR are used to represent the large stresses experienced during application. This could be representative of paint being spread on a wall, or inks being extruded through a small nozzle. During this regime, structural breakdown of the interparticle network occurs, which leads to a rapid decrease in viscoelastic properties. Finally, SAOS data is collected again, and viscoelastic parameters recover (sometimes incompletely) to their original values – representative of the material as it rests post-stress [86, 87].

There are numerous ways to perform these experiments, and they are not limited to low-high-low steps in strain. For example, it is possible to increase both the shear strain *and* the

frequency to represent the high stresses and shear rates experienced during extrusion [88]. The second step may also be performed under steady shear rotation to allow for more significant network destruction via an "oscillation-rotation-oscillation" protocol [78]. It is worth noting that 3ITT can be performed entirely using steady shear rotation by performing step changes in rotational velocity, although this method does not provide modulus data and will suffer from edge fracture even at small shear rates [89]. An example of 3ITT is illustrated in Figure 2.7.

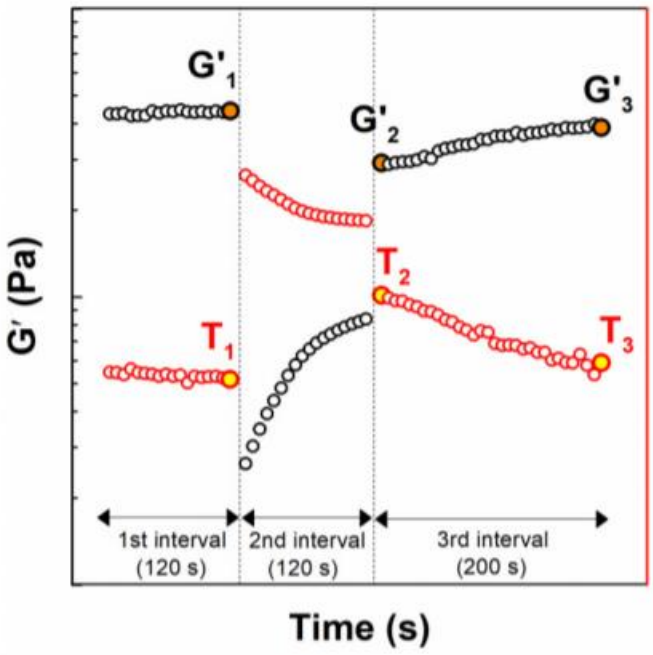

Figure 2.7: Example of three interval thixotropy testing, reprinted with permission from Eom et al. [90].

Here, G_1' is the modulus at the end of the first interval, G_2' is the modulus at the beginning of the third interval (immediately after network destruction due to LAOS occurs), and G_3' is the modulus at the end of the third interval (once the recovery period ends). T_1, T_2, and T_3 are the loss tangents at each of these respective time points [90].

While section 2.4.4 will outline the specific use of rheology as a tool for assessing/predicting printability, it is worth noting here several parameters that the three interval thixotropy test provides in regard to DIW. The most common parameters gathered from 3ITT are illustrated in Equations (2.18)-(2.21) [90].

$$De = \frac{G_1' - G_2'}{G_1'} \tag{2.18}$$

$$Rec = \frac{G_3'}{G_1'} \tag{2.19}$$

$$Rs = \frac{T_1 - T_2}{T_1} \tag{2.20}$$

$$Recs = \frac{T_1}{T_3} \tag{2.21}$$

Here, *De* is the degree of structural deformation, *Rec* is the degree of structural recovery, *Rs* is the relative solidity, and *Recs* is the degree of recovery for structural solidity. These parameters act as normalizers for determining how much a viscoelastic property changes after subjection to large amounts of stress or strain. Similarly, the mutation number in Equation (2.22) can be used to quantify the contribution of recovered modulus or modulus recovery rate towards overall recovery capabilities [79].

$$\lambda_{mut} = \left(\frac{1}{G_{end}'} \left(\frac{dG'(t)}{dt} \right)_{rebuilt} \right)^{-1} \tag{2.22}$$

In Equation (2.22), G_{end}' is the storage modulus at the end of the third interval, and $\left(\frac{dG'(t)}{dt}\right)_{rebuilt}$ is the rate of modulus recovery during a non-specific timeframe in the third interval – though it is often within first several seconds of recovery. Parameters such as the mutation number aid discussions of whether the final modulus or modulus recovery rate contribute more to

printability in the DIW setting. Oftentimes, these viscoelastic properties can be improved through reactivity of the resin material, which improves printability [91] This discussion provides an opportunity to differentiate the structural effects of thixotropy from chemically-induced reformation, and introduce the concept of chemorheology.

2.4.3 Chemorheology

Because printed materials can sag excessively post-deposition, a method to track short- and long-term cure progress of filled and unfilled systems under a variety of curing conditions is essential when screening for potential DIW inks [88, 92]. In contrast to 3ITT – which acts as a rheological method to model interparticle network recovery – chemorheology uses the capabilities of a torsional rheometer to track the cure progress of a reactive resin via increases in viscoelastic properties over time [93].

For thermally curing systems, increases in viscosity can be modeled using an Arrhenius-style equation which accounts for the time-temperature dependence of thermosetting materials, as illustrated in Equations (2.23)-(2.25) [93].

$$\ln \eta(t) = \ln \eta_r + kt \tag{2.23}$$

$$\eta_r = \eta_\infty e^{\frac{\Delta E_\eta}{RT}} \tag{2.24}$$

$$k = k_\infty e^{\frac{\Delta E_k}{RT}} \tag{2.25}$$

Here, η_r and k are temperature-dependent viscosity and rate constants, η_∞ and k_∞ are the infinite temperature viscosity and rate constants, ΔE_η and ΔE_k are the activation energies associated with the viscosity and reaction rate, R is the universal gas constant, and T is the absolute temperature. For materials which experience molecular weight growth in multiple stages (e.g. diisocyanates with asymmetrically reactive functional groups), this type of equation can be used

to describe each step independently [30, 33, 94]. The rate of conversion can also described using autocatalytic models such as the Kamal-Sourour equation, shown in Equation (2.26) [29, 30].

$$\frac{d\alpha}{dt} = (k_1 + k_2\alpha^a)(1-\alpha)^b \tag{2.26}$$

The Kamal-Sourour model uses k_1 and k_2 as reaction rate constants, in addition to a and b as reaction order constants. Conversion is denoted as α, which can be difficult to measure without methods such as *in-situ* curing during Fourier transform infrared spectroscopy (FTIR); however, previous authors have estimated conversion using storage modulus during multi-day chemorheological experiments, as illustrated in Equation (2.27) [95].

$$\alpha = \frac{G'(t) - G'(0)}{G'(\infty) - G'(0)} \tag{2.27}$$

Equation (2.27) estimates conversion by comparing the storage at any given time $G'(t)$ to the final storage modulus $G'(\infty)$ and normalizing it by the initial storage modulus $G'(0)$. This method enables purely rheological methods to track cure progress while relaxing assumptions of linearity (i.e. Arrhenius-style equations) in favor of power law relationships (i.e. the Kamal-Sourour model) [29, 30].

For more complex autocatalytic reactions, the Prout-Tompkins equation described in Equation (2.28) combines the Arrhenius-style temperature dependence of curing reactions with power-law approaches present within the Kamal-Sourour model [96].

$$\frac{d\alpha}{dt} = Ae^{\left(\frac{-E_a}{RT}\right)}\alpha^m(1-\alpha)^n(-\log(1-\alpha)^p) \tag{2.28}$$

The activation energy E_a can be obtained using an Arrhenius analysis at several different temperatures, and there are also three reaction orders m, n, and p. By neglecting the log term on a "system-dependent basis," the Prout-Tompkins equation can be simplified to the Sestak-Berggren

model in Equation (2.29). This form is commonly used for crosslinking reactions, and simplifies interpretation of parameters when performing non-linear curve fitting [96].

$$\frac{d\alpha}{dt} = Ae^{\left(\frac{-E_a}{RT}\right)}\alpha^m(1-\alpha)^n \tag{2.29}$$

In addition to the common thermosetting reactions during DIW, *in-situ* and *ex-situ* UV light can be used to solidify inks on the build bed [91]. The cure depth of these materials is impacted by several factors. For example, different photopolymers/photoinitiators will activate at different wavelengths – although this does not always affect cure depth meaningfully [97]. High amounts of opaque filler will also block or absorb UV light, causing a reduction in cure depth; reductions in cure depth due to fillers can often be combatted by increasing the intensity of UV light [97, 98]. Jacob's working curve, in Equation (2.30), is useful for equating the cure depth C_d to the sensitivity parameter D_p, the energy dose E, and the formulation-dependent critical energy dose E_c [99].

$$C_d = D_p \ln\left(\frac{E}{E_c}\right) \tag{2.30}$$

Measurements of curje depth can be performed with increasing accuracy using calipers, stylus profilometry, or confocal laser scanning microscopy – although the increased accuracy also results in increased costs [100]. A simple way to perform cure depth measurements while building a Jacob's working curve was proposed by Rau et al. via photorheometric methods [82]. By performing SAOS measurements on a photorheometer, *in-situ* UV light via the UV accessory is introduced which partially solidifies the photocurable resin from the bottom up. Excess material is wiped from the rheometer plate post-cure, at which point the top geometry can be lowered until a designated axial force is reached. This axial force is indicative of the cure depth, and has been shown to work for filled and unfilled materials in addition to soft and stiff resins [82].

Chemorheological adaptations like these are useful for translating photorheometry results into printability findings, particularly if *in-situ* UV light is used to partially cure a material during DIW. The relationship between rheology and printability is hence discussed.

2.4.4 Rheology as Tool for Printability

Because rheology experiments require approximately a gram of material (compared to the dozens of grams required for printing studies), rheological methods to predict printability are highly desired – although understudied [81]. This section outlines common approaches to producing printability maps using rheological arguments. While many of the systems discussed here are highly filled composites, they are frequently inert, or the reaction kinetics were not discussed in detail. However, the methods outlined here set up discussions in 2.5 for highly filled, reactive systems which experience thixotropy.

Oftentimes, rheological arguments towards printability rely on the presence of a yield stress, which prevents flow through the nozzle without sufficient backpressures. Unfortunately, as illustrated in Figure 2.8 and explained by Hmeidat et al., even materials which exhibit a yield stress may fail to be printable [101]. For example, for the epoxy resin filled with various levels of nanoclay in Figure 2.8, the 0, 2.5, and 5 wt% samples were too fluidic to print. While expected for the 0 wt% sample (no presence of a yield stress), the 2.5 and 5 wt% samples clearly elicited yield stress behavior – to the point that the 5 wt% sample possessed a loss tangent less than unity.

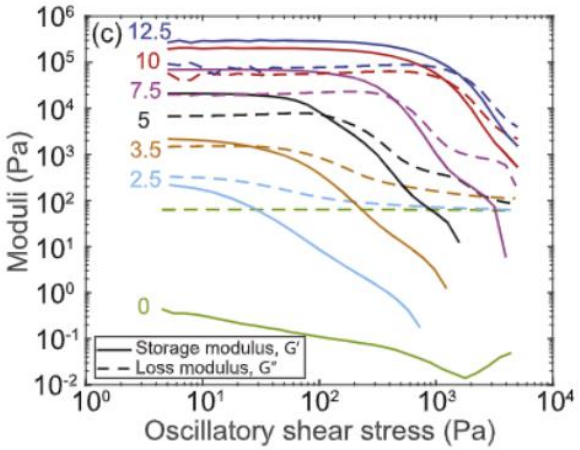

Figure 2.8: Illustration of yield stress materials which are not always printable (e.g. 0, 2.5, and 5 wt% nanoclay in Epon 826 epoxy resin), reprinted with permission from Hmeidat et al. [101].

The reason for this behavior is multifaceted, and likely requires arguments of the resting modulus/yield stress in addition to post-shear properties. This necessitates discussions of recoverability in addition to simple shear flow/oscillation studies. To begin, using the structural deformation parameters from three interval thixotropy testing outlined in Equations (2.18)-(2.21), it is possible to form printability maps which relate the relative solidity and degree of structural deformation. An example of this printability map is illustrated in Figure 2.9 [90].

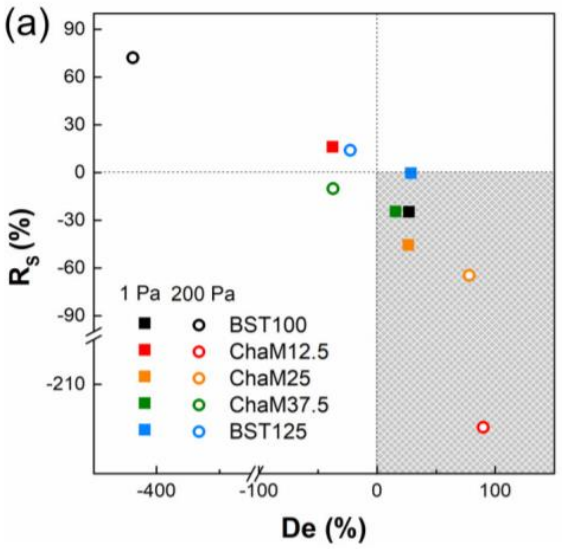

Figure 2.9: Printability maps (highlighted region) of various inks extruded at different pressures. BST125, ChaM25, and ChaM37.5 (materials containing varying amounts of glycerol, chalcogenidometallate, and solid BiSbTe filler) were the only printable materials, reprinted with permission from Eom et al. [90].

Studies like these indicate that printable materials require $R_s < 0\%$ to ensure that materials become fluidic during extrusion, and $D_e > 0\%$ to prevent network formation within the nozzle during deposition [90]. In other cases, printability maps may simply account for yield stress requirements. For example, Corker et al. stated that so long as the stress required for flow to occur $\sigma_F > 500$ Pa, the resting LVR storage modulus $G'_{rest} > 10{,}000$ Pa, and the flow transition index FTI = $\sigma_F/\sigma_{yield} \approx 20$, concentrated suspension of graphene oxide will be printable (see Figure 2.10) [79].

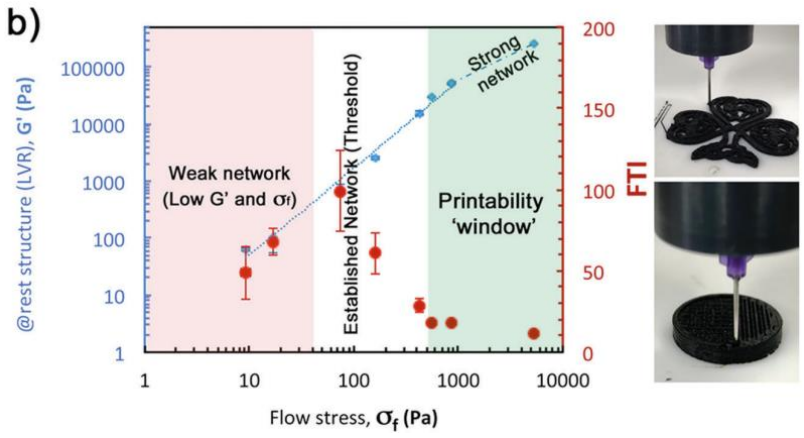

Figure 2.10: Printability map of concentrated graphene oxide suspensions using rheological arguments of yield stress and flow stress, reprinted with permission from Corker et al. [79].

While direct relationships between yield stress/recoverability requirements and printability might be expected, this is not always the case. For example, epoxy resins filled with either 10 wt% nanoclay (platelets) or 10 wt% fumed silica (spheres) were shown by Romberg et al. (2021) to experience non-linear relationships between peak stress hold times and recoverability during 3ITT, as elucidated in Figure 2.11 [102].

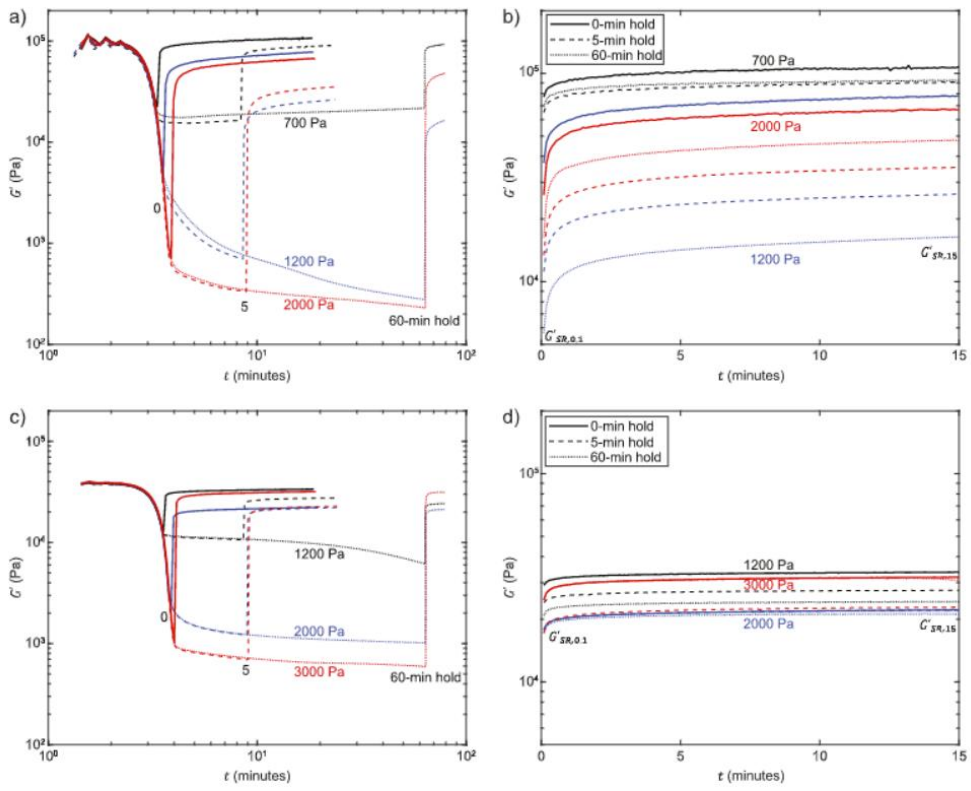

Figure 2.11: Three interval thixotropy tests for (a)-(b) 10 wt% nanoclay and (c)-(d) fumed silica dispersed in Epon 826 epoxy resin. Recoverability was non-linear with the imposed stress and peak-hold time, reprinted with permission from Romberg et al. [102].

These experiments indicate that filler materials with aspect ratios ≠ 1 induce time-dependent recovery, which is known to cause bulging/sag during prints. Because recoverability was non-linear with both peak hold time, the use of 3ITT in this case highlights the importance of matching shear stresses/times during rheological experiments to the shear stresses/times experienced during DIW. In some cases, this information can be used to build empirical equations for predicting buckling height (see Equation (2.31)) [102].

$$h_b = \left(7.8373\left(\frac{G'w^2}{6\rho g}\right)\left(\frac{1+\nu}{1-\nu^2}\right)\right)^{\frac{1}{3}} \tag{2.31}$$

In Equation (2.31), h_b is the buckling height, w is the line width, ρ is the density, g is the gravitation constant, and v is the Poisson ratio. While empirical equations such this are useful for specific materials and printing setups, they often lack the generalizability that printability maps provide. This finding is critical since a diverse set of curing mechanisms to prevent thixotropy exist; generalizable rheological models are necessary to capture the large array curing mechanisms available for reactive DIW.

2.5 Approaches for Improving Recoverability During DIW

Sections 2.1-2.4 have set up the motivation, fundamentals, and protocols for using rheology as a tool to predict printability in reactive, filled systems which experience time-dependent recovery post-extrusion. These discussions enable a review of the state-of-the-art advancements in DIW, with a specific focus on the relationship between rheology and printability for various curing mechanisms.

2.5.1 UV-Assisted Direct Ink Write

UV-assisted direct ink write (UV-DIW) is a well-established method for 3D printing filled and unfilled photocurable inks [77]. For unfilled photopolymers, UV light causes quick gelation during extrusion, which solidifies the ink and prevents sag on the build bed [77]. The presence of fillers, as previously mentioned, may block or absorb UV light resulting in a partial cure [97]. This partial cure provides green body during printing processes, which enables highly filled inks to be printable prior to post-processing techniques such as thermal cures.

Jiang et al. (2022) used a polyurethane acrylate (PUA) filled with fumed silica (FS) at 1, 3, 5, and 7 wt% to understand how percolating networks can form depending on the hydrophobicity of the system [103]. Because fumed silica is a nanoparticle, the amount of filler needed to attain

"highly filled" levels is significantly less than micron-scale counterparts [15]. It was shown that while hydrophilic FS in non-polar resins formed percolating networks (indicative of a highly filled system), hydrophobic FS in polar resins simply formed thin layers of film at the bottom of the resin. Using 3ITT, Figure 2.12 confirmed these findings, by suggesting that neat resins had similar viscoelastic properties to that of a 5 wt% hydrophobic FS; in contrast, hydrophilic FS experienced drastic growth in viscosity, and recovery could be tracked via steady shear 3ITT.

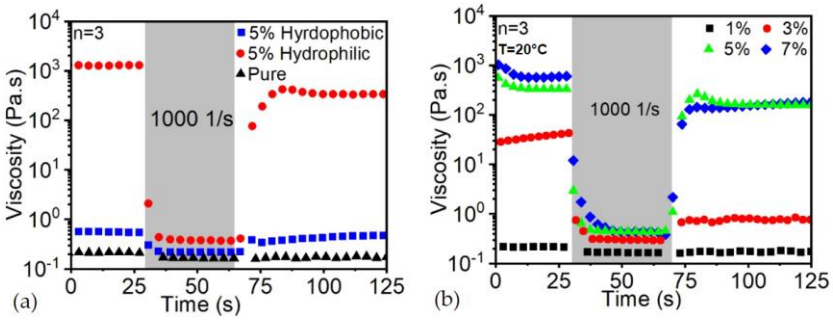

Figure 2.12: 3ITT of (a) hydrophobic and hydrophilic fumed silica composites and (b) hydrophilic composites at various concentrations, reprinted with permission from Jiang et al. [103].

UV-DIW printing studies showed good agreement with rheological experiments, specifically when correlating recoverability during 3ITT to print quality. Interestingly, silica content in excess of 3 wt% increased the presence of voids and the desired wall thickness due to swelling effects, illustrated in Figure 2.13.

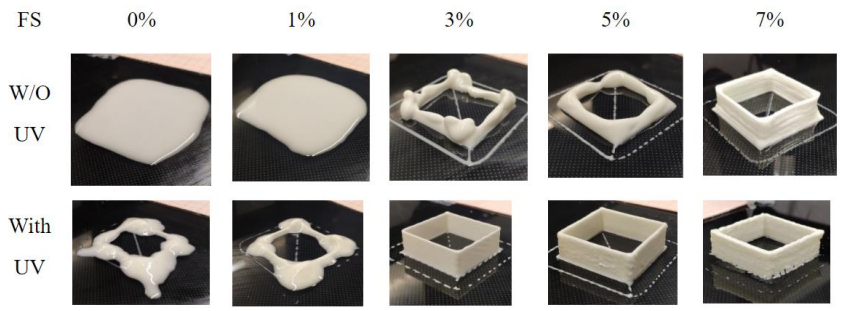

Figure 2.13: Highly filled FS composites at various concentrations with and without *in-situ* UV light, reprinted with permission from Jiang et al. [103].

The ratio of filler sizes can also influence overall printability and rheological properties. Ju et al. (2020) illustrated this finding by dispersing 5.5 μm and 20 nm ZrO_2 particles in 1,6-Hexanediol diacrylate (HDDA) at various bimodal distributions [104]. These materials were subjected to 3ITT and the structural recovery parameters *De*, *Rs*, and *Recs* (outlined in section 2.4.2) were used to create printability maps in Figure 2.14 (where N indicates the relative proportion of nanoparticles compared to microparticles). These findings suggest that printable inks generally have low levels of structural deformation, relative solidity levels between 0 and -100%, as well as structural recovery for the degree of solidity around 100% ± 20%.

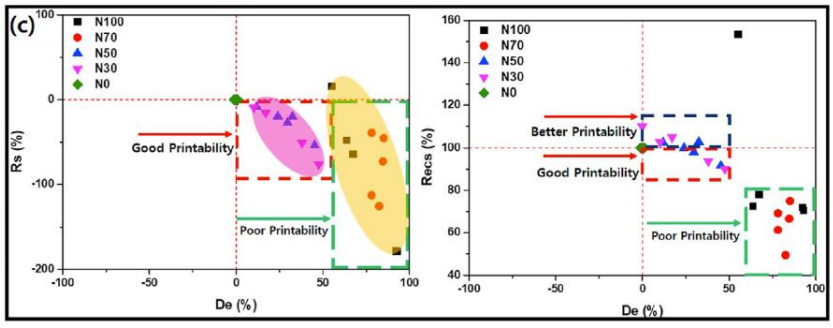

Figure 2.14: Printability maps created using structural recovery parameters from three interval thixotropy testing, reprinted with permission from Ju et al. [104].

From Figure 2.14, it is apparent that the 50:50 and 30:70 distributions generally outperform all other inks. Interestingly, when UV rheometry was used (60 seconds off, 10 seconds on, 60 seconds off in SAOS), materials with relatively higher amounts of nanoparticles saw jumps in tan(δ) during the 10 seconds of *in-situ* UV light. The authors attributed this finding to UV light being trapped between high density clusters of nanoparticles in bimodal settings, which increased the release of heat, thus causing the material to appear temporarily fluidic. This finding is illustrated in Figure 2.15 [104].

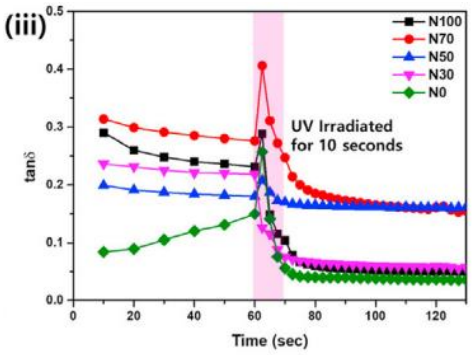

Figure 2.15: Temporary increases in fluidity during exposure to UV light caused by "trapping" of heated between clusters of nanoparticles, reprinted with permission from Ju et al. [104].

Ji et al. (2021) altered this approach by utilizing a photorheometer to introduce UV light during the second interval (high-strain period) [105]. Structural deformation parameters were used to create printability maps for 3Y-ZrO2 ceramic nanocomposite resins with HDDA monomers for UV-crosslinking capabilities. Both *Rs* and *Recs* were plotted as a function of *De*, although successful printability was attributed to the structural deformation parameter *De*; so long as *De* < ~60%, printability was considered "good." The results of photo-DSC studies, photorheology, and

these printability maps are shown in Figure 2.16, where WB represents the vol% of butoxyethanol diluent in the ink.

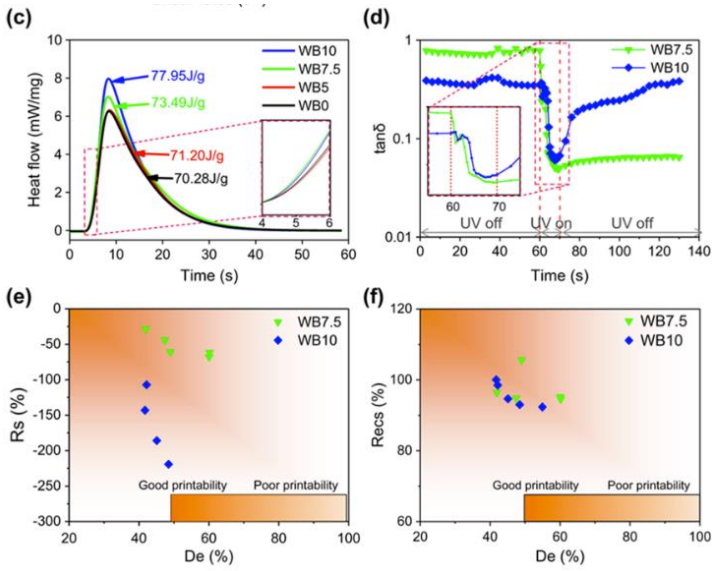

Figure 2.16: (a) Photo-DSC studies illustrating that higher concentrations of diluent increase exothermic peaks, (b) photorheology suggesting that excessive diluent causes fluidity after periods of high strain, and (c) printability maps using *Rs* as a function of *De*, as well as (d) *Recs* as a function of *De*, reprinted with permission from Ji et al. [105].

Campbell and Marnot (2021) used both a polyvinylpyrrolidone (PVP) resin and a bisphenol A-glycidyl methacrylate + triethylene glycol dimethacrylate resin to study both high molecular weight solvent evaporation and low molecular weight UV-curable systems, respectively [92]. These resins were filled with a bimodal distribution of 9-13 μm and 106-212 μm glass spheres at loading levels > 50 vol%. During direct ink write extrusion, only one distribution was deemed printable, and the line widths of all UV-curable systems were larger than the solvent evaporation inks. Rheological testing attributed this finding to large values of tan(δ) for photocuring inks, which was caused by an insufficiently fast cure post-deposition. Because the solvent evaporation

inks effectively start “curing” as soon as they are deposited, this can contribute to better bead shape retention. However, because some systems contain solvent-incompatible materials, these UV-reactive inks still show utility.

Similarly, bimodal distributions of nano-scale silica (12 nm) and styrene butadiene rubber (SBR, 122 nm) in 1-vinyl-2-pyrollidinone (NVP) + poly(ethylene glycol) diacrylate (PEGDA) were studied by Scott et al. (2020) for ex-situ UV-DIW [106]. By using process-relevant shear rates during rheological studies, it was found that at least a 30:70 ratio of silica:SBR was required for printability based on the presence of yield stresses. This precluded the use of low-viscosity inks for DIW, and enabled a rapid down selection of inks for printing studies and 3ITT recovery studies. Photorheology revealed that sufficient cure times and cure depths were possible for ex-situ DIW applications.

A study from Brooks et al. (2021) further explored comparisons of photocurable resins by analyzing differences between polycarbonatepoly(norbornene trimethyl carbonate) (PolyNTC) and poly(trimethylol propane allyl carbonate) (PolyTMPAC) [107]. They emphasized the use of lower viscosity resins, such as PolyTMPAC, for SLA applications, while reserving the high-viscosity PolyNTC resin for DIW extrusion. This study also emphasized how increasing the loading levels of solids causes a transition in fluidity from “liquid” to “toothpaste-like” when adding graphite nanoparticles. While this transition is useful for direct ink write, photorheology revealed that for gaps greater than 1 mm, incomplete cures occur, making UV-DIW difficult for these opaque systems. The presence of opaque fillers is known to reduce cure depth, but photorheology studies of hybridized DIW/VP from Rau et al. (2021) indicated that the addition of alumina can sometimes decrease the cure time of all-aromatic polyimides [108].

2.5.2 Thermosetting Reactions

Similar to UV-DIW, thermally-initiated crosslinking processes can assist in mitigating thixotropic effects by introducing chemical crosslinks to negate the time-dependent effects of interparticle recovery. The challenge here is calibrating and providing constant thermal energy during printing, similar to UV-DIW. Based on this challenge, the body of research focusing on *in-situ* or *ex-situ* thermal curing of highly filled systems is scarce.

Sarmah et al. (2022) addressed this issue by curing inks *ex-situ* via co-planar radio frequency (RF) ranging from 1-100 MHz [109]. 3ITT studies suggested that when filling a thermosetting epoxide with 3-10 wt% carbon nanotubes, a minimum loading level of 4 wt% filler was necessary to prevent fluidity post-shear. The presence of *ex-situ* RF increased the quality of DIW printed parts, as well as the number of layers before collapse.

Manning et al. (2019) explored the addition of 20 wt% nanoclay to Epon828 (a diglycidyl ether of bisphenol A), Jeffamine D230 (a polyether diamine), and a mono-ureidopyrimidinone-functionalized Jeffamine D230 [110]. Chemorheological analysis revealed that after 11 hours at room temperature, the *G'/G"* crossover was nearly reached, but the force transducer overloaded; this time period was considered the printability window based on these findings. Based on this long timeframe, a post-processing cure was chosen instead of an active curing protocol. Increased amounts of functionalized Jeffamine increased the yield stress and thixotropy as illustrated in Figure 2.17. This finding was attributed to the exposure of Ureidopyrimidinone groups to the outer edges of the printed beads during periods of high shear – especially through the nozzle after extrusion. This process formed hydrogen bonding between layers similar to hook-and-loop adhesives, which contributed to isotropic behavior during tensile testing.

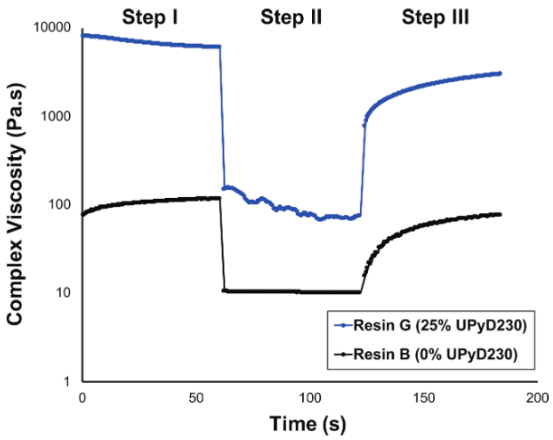

Figure 2.17: Decreases in recoverability attributed to migration of Ureidopyrimidinone groups during periods of high shear, reprinted with permission from Manning et al. [110].

The presence of fillers is known to slow down cure progress due to inhibition of free radical movement [111]. Interestingly, although smaller particles lead to more thixotropy, the size of particles has little effect on curing kinetics [112]. To avoid the potential interaction between cure kinetics and filler concentration, McKenzie et al. (2020) included low molecular weight gelators to promote yields stress behavior of inks, thus promoting shape retention post-extrusion [48]. While increasing the concentration of gelator increased the viscosity of the inks, start-stop deposition was difficult, leading to excessive flow out of the nozzle once the backpressure was halted. This can potentially be attributed to the lack of interparticle network recovery.

Thermal initiation of reactive fillers has also been studied to produce mechanically stable, thermally and electrically conductive structures [113]. By depositing Al/Zr/C nanocomposite inks onto a heated build bed, a complete conversion to Al and ZrC was obtained, producing multiphase microstructure. Further, the exothermic reaction of Zr and Al facilitated melting of AL, which contributed to quicker reactions of Zr and C. This concept of reactive extrusion is further explored in section 2.5.3.

2.5.3 Reactive Extrusion

Reactive ambient extrusion (RAM) poses a solution to many of the fallbacks present within thermally-reactive inks – specifically by producing printed parts in the absence of elevated temperatures. The goal of RAM is to mix two liquid-phase reactants *in-situ* within the nozzle of an extruder using a static mixer to enable curing on the build bed. This form of DIW permits material extrusion rates 350 times faster than standard FFF methods, while producing an isotropic printed part [114]. Rios et al. (2018) performed an analysis to predict printability of RAM inks based on chemorheological studies, which concluded that an initial $\tan(\delta) < 1.5$, an initial $G' >$ 2000 Pa, $G' > 1$ MPa after six minutes, and $G'' > 0.6$ after six minutes facilitated successful prints, as shown in Figure 2.18 [115].

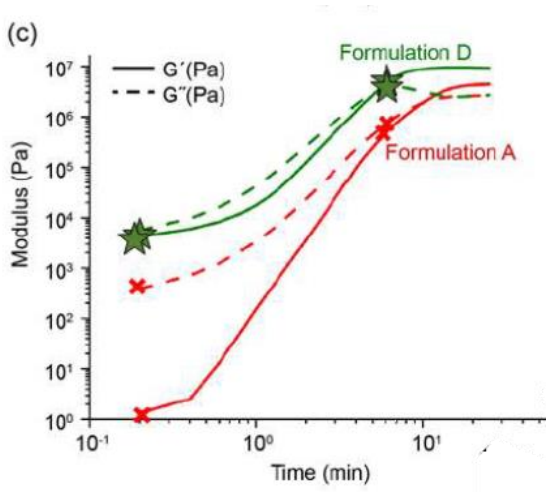

Figure 2.18*:* Chemorheology experiments indicating successful (formulation D) and unsuccessful (formulation A) inks for RAM, reprinted with permission from Rios et al. [115]

For reactions which take longer to fully cure, it becomes necessary to add fillers such that the interparticle network can impart a yield stress and thixotropy. This finding was explored by

Chen et al. (2020) by mixing a BPA-based epoxy resin with either a cyclo-aliphatic crosslinker or an aromatic crosslinker in addition to silica nanoparticles [116]. The amine groups in the cyclo-aliphatic crosslinker were shown to form hydrogen bonds with hydroxyl groups on the silica particles, which reduced the amount of solids loading required to form a yield stress compared to the aromatic crosslinker formulation. This finding emphasized the importance of surface chemistry when determining the amount of filler required to alter viscoelastic properties. As a more recent form of DIW additive manufacturing, the potential for scientific – specifically rheological – advancement in this area is significant.

2.5.4 Ionization

While much less studied than other variations of DIW, ionization can be utilized to induce viscoelastic properties necessary for extrusion. This concept was studied by Ju et al. (2021) who examined highly filled poly viny alcohol (PVA) hydrogels created using cellulose nanofibrils and metal cations [13]. The resulting hydrogels displayed deformation/reformation capabilities through a combination of metal-carboxylate coordination bonds, as well as borate ion complexes reacting with hydroxyl groups in the PVA. Printability maps using structural recovery parameters from 3ITT experiments established criteria for printable gels, where certain metal cations promoted faster recovery in the form of "self healing" [13].

In contrast to interpenetrating polymer networks created during gel formation, Nan et al. (2020) successfully 3D printed vertical pillars of hydroxypropyl methylcellulose (HPMC), polyethyleneimine (PEI), and titanium dioxide (TiO_2) [87]. The cationic polymer PEI can react with the outer surface of HPMC and added fillers to create an internal structure, whose recovery is concentration-dependent. Recovery of these inks during 3ITT was strongly dependent on PEI concentration. While inks without PEI recovered almost immediately, they lacked any structure

sufficient for 3D printing. Increasing the PEI concentration to 0.032 wt% resulted in 100% recovery within 330 seconds, but 0.068 wt% PEI only reacted 61% recovery within this timeframe; this finding reiterates the discussion of non-linearity at the end of section 2.4.4. This decrease in recovery was attributed to cationic-anionic interactions being "less accentuated due to the multibody effects," which also increased the risk of clogging as a result of faster flocculation. Printing results and relevant rheological tests are illustrated in Figure 2.19.

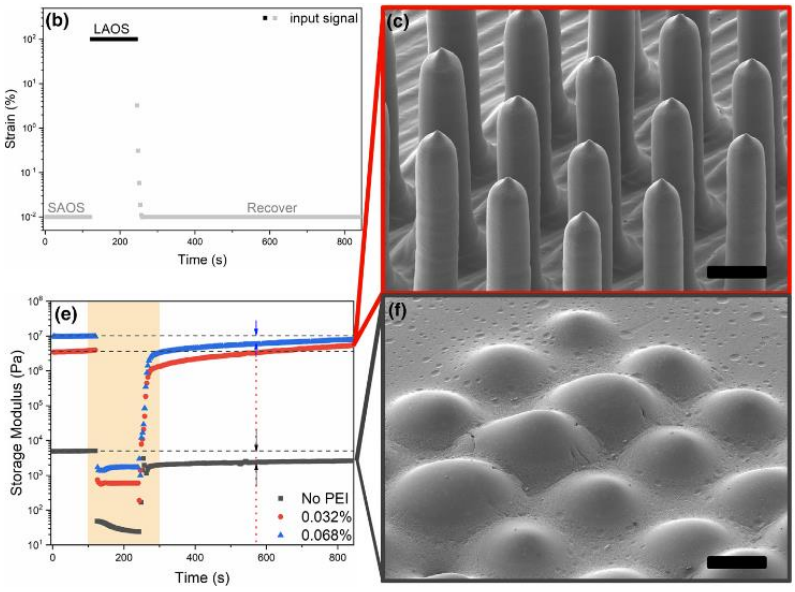

Figure 2.19*:* (Top Left) Changes in strain during 3ITT, (Bottom Left) 3ITT experiments for a range of PEI concentrations, (Top Right) SEM of 0.032 wt% PEI prints, and (Bottom Right) SEM of a poor quality print without any PEI, reprinted with permission from Nan et al. [87].

Silicon-carbide (63 vol%) filled polyelectrolyte complexes (PECs) were also shown to induce changes in recovery depending on the ratio of cationic to anionic groups [117]. Relatively higher concentrations of anionic compounds resulted in a higher modulus. In basic pH environments, this finding was accentuated due to larger zeta potentials (indicative of more colloidal stability). During alternating thixotropy tests (a form of 3ITT with added intervals), more

cationic systems recovered immediately. In contrast, more anionic inks failed to reach steady-state recovery until the second high-shear regime, suggesting that they were not as suitable for DIW studies.

2.5.5 Hydration

AM technologies using hydration as a form of recovery is largely dominated by industrial-scale concrete printing, which by itself is an entire field of research [118]. This method of freeform construction is in high demand due to the construction industry contributing towards nearly 80% of all waste in the world; automation of these technologies also aims to reduce hazards in the construction environment [118]. Especially considering the massive quantity of material required for these construction projects, rheology is a vital tool for downselecting potential cementitious pastes.

Cement, which is typically comprised of silicon and calcium oxides, is subject to interparticle network disruption due to particle de-agglomeration similar to DIW inks [119]. When forming concrete, non-reversible hydrate bridges form as a result of hydrate bonds between percolated cement particles [120]. The combined effects of thixotropy and chemical rigidification – resulting from cement hydration – complicates rheological studies of recovery, and necessitates novel approaches that hysteresis loops cannot capture [119]. For example, Figure 2.20 compares the recovery of calcium carbonate ($CaCO_3$) suspensions to cement pastes using SAOS measurements after a period of pre-shearing.

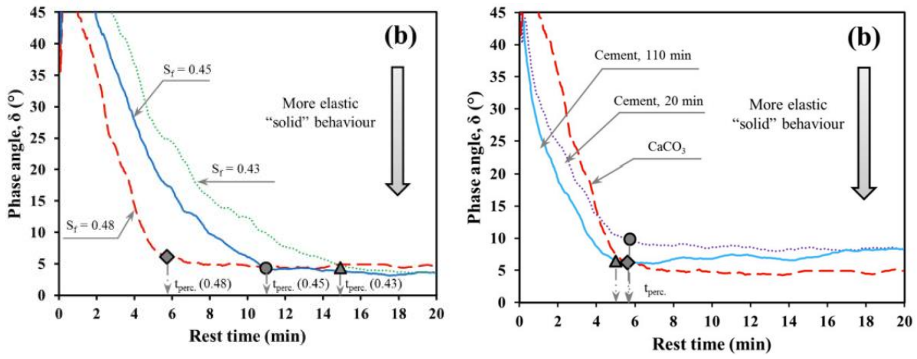

Figure 2.20*:* (Left) Solidification of $CaCO_3$ suspensions in water for volume fractions ranging from 43-48 vol%, (Right) $CaCO_3$ suspensions compared to general use cement (which experiences hydration reactions), at 48 vol% solids, for a variety of rest times prior to pre-shearing, reprinted with permission from Mostafa et al. [119].

This type of analysis aids the discussion of whether the physical rearrangement of particles or the chemical reaction is contributing more towards recovery. Since both systems exhibit thixotropy in the form of interparticle network recovery, but cements have an additional hydration reaction, the contribution of hydration towards solidification can be quantified. The use of representative, surrogate fillers is therefore a challenging yet imperative aspect of rheologically testing the printability of reactive inks.

To accelerate the aforementioned hydration reaction, other studies used a combination of fly ash, micro silica fume, and ground granulated blast-furnace slag (GGBS) to form a geopolymer [121]. While the combination of fly ash with GGBS produced the geopolymer, recovery of this system was still challenging, but was improved with a small proportion (<10 vol%) of silica fume. This research produced materials with denser microstructures compared to traditional cements, while unveiling the importance of studying physical/chemical reformation.

As stated, thixotropic effects of cement-based materials is an entire research area itself, and review articles are currently published which outline state-of-the-art advancements within this field [122]. This is extended to the field of ceramics, which, similar to cementitious pastes, contains its own breadth of research and journal outlets [5, 7, 12, 123].

2.5.6 Dual-Cure Mechanisms

The combination of curing mechanisms for advanced manufacturing is a growing field of interest for researchers who wish to balance green body strength during prints against desirable mechanical properties obtained during post-processing [124]. The advantage of this method, compared to a single-cure approach, is that *in-situ* UV cures can be used to partially cure the material during deposition, whereby a final thermal treatment can bond the layers together as a resulting from interpenetration of polymer chains [9]. De Marzi et al. (2022) presented evidence that this post-processing step can also alter optical properties of the printed part, transforming it from an opaque solid into a transparent solid, as shown in Figure 2.21.

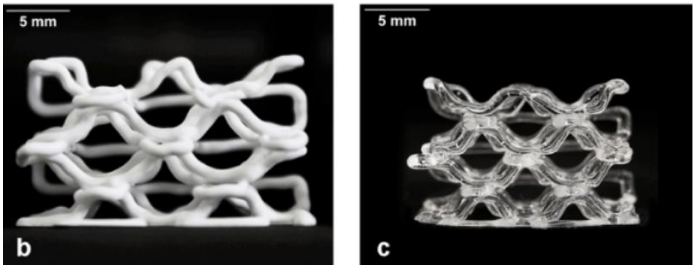

Figure 2.21: UV-DIW of a dual-cure material filled with 21 vol% fumed silica before (left) and after (right) post-processing pyrolysis, reprinted with permission from De Marzi et al. [125].

While this study emphasized the distinction between green body strength and final print properties, the relationship between rheology of the uncured ink, photorheometry, printability, and final print properties was not established. However, this study facilitates a discussion of which

component – from a rheological perspective – is most important towards building sufficient green body and final mechanical strength: the UV-curable resin or thermally-crosslinking resin?

This dual-cure approach to 3D printing epoxy/acrylate inks was explored by Kopatz et al. (2021) who studied the competing effects of UV/thermally curing systems using UV-DIW with a post thermal cure [124]. While relatively higher concentrations of thermally curing monomer dilute the acrylate, lowering the conversion and radical efficiency, the plasticizing effect can delay vitrification, thus increasing conversion. Additionally, at low loadings of epoxy where the plasticizing effect was minimal, higher UV intensities prevented vitrification through thermal effects of the UV lamp. In this regard, so long as no clogging occurred, higher UV intensities had generally more favorable outcomes. Many non-linearities were present within formulation-dependent gel times, cure times, and green body strengths, but the major finding was that mechanical properties post-thermal cure were insensitive to chemical formulation. This finding enabled formulation of epoxy/acrylate systems to be tailored purely on a basis of building green body strength for a specific application, while disregarding the effects formulation might play into final print properties. The insensitivity of acrylate composition towards final mechanical properties has been repeated for many different materials during dual-cure DIW, including diacrylate/diglycidyl either resins [9].

To combat the issue of nozzle clogging due to UV light, Tu et al. (2021) printed fumed silica-filled vinyl esters with both diphenyl(2,4,6-trimethylbenzoyl)phosphine oxide (TPO, photoinitiator) and tert-Butyl peroxybenzoate (TBPB, thermal initiator) using a UV-shielded nozzle, illustrated in Figure 2.22 [91]. The combination of UV-DIW and a post-thermal cure once again enabled sufficient green body strength during prints and subsequent desirable mechanical properties due to thermal crosslinking.

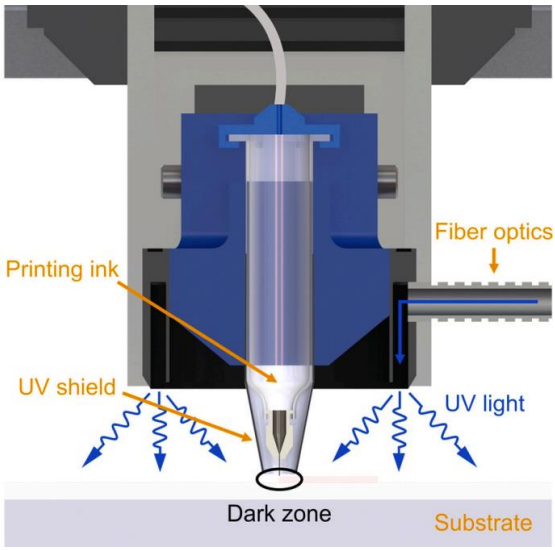

Figure 2.22: Prevention of clogging during UV-DIW using a shielded nozzle, reprinted with permission from Tu et al. [91].

Parts produced using this method possessed sufficiently high storage moduli on the order of 2-4 GPa, which were strong enough to be used as wrenches. Interestingly, this study asserted that the rheological requirements for inks to be printable in this setup were not “strict,” since “the additional UV-triggered radical curing reaction outside the dark zone for solidification" was sufficient [91].

In an effort to produce more isotropic parts, Chen et al. (2018) used a dual-cure approach to form IPNs via commercially available diacrylate/diglycidyl ether resins [20]. Because fumed silica is known to be UV transparent, its use for UV-DIW imparts desirable rheological properties while not influencing cure patterns. As a result, raster angle had no influence on tensile properties, and the presence of an IPN enabled shape memory properties when brought above and below the glass transition temperature.

2.6 References

[1] S. Singh, G. Singh, C. Prakash, S. Ramakrishna, Current status and future directions of fused filament fabrication, Journal of Manufacturing Processes 55 (2020) 288-306. https://doi.org/10.1016/j.jmapro.2020.04.049.
[2] S.B. Balani, F. Chabert, V. Nassiet, A. Cantarel, Influence of printing parameters on the stability of deposited beads in fused filament fabrication of poly (lactic) acid, Addit. Manuf. 25 (2019) 112-121. https://doi.org/10.1016/j.addma.2018.10.012.
[3] S. Liparoti, D. Sofia, A. Romano, F. Marra, R. Pantani, Fused filament deposition of PLA: the role of interlayer adhesion in the mechanical performances, Polymers 13(3) (2021) 399. https://doi.org/10.3390/polym13030399.
[4] J. Huang, Q. Qin, J. Wang, A review of stereolithography: Processes and systems, Processes 8(9) (2020) 1138. https://doi.org/10.3390/pr8091138.
[5] M. Schwentenwein, J. Homa, Additive manufacturing of dense alumina ceramics, Int. J. Appl. Ceram. Technol. 12(1) (2015) 1-7. https://doi.org/10.1111/ijac.12319.
[6] P.F. O'Neill, N. Kent, D. Brabazon, Mitigation and control of the overcuring effect in mask projection micro-stereolithography, AIP Conference Proceedings, AIP Publishing LLC, 2017, p. 200012. https://doi.org/10.1063/1.5008249.
[7] A. M'barki, L. Bocquet, A. Stevenson, Linking rheology and printability for dense and strong ceramics by direct ink writing, Sci. Rep. 7(1) (2017) 1-10. https://doi.org/10.1038/s41598-017-06115-0.
[8] I. Gibson, D. Rosen, B. Stucker, M. Khorasani, Direct write technologies, Additive Manufacturing Technologies, Springer2015, pp. 319-345.
[9] M. Invernizzi, G. Natale, M. Levi, S. Turri, G. Griffini, UV-assisted 3D printing of glass and carbon fiber-reinforced dual-cure polymer composites, Materials 9(7) (2016) 583. https://doi.org/10.3390/ma9070583.
[10] J.I. Lipton, M. Cutler, F. Nigl, D. Cohen, H. Lipson, Additive manufacturing for the food industry, Trends Food Sci. Technol. 43(1) (2015) 114-123. https://doi.org/10.1016/j.tifs.2015.02.004.
[11] N.V. Muravyev, K.A. Monogarov, U. Schaller, I.V. Fomenkov, A.N. Pivkina, Progress in additive manufacturing of energetic materials: Creating the reactive microstructures with high potential of applications, Propellants Explos. Pyrotech. 44(8) (2019) 941-969. https://doi.org/10.1002/prep.201900060.
[12] S.S. Chan, R.M. Pennings, L. Edwards, G.V. Franks, 3D printing of clay for decorative architectural applications: Effect of solids volume fraction on rheology and printability, Addit. Manuf. 35 (2020) 101335. https://doi.org/10.1016/j.addma.2020.101335.
[13] Y. Ju, J. Ha, Y. Song, D. Lee, Revealing the enhanced structural recovery and gelation mechanisms of cation-induced cellulose nanofibrils composite hydrogels, Carbohydr. Polym. 272 (2021) 118515. https://doi.org/10.1016/j.carbpol.2021.118515.
[14] R. Duballet, O. Baverel, J. Dirrenberger, Classification of building systems for concrete 3D printing, Autom. Constr. 83 (2017) 247-258. https://doi.org/10.1016/j.autcon.2017.08.018.
[15] M.M. Rueda, M.-C. Auscher, R. Fulchiron, T. Perie, G. Martin, P. Sonntag, P. Cassagnau, Rheology and applications of highly filled polymers: A review of current understanding, Prog. Polym. Sci. 66 (2017) 22-53. https://doi.org/10.1016/j.progpolymsci.2016.12.007.
[16] M. Paulino, F. Teixeira-Dias, On the use of polyurethane foam paddings to improve passive safety in crashworthiness applications, Polyurethane (2012). https://doi.org/10.5772/47996.

[17] J.O. Akindoyo, M.D. Beg, S. Ghazali, M.R. Islam, N. Jeyaratnam, A.R. Yuvaraj, Polyurethane types, synthesis and applications–a review, RSC Adv. 6(115) (2016) 114453-114482. https://doi.org/10.1039/C6RA14525F.
[18] S. Chaturvedi, P.N. Dave, Solid propellants: AP/HTPB composite propellants, Arabian J. Chem. 12(8) (2019) 2061-2068. https://doi.org/10.1016/j.arabjc.2014.12.033.
[19] V. Sekkar, S. Venkatachalam, K.N. Ninan, Rheokinetic studies on the formation of urethane networks based on hydroxyl terminated polybutadiene, Eur. Polym. J. 38(1) (2002) 169-178. https://doi.org/10.1016/S0014-3057(01)00106-9.
[20] K. Chen, X. Kuang, V. Li, G. Kang, H.J. Qi, Fabrication of tough epoxy with shape memory effects by UV-assisted direct-ink write printing, Soft Matter 14(10) (2018) 1879-1886. https://doi.org/10.1039/c7sm02362f.
[21] S. Garino, P. Antonaci, D. Pastrone, M. Sangermano, F. Maggi, Photo-polymerization for additive manufacturing of composite solid propellants, Acta Astronaut. 182 (2021) 58-65. https://doi.org/10.1016/j.actaastro.2021.01.062.
[22] A. Kumar, R.K. Gupta, Fundamentals of Polymers, McGraw-Hill 1998.
[23] J. Guo, T. Chai, Y. Liu, J. Cui, H. Ma, S. Jing, L. Zhong, S. Qin, G. Wang, X. Ren, Kinetic research on the curing reaction of hydroxyl-terminated polybutadiene based polyurethane binder system via FT-IR measurements, Coatings 8(5) (2018) 175. https://doi.org/10.3390/coatings8050175.
[24] M.A. Pérez-Limiñana, F. Arán-Aís, A.M. Torró-Palau, C. Orgilés-Barcel, J.M. Martín-Martínez, Influence of the hard-to-soft segment ratio on the adhesion of water-borne polyurethane adhesive, J. Adhes. Sci. Technol. 21(8) (2007) 755-773. https://doi.org/10.1163/156856107781362635.
[25] D. Nichetti, S. Cossar, N. Grizzuti, Effects of molecular weight and chemical structure on phase transition of thermoplastic polyurethanes, J. Rheol. 49(6) (2005) 1361-1376. https://doi.org/10.1122/1.2071987.
[26] J. Silva, D. Meltzer, J. Liu, M. Cox, J. Maia, The influence of thermo-mechanical history on structure development of elastomeric and amorphous glass thermoplastic polyurethanes, Polymer Engineering & Science 54(6) (2014) 1383-1393. https://doi.org/10.1002/pen.23673.
[27] C. Korah Bina, K. Kannan, K. Ninan, DSC study on the effect of isocyanates and catalysts on the HTPB cure reaction, J. Therm. Anal. Calorim. 78(3) (2004) 753-760. https://doi.org/10.1007/s10973-005-0442-0.
[28] M. Hui, L. Yu-Cun, C. Tao, H. Tuo-Ping, G. Jia-Hu, Y. Yan-Wu, Y. Jun-Ming, W. Jian-Hua, Q. Ning, Z. Liang, Kinetic studies on the cure reaction of hydroxyl-terminated polybutadiene based polyurethane with variable catalysts by differential scanning calorimetry, e-Polymers 17(1) (2017) 89-94. https://doi.org/10.1515/epoly-2016-0245.
[29] B. Lucio, J.L. de la Fuente, Chemorheology and Kinetics of High-Performance Polyurethane Binders Based on HMDI, Macromol. Mater. Eng. 306(3) (2021) 2000617. https://doi.org/10.1002/mame.202000617.
[30] B. Lucio, J.L. de la Fuente, Kinetic and chemorheological modelling of the polymerization of 2, 4-Toluenediisocyanate and ferrocene-functionalized hydroxyl-terminated polybutadiene, Polymer 140 (2018) 290-303. https://doi.org/10.1016/j.polymer.2018.02.058.
[31] B. Lucio, J.L. de la Fuente, Non-isothermal DSC and rheological curing of ferrocene-functionalized, hydroxyl-terminated polybutadiene polyurethane, React. Funct. Polym. 107 (2016) 60-68. https://doi.org/10.1016/j.reactfunctpolym.2016.08.002.

[32] B. Lucio, J.L. de la Fuente, Rheokinetic analysis on the formation of metallo-polyurethanes based on hydroxyl-terminated polybutadiene, Eur. Polym. J. 50 (2014) 117-126. https://doi.org/10.1016/j.eurpolymj.2013.10.013.
[33] B. Lucio, J.L. de la Fuente, Rheological cure characterization of an advanced functional polyurethane, Thermochim. Acta 596 (2014) 6-13. https://doi.org/10.1016/j.tca.2014.09.012.
[34] A. Shenoy, Thermoplastic melt rheology and processing, CRC Press 1996.
[35] G. Kim, E. Barocio, R.B. Pipes, R. Sterkenburg, 3D printed thermoplastic polyurethane bladder for manufacturing of fiber reinforced composites, Addit. Manuf. 29 (2019) 100809. https://doi.org/10.1016/j.addma.2019.100809.
[36] T. Xu, W. Shen, X. Lin, Y.M. Xie, Mechanical properties of additively manufactured thermoplastic polyurethane (TPU) material affected by various processing parameters, Polymers 12(12) (2020) 3010. https://doi.org/10.3390/polym12123010.
[37] X. Lin, P. Coates, M. Hebda, R. Wang, Y. Lu, L. Zhang, Experimental analysis of the tensile property of FFF-printed elastomers, Polym. Test. 90 (2020) 106687. https://doi.org/10.1016/j.polymertesting.2020.106687.
[38] Y.-H. Que, Y. Shi, L.-Z. Liu, Y.-X. Wang, C.-C. Wang, H.-C. Zhang, X.-Y. Han, The Crystallisation, Microphase Separation and Mechanical Properties of the Mixture of Ether-Based TPU with Different Ester-Based TPUs, Polymers 13(20) (2021) 3475. https://doi.org/10.3390/polym13203475.
[39] Thermoplastic Polyurethane (TPU) processing guide. https://www.fostercomp.com/wp-content/uploads/2018/11/Foster-TPU-Processing-Guidelines.pdf.
[40] G. Lu, D.M. Kalyon, I. Yilgör, E. Yilgör, Rheology and extrusion of medical-grade thermoplastic polyurethane, Polymer Engineering & Science 43(12) (2003) 1863-1877. https://doi.org/10.1002/pen.10158.
[41] A.M. Heintz, D.J. Duffy, S.L. Hsu, W. Suen, W. Chu, C.W. Paul, Effects of reaction temperature on the formation of polyurethane prepolymer structures, Macromolecules 36(8) (2003) 2695-2704. https://doi.org/10.1021/MA021559H.
[42] Y. Suryawanshi, P. Sanap, V. Wani, Advances in the synthesis of non-isocyanate polyurethanes, Polym. Bull. 76 (2019) 3233-3246. https://doi.org/doi.org/10.1007/S00289-018-2531-7.
[43] E. Delebecq, J.-P. Pascault, B. Boutevin, F. Ganachaud, On the versatility of urethane/urea bonds: reversibility, blocked isocyanate, and non-isocyanate polyurethane, Chem. Rev. 113(1) (2013) 80-118. https://doi.org/10.1021/cr300195n.
[44] J.N. Gibb, J.M. Goodman, The formation of high-purity isocyanurate through proazaphosphatrane-catalysed isocyanate cyclo-trimerisation: computational insights, Organic & Biomolecular Chemistry 11(1) (2013) 90-97. https://doi.org/10.1039/C2OB26547H.
[45] Merriam-Webster, Rheology, Merriam-Webster.com dictionary, Merriam-Webster, 2023.
[46] H.H. Barnes, J.F. Hutton, K. Walters, An Introduction to Rheology, Elsevier, Amsterdam, 1989.
[47] F.A. Morrison, Understanding rheology, Oxford university press New York 2001.
[48] R. McKenzie, H. Koerner, Enabling direct writing of an epoxy resin with thermo-activated organic thixotropes, Addit. Manuf. 31 (2020) 100905. https://doi.org/10.1016/j.addma.2019.100905.
[49] A.V. Shenoy, Rheology of filled polymer systems, 1 ed., Springer Science & Business Media 1999.

[50] M. Bek, J. Gonzalez-Gutierrez, C. Kukla, K. Pušnik Črešnar, B. Maroh, L. Slemenik Perše, Rheological behaviour of highly filled materials for injection moulding and additive manufacturing: effect of particle material and loading, Applied Sciences 10(22) (2020) 7993. https://doi.org/10.3390/app10227993.
[51] J. Walberer, A.J. McHugh, The linear viscoelastic behavior of highly filled polydimethylsiloxane measured in shear and compression, J. Rheol. 45(1) (2001) 187-201. https://doi.org/10.1122/1.1332386.
[52] S. Richter, M. Saphiannikova, K.W. Stöckelhuber, G. Heinrich, Jamming in filled polymer systems, Macromol. Symp., Wiley Online Library, 2010, pp. 193-201. https://doi.org/10.1002/masy.201050523.
[53] B.K. Aral, D.M. Kalyon, Viscoelastic material functions of noncolloidal suspensions with spherical particles, J. Rheol. 41(3) (1997) 599-620. https://doi.org/10.1122/1.550841.
[54] H.M. Wyss, E.V. Tervoort, L.J. Gauckler, Mechanics and microstructures of concentrated particle gels, J. Am. Ceram. Soc. 88(9) (2005) 2337-2348. https://doi.org/10.1111/j.1551-2916.2005.00622.x.
[55] J. Meier, J. Reynolds, S. Whalen, J. Patel, M.J. Bortner, G. Young, Improved Hybrid Rocket Performance by Additively Manufactured Gel-Infused Solid Fuels, J. Propul. Power (2022) 1-9. https://doi.org/10.2514/1.B38773.
[56] S.A. Gulmus, U. Yilmazer, Effect of volume fraction and particle size on wall slip in flow of polymeric suspensions, J. Appl. Polym. Sci. 98(1) (2005) 439-448. https://doi.org/10.1002/app.21928.
[57] J. Mewis, A. Spaull, Rheology of concentrated dispersions, Adv. Colloid Interface Sci. 6(3) (1976) 173-200. https://doi.org/10.1016/0001-8686(76)80008-5.
[58] R.G. Larson, Y. Wei, A review of thixotropy and its rheological modeling, J. Rheol. 63(3) (2019) 477-501. https://doi.org/10.1122/1.5055031.
[59] V.G. Kulichikhin, A.Y. Malkin, The Role of Structure in Polymer Rheology, Polymers 14(6) (2022) 1262. https://doi.org/10.3390/polym14061262.
[60] M. Folkes, Polymer engineering composites, Applied Science Publishers Ltd., London, 1979.
[61] H. Barnes, Thixotropy-A review, Journal of non-Newtonian fluid mechanics 70(97) (1997) 1-33. https://doi.org/10.1016/S0377-0257(97)00004-9.
[62] F. Rubio-Hernández, J. Sánchez-Toro, N. Páez-Flor, Testing shear thinning/thixotropy and shear thickening/antithixotropy relationships in a fumed silica suspension, J. Rheol. 64(4) (2020) 785-797. https://doi.org/10.1122/1.5131852.
[63] P.R. de Souza Mendes, R.L. Thompson, A critical overview of elasto-viscoplastic thixotropic modeling, Journal of Non-Newtonian Fluid Mechanics 187 (2012) 8-15. https://doi.org/10.1016/j.jnnfm.2012.08.006.
[64] A. Mujumdar, A.N. Beris, A.B. Metzner, Transient phenomena in thixotropic systems, Journal of Non-Newtonian Fluid Mechanics 102(2) (2002) 157-178. https://doi.org/10.1016/s0377-0257(01)00176-8.
[65] O.S. Toker, S. Karasu, M.T. Yilmaz, S. Karaman, Three interval thixotropy test (3ITT) in food applications: A novel technique to determine structural regeneration of mayonnaise under different shear conditions, Food Res. Int. 70 (2015) 125-133. https://doi.org/10.1016/j.foodres.2015.02.002.

[66] C.E. Cipriani, Y. Shu, E.B. Pentzer, C.C. Benjamin, Viscoelastic and thixotropic characterization of paraffin/photopolymer composites for extrusion-based printing, Physics of Fluids 34(9) (2022) 093106. https://doi.org/10.3390/sym13101767.
[67] O. Ojeda-Farías, P. Hebraud, D. Lootens, M. Liard, J. Mendoza-Rangel, Thixotropy of reactive suspensions: The case of cementitious materials, Constr. Build. Mater. 212 (2019) 121-129. https://doi.org/10.1016/j.conbuildmat.2019.03.319.
[68] J. Mewis, N.J. Wagner, Thixotropy, Adv. Colloid Interface Sci. 147 (2009) 214-227. https://doi.org/10.1016/j.cis.2008.09.005.
[69] S. Jamali, G.H. McKinley, The Mnemosyne number and the rheology of remembrance, J. Rheol. 66(5) (2022) 1027-1039. https://doi.org/10.1122/8.0000432.
[70] U. Yilmazer, D.M. Kalyon, Slip effects in capillary and parallel disk torsional flows of highly filled suspensions, J. Rheol. 33(8) (1989) 1197-1212. https://doi.org/10.1122/1.550049.
[71] D.M. Kalyon, P. Yaras, B. Aral, U. Yilmazer, Rheological behavior of a concentrated suspension: A solid rocket fuel simulant, J. Rheol. 37(1) (1993) 35-53. https://doi.org/10.1122/1.550435.
[72] M. Patel, S. Blackburn, D.I. Wilson, Modelling of paste ram extrusion subject to liquid phase migration and wall friction, Chem. Eng. Sci. 172 (2017) 487-502. https://doi.org/10.1016/j.ces.2017.07.001.
[73] D. Wilson, S. Rough, Exploiting the curious characteristics of dense solid–liquid pastes, Chem. Eng. Sci. 61(13) (2006) 4147-4154. https://doi.org/10.1016/j.ces.2005.10.032.
[74] S. Rough, J. Bridgwater, D. Wilson, Effects of liquid phase migration on extrusion of microcrystalline cellulose pastes, Int. J. Pharm. 204(1-2) (2000) 117-126. https://doi.org/10.1016/S0378-5173(00)00478-6.
[75] M. Patel, S. Blackburn, D.I. Wilson, Modelling of paste flows subject to liquid phase migration, International journal for numerical methods in engineering 72(10) (2007) 1157-1180. https://doi.org/10.1002/nme.2040.
[76] T. Beran, T. Mulholland, F. Henning, N. Rudolph, T.A. Osswald, Nozzle clogging factors during fused filament fabrication of spherical particle filled polymers, Addit. Manuf. 23 (2018) 206-214. https://doi.org/10.1016/j.addma.2018.08.009.
[77] D.A. Rau, J. Herzberger, T.E. Long, C.B. Williams, Ultraviolet-assisted direct ink write to additively manufacture all-aromatic polyimides, ACS Appl. Mater. Interfaces 10(41) (2018) 34828-34833. https://doi.org/10.1021/acsami.8b14584.
[78] H. Ji, J. Zhao, J. Chen, S. Shimai, J. Zhang, Y. Liu, D. Liu, S. Wang, A novel experimental approach to quantitatively evaluate the printability of inks in 3D printing using two criteria, Addit. Manuf. 55 (2022) 102846. https://doi.org/10.1016/j.addma.2022.102846.
[79] A. Corker, H.C.-H. Ng, R.J. Poole, E. García-Tuñón, 3D printing with 2D colloids: Designing rheology protocols to predict 'printability'of soft-materials, Soft Matter 15(6) (2019) 1444-1456. https://doi.org/10.1039/c8sm01936c.
[80] I. Gunduz, M. McClain, P. Cattani, G.-C. Chiu, J. Rhoads, S. Son, 3D printing of extremely viscous materials using ultrasonic vibrations, Addit. Manuf. 22 (2018) 98-103. https://doi.org/10.1016/j.addma.2018.04.029.
[81] L. del-Mazo-Barbara, M.-P. Ginebra, Rheological characterisation of ceramic inks for 3D direct ink writing: A review, J. Eur. Ceram. Soc. 41(16) (2021) 18-33. https://doi.org/10.1016/j.jeurceramsoc.2021.08.031.

[82] D.A. Rau, J.P. Reynolds, J.S. Bryant, M.J. Bortner, C.B. Williams, A rheological approach for measuring cure depth of filled and unfilled photopolymers at additive manufacturing relevant length scales, Addit. Manuf. 60 (2022) 103207. https://doi.org/10.1016/j.addma.2022.103207.
[83] A. Paar, Basics of Thixotropy, 2022. https://wiki.anton-paar.com/en/basics-of-thixotropy/.
[84] T. Instruments, Introduction to Thixotropy Analysis Using a Rotational Rheometer, 2000. https://www.tainstruments.com/pdf/literature/RH106.pdf.
[85] M. Dinkgreve, M. Fazilati, M. Denn, D. Bonn, Carbopol: From a simple to a thixotropic yield stress fluid, J. Rheol. 62(3) (2018) 773-780. https://doi.org/10.1122/1.5016034.
[86] Y. Chen, Y. Wang, Q. Yang, Y. Liao, B. Zhu, G. Zhao, R. Shen, X. Lu, S. Qu, A novel thixotropic magnesium phosphate-based bioink with excellent printability for application in 3D printing, J. Mater. Chem. B 6(27) (2018) 4502-4513. https://doi.org/10.1039/c8tb01196f.
[87] B. Nan, F.J. Galindo-Rosales, J.M. Ferreira, 3D printing vertically: Direct ink writing free-standing pillar arrays, Mater. Today 35 (2020) 16-24. https://doi.org/10.1016/j.mattod.2020.01.003.
[88] J.T. Kolawole, R. Combrinck, W.P. Boshoff, Rheo-viscoelastic behaviour of fresh cement-based materials: Cement paste, mortar and concrete, Constr. Build. Mater. 248 (2020) 118667. https://doi.org/10.1016/j.conbuildmat.2020.118667.
[89] H. Hong, H. Jiyong, K.-S. Moon, X. Yan, C.-p. Wong, Rheological properties and screen printability of UV curable conductive ink for flexible and washable E-textiles, J. Mater. Sci. Technol. 67 (2021) 145-155. https://doi.org/10.1016/j.jmst.2020.06.033.
[90] Y. Eom, F. Kim, S.E. Yang, J.S. Son, H.G. Chae, Rheological design of 3D printable all-inorganic inks using BiSbTe-based thermoelectric materials, J. Rheol. 63(2) (2019) 291-304. https://doi.org/10.1122/1.5058078.
[91] R. Tu, H.A. Sodano, Additive manufacturing of high-performance vinyl ester resin via direct ink writing with UV-thermal dual curing, Addit. Manuf. 46 (2021) 102180. https://doi.org/10.1016/j.addma.2021.102180.
[92] I. Campbell, A. Marnot, M. Ketcham, C. Travis, B. Brettmann, Direct ink write 3D printing of high solids loading bimodal distributions of particles, AlChE J. 67(12) (2021) e17412. https://doi.org/10.1002/aic.17412.
[93] M.J. Bortner, V. Bhanu, J.E. McGrath, D.G. Baird, Shear rheological properties of acrylic copolymers and terpolymers suitable for potentially melt processable carbon fiber precursors, J. Appl. Polym. Sci. 93(6) (2004) 2856-2865. https://doi.org/10.1002/app.20833.
[94] V. Sekkar, T.S.K. Raunija, Issues Related with Pot Life Extension for Hydroxyl-Terminated Polybutadiene-Based Solid Propellant Binder System, Propellants Explos. Pyrotech. 40(2) (2015) 267-274. https://doi.org/10.1002/prep.201400054.
[95] G. Santhosh, S. Reshmi, C.R. Nair, Rheokinetic characterization of polyurethane formation in a highly filled composite solid propellant, J. Therm. Anal. Calorim. 140(1) (2020) 213-223. https://doi.org/10.1007/s10973-019-08793-6.
[96] A. Olejnik, K. Gosz, Ł. Piszczyk, Kinetics of cross-linking processes of fast-curing polyurethane system, Thermochim. Acta 683 (2020) 178435. https://doi.org/10.1016/j.tca.2019.178435.
[97] M.S. McClain, A. Afriat, J.F. Rhoads, I.E. Gunduz, S.F. Son, Development and characterization of a photopolymeric binder for additively manufactured composite solid propellant using vibration assisted printing, Propellants Explos. Pyrotech. 45(6) (2020) 853-863. https://doi.org/10.1002/prep.201900387.

[98] A.K. Mahanta, D.D. Pathak, HTPB-polyurethane: a versatile fuel binder for composite solid propellant, Polyurethane 1 (2012). https://doi.org/10.5772/47995.
[99] J.W. Halloran, V. Tomeckova, S. Gentry, S. Das, P. Cilino, D. Yuan, R. Guo, A. Rudraraju, P. Shao, T. Wu, Photopolymerization of powder suspensions for shaping ceramics, J. Eur. Ceram. Soc. 31(14) (2011) 2613-2619. https://doi.org/a10.1016/j.jeurceramsoc.2010.12.003.
[100] J. Bennett, Measuring UV curing parameters of commercial photopolymers used in additive manufacturing, Addit. Manuf. 18 (2017) 203-212. https://doi.org/10.1016/j.addma.2017.10.009.
[101] N.S. Hmeidat, J.W. Kemp, B.G. Compton, High-strength epoxy nanocomposites for 3D printing, Compos. Sci. Technol. 160 (2018) 9-20. https://doi.org/10.1016/j.compscitech.2018.03.008.
[102] S.K. Romberg, M.A. Islam, C.J. Hershey, M. DeVinney, C.E. Duty, V. Kunc, B.G. Compton, Linking thermoset ink rheology to the stability of 3D-printed structures, Addit. Manuf. 37 (2021) 101621. https://doi.org/10.1016/j.addma.2020.101621.
[103] F. Jiang, M. Zhou, D. Drummer, Effects of Fumed Silica on Thixotropic Behavior and Processing Window by UV-Assisted Direct Ink Writing, Polymers 14(15) (2022) 3107. https://doi.org/10.3390/polym14153107.
[104] Y. Ju, J. Ha, Y. Song, J.S. Yun, D. Lee, Optimizing the printability and dispersibility of functionalized zirconium oxide/acrylate composites with various nano-to micro-particle ratios, Ceram. Int. 46(17) (2020) 26903-26910. https://doi.org/10.1016/j.ceramint.2020.07.168.
[105] S.H. Ji, D.S. Kim, M.S. Park, D. Lee, J.S. Yun, Development of multicolor 3D-printed 3Y-ZrO2 sintered bodies by optimizing rheological properties of UV-curable high-content ceramic nanocomposites, Mater. Des. 209 (2021) 109981. https://doi.org/10.1016/j.matdes.2021.109981.
[106] P.J. Scott, D.A. Rau, J. Wen, M. Nguyen, C.R. Kasprzak, C.B. Williams, T.E. Long, Polymer-inorganic hybrid colloids for ultraviolet-assisted direct ink write of polymer nanocomposites, Addit. Manuf. 35 (2020) 101393. https://doi.org/10.1016/j.addma.2021.101996.
[107] S. Brooks, Z. Cartwright, D. Merckle, A.C. Weems, 4D Aliphatic photopolymer polycarbonates as direct ink writing of biodegradable, conductive graphite-composite materials, Polym. Compos. 42(10) (2021) 5134-5143. https://doi.org/10.1002/pc.26211.
[108] D.A. Rau, M. Forgiarini, C.B. Williams, Hybridizing Direct Ink Write and mask-projection Vat Photopolymerization to enable additive manufacturing of high viscosity photopolymer resins, Addit. Manuf. 42 (2021) 101996. https://doi.org/10.1016/j.addma.2021.101996.
[109] A. Sarmah, S.K. Desai, A.G. Crowley, G.C. Zolton, G.B. Tezel, E.M. Harkin, T.Q. Tran, K. Arole, M.J. Green, Additive manufacturing of nanotube-loaded thermosets via direct ink writing and radio-frequency heating and curing, Carbon 200 (2022) 307-316. https://doi.org/10.1016/j.carbon.2022.08.063.
[110] K.B. Manning, N. Wyatt, L. Hughes, A. Cook, N.H. Giron, E. Martinez, C.G. Campbell, M.C. Celina, Self assembly–assisted additive manufacturing: direct ink write 3D printing of epoxy–amine thermosets, Macromol. Mater. Eng. 304(3) (2019) 1800511. https://doi.org/10.1002/mame.201800511.
[111] F. Liu, W. Yu, Y. Wang, R. Shang, Q. Zheng, Curing kinetics and thixotropic properties of epoxy resin composites with different kinds of fillers, Journal of Materials Research and Technology 18 (2022) 2125-2139. https://doi.org/10.1016/j.jmrt.2022.03.102.
[112] Y. Zhao, D. Drummer, Influence of filler content and filler size on the curing kinetics of an epoxy resin, Polymers 11(11) (2019) 1797. https://doi.org/10.3390/polym11111797.

[113] S.Q. Arlington, S.C. Barron, J.B. DeLisio, J.C. Rodriguez, S. Vummidi Lakshman, T.P. Weihs, G.M. Fritz, Multifunctional reactive nanocomposites via direct ink writing, Advanced Materials Technologies 6(5) (2021) 2001115. https://doi.org/10.1002/admt.202001115.
[114] O. Uitz, P. Koirala, M. Tehrani, C.C. Seepersad, Fast, low-energy additive manufacturing of isotropic parts via reactive extrusion, Addit. Manuf. 41 (2021) 101919. https://doi.org/10.1016/j.addma.2021.101919.
[115] O. Rios, W. Carter, B. Post, P. Lloyd, D. Fenn, C. Kutchko, R. Rock, K. Olson, B. Compton, 3D printing via ambient reactive extrusion, Mater. Today Commun. 15 (2018) 333-336. https://doi.org/10.1016/j.mtcomm.2018.02.031.
[116] Q. Chen, T. Sukmanee, L. Rong, M. Yang, J. Ren, S. Ekgasit, R. Advincula, A dual approach in direct ink writing of thermally cured shape memory rubber toughened epoxy, Acs Applied Polymer Materials 2(12) (2020) 5492-5500. https://doi.org/10.1021/acsapm.0c00839.
[117] S. Li, Z. Lu, H. Zhang, Z. Ai, Y. Ran, Y. Li, X. Deng, D. Li, Rheological behavior of multi-sized SiC inks containing polyelectrolyte complexes specifically for direct ink writing, J. Eur. Ceram. Soc. (2022). https://doi.org/10.1016/j.jeurceramsoc.2022.04.048.
[118] B. Nematollahi, M. Xia, J. Sanjayan, Current progress of 3D concrete printing technologies, ISARC. Proceedings of the international symposium on automation and robotics in construction, IAARC Publications, 2017.
[119] A.M. Mostafa, A. Yahia, New approach to assess build-up of cement-based suspensions, Cem. Concr. Res. 85 (2016) 174-182. https://doi.org/10.1016/j.cemconres.2016.03.005.
[120] N. Roussel, Rheological requirements for printable concretes, Cem. Concr. Res. 112 (2018) 76-85. https://doi.org/10.1016/j.cemconres.2018.04.005.
[121] B. Panda, C. Unluer, M.J. Tan, Investigation of the rheology and strength of geopolymer mixtures for extrusion-based 3D printing, Cem. Concr. Compos. 94 (2018) 307-314. https://doi.org/10.1016/j.cemconcomp.2018.10.002.
[122] D. Jiao, R. De Schryver, C. Shi, G. De Schutter, Thixotropic structural build-up of cement-based materials: A state-of-the-art review, Cem. Concr. Compos. 122 (2021) 104152. https://doi.org/10.1016/j.cemconcomp.2021.104152.
[123] A. Shahzad, I. Lazoglu, Direct ink writing (DIW) of structural and functional ceramics: recent achievements and future challenges, Composites, Part B 225 (2021) 109249. https://doi.org/10.1016/j.compositesb.2021.109249.
[124] J.W. Kopatz, J. Unangst, A.W. Cook, L.N. Appelhans, Compositional effects on cure kinetics, mechanical properties and printability of dual-cure epoxy/acrylate resins for DIW additive manufacturing, Addit. Manuf. 46 (2021) 102159. https://doi.org/10.1016/j.addma.2021.102159.
[125] A. De Marzi, G. Giometti, J. Erler, P. Colombo, G. Franchin, Hybrid additive manufacturing for the fabrication of freeform transparent silica glass components, Addit. Manuf. 54 (2022) 102727. https://doi.org/10.1016/j.addma.2022.102727.

Chapter 3

Characterization Methods to Predict Extrusion Performance in Thermoplastic Polyurethane Batches

3. Characterization Methods to Predict Extrusion Performance in Thermoplastic Polyurethane Batches

John P. Reynolds+[a,b], James Brown+[c,d], Arit Das[a,b], Patrick Willoughby[f], Joseph Delaney[f], Tatyana Dyndikova[f], Timothy E. Long[c,d,e], Michael J. Bortner[*a,b]

[a]Department of Chemical Engineering, Virginia Tech, Blacksburg, VA 24061

[b]Macromolecules Innovation Institute, Virginia Tech, Blacksburg, VA 24061

[c]Chemisty, School of Molecular Sciences, Arizona State University, Tempe, AZ 85281

[d]Biodesign Center for Sustainable Macromolecular Materials and Manufacturing, Arizona State University, Tempe, AZ 85281

[e]Chemical Engineering, School for Engineering of Matter, Transport and Energy, Arizona State University, Tempe, AZ 85281

[f]Boston Scientific, St. Paul, MN, 55113

+Co-first authors

*Corresponding author

| mbortner@vt.edu | 245 Goodwin Hall, 635 Prices Fork Rd, Blacksburg, VA 24061

This chapter is presented as a portion of a research article currently in preparation for submission to the *Polymer Degradation and Stability* Journal.

3.1 Abstract

Thermoplastic polyurethanes (TPUs) are a class of urethane elastomers which flow at elevated temperatures, enabling a diverse set of processing techniques including industrial-scale extrusion and injection molding. Due to variations in the relative content of hard and soft segments within the polymer chains, as well as block lengths and chemistries, this material exhibits a wide range of viscoelastic properties depending on the synthetic process and thermal history. Numerous manufacturers produce their own proprietary brands of TPU, thus creating a diverse market for a product whose processability varies depending on the supplier. Lot dependent undesirable characteristics may be observed during melt extrusion, including degradation at process-relevant temperatures, increases in viscosity over time, and buildup of solid-like particulates during extrusion. This manuscript implements a combination of chemorheological, spectroscopic, solubility, light scattering, and calorimetric techniques to understand the formation of this solid particulate phase during extrusion. The presence of endothermic transitions, large degrees of branching, rapidly changing viscoelastic properties, and poor dissolution capabilities were correlated with the worst performing lots of TPU in terms of extrudability. These findings suggest that solidification is caused by physical crosslinking through hard phase aggregation, which is attributed to differences in polymer branching architecture, high chain mobility, and strain under extrusion conditions. The strong association between polymer branching and solidification during extrusion highlights the ability for these characterization techniques to rapidly screen for extrusion-related performance of TPUs prior to processing.

3.2 Introduction

Thermoplastic polyurethanes (TPU) are a class of randomly coupled, linear, multiblock copolymers with alternating hard and soft segments [1]. The synthetic pathways available to

produce TPUs are vast, but typically a polyol and a diisocyanate are combined which causes step growth polymerization; depending on the functionality of the polyol (i.e. the relative amount of chemically reactive sites), crosslinks can form resulting in the formation of a thermosetting polymer [2].

The reactivity and cure profile of polyurethanes is dominated by the choice of diisocyanate, largely because the molecular weight of the respective polyol is significantly higher than the diisocyanate [3]. Thus, the chemical structure of the diisocyanate drives reactivity in two major ways. First, electron withdrawing effects due to aromaticity – which stabilizes the transition state – cause much more rapid molecular weight growth compared to aliphatic diisocyanates [4]. Second, the symmetry of the isocyanate (NCO) functional groups on each molecule can cause differences in cure progression. Symmetric NCO groups induce single-stage molecular weight growth, whereas asymmetric NCO groups result in a distinct two-stage molecular weight buildup [5]. Precursors including toluene diisocyanate (aromatic and asymmetric) therefore react relatively faster and in two stages, whereas hexamethylene diisocyanate (aliphatic and symmetric) reacts slower and in one stage [5]. Thus, the choice of chemical precursor, as well the ratio of NCO groups relative to hydroxyl (OH) groups, will have profound effects on the relative amount of hard and soft segments present within the fully synthesized TPU [6].

These hard segments, which provide strength and overall structural/mechanical properties, are primarily comprised of chain extenders (in the form of short-chain diols) and reacted diisocyanates. In contrast, the soft segments (typically flexible polyesters and polyesters) enable chain mobility which increases the elasticity of the sample [1, 7]. The linear nature of TPU, in contrast to the crosslinked thermosetting variety, facilitates thermoplasticity [8].

Thermoplasticity specifically facilitates melt-flow material extrusion of TPU using a variety of techniques, including but not limited to selective laser sintering additive manufacturing (AM), fused filament fabrication AM, large-scale injection molding, and twin-screw extrusion processing [9-12]. However, processing TPU at the temperatures necessary for melt-flow (often > 200 °C) is challenging given the similarities between its thermal degradation temperature and processing temperature [13].

The similarity between the degradation and processing temperatures of TPU complicates the material extrusion process. Oftentimes, their proximity leads to an unwanted buildup of an unknown, solid, white particulate substance, as shown by the candle filters used during extrusion in Figure 3.1. This buildup is time-dependent, such that extrusion operates normally for some finite amount of time, but eventually particulate buildup initiates, which causes the extrudate to solidify. For many batches of TPU, this problem worsens to the point that a complete blockage occurs within the extruder.

This stiffening behavior is hypothesized to occur via a combination of side reactions and hard segment agglomeration. As such, it is possible to utilize chemorheology – where changes in viscoelasticity are monitored at process-relevant time scales using a torsional rheometer –to probe for changes in physical/chemical crosslinking [14]. This methodology has been widely accepted when tracking chemical reaction kinetics and physical crosslinking processes for time periods ranging from several hours to multiple days [5, 15, 16].

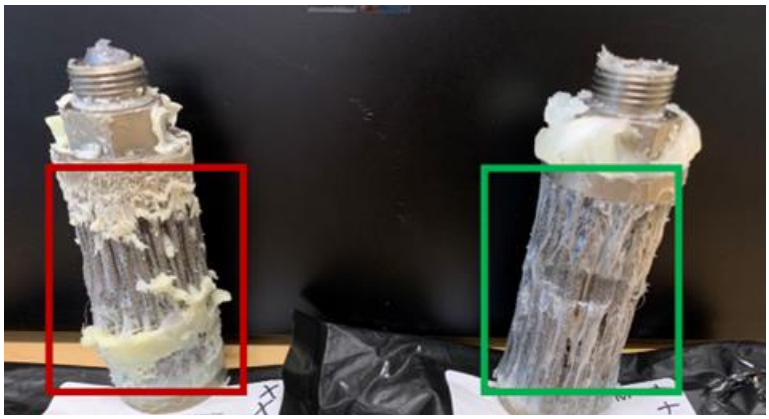

Figure 3.1: (Left) Solid white material building up on candle filters during extrusion and (Right) a candle filter without any particulate buildup, indicative of proper performance.

While chemorheological results elucidate the evolution of mechanical/viscoelastic properties over time, changes in morphology and chemical structure are not necessarily captured using this method. As such, complimentary chemical analyses are necessary to determine whether chemical (i.e. covalent) or physical (i.e. hard/soft segment agglomeration) crosslinking is the cause of solidification. In this work, a series of Shore 55D poly(tetramethylene oxide)-butane diol-methylene diphenyl diisocyanate (PTMO-BDO-MDI) TPU samples from three separate manufacturers are investigated, such that their viscoelastic characteristics are correlated against their extrusion performance. Although the intended product in the reaction between MDI and the respective polyol is a linear polyurethane with only urethane linkages throughout the polymer backbone, it is well documented that side reactions can occur both in dry and humid conditions [17-19]. Scheme 3.1 highlights the most prominent side products, and their respective reaction pathways, that form under these conditions during (PTMO-BDO-MDI) polyurethane synthesis.

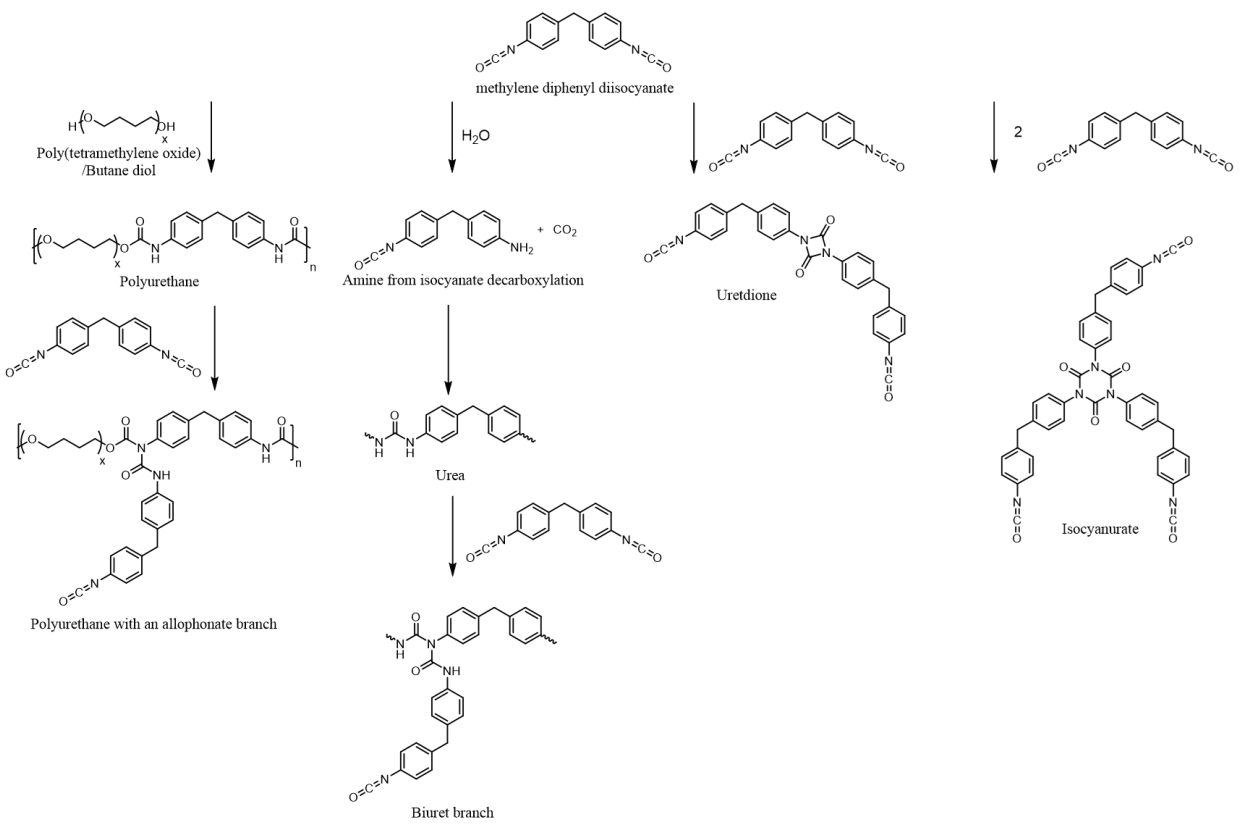

Scheme 3.1: Chemical structures and reaction mechanisms of common side products during production of MDI-based polyurethanes.

Allophanate branching occurs when the most nucleophilic nitrogen in the polyurethane precursor reacts with a free isocyanate. Approximately 10% of these nitrogens react to form a branching points, which heavily depends on reaction conditions [20]. In humid conditions, moisture can also cause this isocyanate to decarboxylate, which forms an amine as well as carbon dioxide via a carbamic acid intermediate [21]. This amine can further react with isocyanates resulting in a urea bond; higher moisture conditions increase the frequency of urea bond formation [22]. Furthermore, nucleophilic nitrogens in this urea bond form biuret branches along the polymer chain when reacting with free isocyanate groups [23]. Isocyanates may also react with one another through dimerization and trimerization to form either uretdione or isocyanurate groups, respectively. This process is far less prevalent than allophanate and biuret formation, especially

since their formation is catalyst-dependent [24]. Evidently, small changes in reaction conditions including temperature, moisture content, catalysis, and reaction timeframe have profound effects on the final architecture of the polymer, especially due to the presence of branch points and potential covalent crosslinks. By studying these phenomena in the context of large-scale extrusion processing, there is potential to greatly modify the processability of TPUs based on the formation of these unintended side products [18,20,23].

This research studies the undesired buildup of solid particulate matter during melt extrusion of TPU, which is potentially attributed to a combination of side reactions and morphological rearrangement of hard and soft segments during high temperature processing. Here, rapid rheological protocols are introduced which can quickly predict the performance of TPU batches off-line, such that a total shutdown of the extrusion line is avoidable and predictable using limited sample quantities. Supporting solubility, spectroscopic, light scattering, and calorimetric techniques are discussed in brevity to provide evidence that hard segment aggregation is a driving factor for extrusion performance. This discussion provides evidence that bulk physical (as opposed to covalent) rearrangement of hard and soft segments largely drives the buildup of solid particulate matter. Multiple lots of TPU from three different manufacturers (A, B, and C) are analyzed. The performance of these TPU batches covers a range of outcomes, varying from “no issues at all” to a “complete shutdown of the extrusion line.” To the authors’ knowledge, no studies have merged the aforementioned characterization techniques with a fundamental understanding of thermal stability and molecular architecture using bulk material measurements of manufacturer- and lot-dependent TPUs. In this study, a unique rheological protocol is developed which identifies the mostly likely cause of an unwanted accumulation of solid matter during melt extrusion of TPU.

These rapid screening protocols can be employed by any researcher or engineer to quickly predict extrusion success of TPU lots in an off-line manner.

3.3 Materials and Methods

Multiple lots of Shore 55D (PTMO-BDO-MDI) TPU from three separate manufacturers were studied. The thermal stability, spectroscopic properties, solubility, and rheological properties of these materials ideally remain consistent when comparing different batches of TPU; however, there are clear differences in these properties lot-by-lot, which provides evidence of varying extrusion success. Changes in molecular structure during processing, the presence of branching, and differences in overall polymer architecture are primarily hypothesized to impact extrusion.

Because the TPU samples vary in extrusion capability lot-by-lot, each sample is designated here by its respective manufacturer name first, and then the lot number. For example, sample B2 refers to manufacturer B, lot 2. Manufacturer A provided three lots of material. Sample A1 performed well during extrusion with no signs of solid particulate buildup, although A2 had slightly inferior extrusion performance with some particulates observed during extrusion over long runs. A3 performed the worst with significantly higher particulate content collected at the filter. Overall, however, TPU from manufacturer A extruded “acceptably” and generally did not experience any significant signs of solidification (e.g. sufficient to shut down the extrusion line) or differences between lots. The right side of Figure 3.1 visualizes these findings, such that no particulate buildup is observed. Manufacturer B produced two lots of TPU. The extrusion performance of TPU from manufacturer B was described as “intermediate,” and frequently experienced solid particulate formation during extrusion that impacted the extrusion line. B1 performed the best, and B2 performed worse, with both exhibiting significant accumulation of solid particulate at the filter at a higher rate than the manufacturer A samples, but not sufficient to

shut down the extrusion line. Therefore, this manufacturer extrusion performance was designated as "impacted." Manufacturer C also provided three lots of samples, and these all portrayed significantly impacted extrusion capabilities with significant solid-like buildup, stopping the extrusion line. Of these, C1 had the best extrusion performance, C2 was worse, and C3 had very poor extrusion outcomes. As a whole, however, TPU from manufacturer C consistently caused the extrusion line to completely stop. A summary of these materials is provided in Table 3.1.

Table 3.1: TPU batch extrusion performance for a given manufacturer and respective lot number.

Manufacturer	Relative Lot Extrusion Performance			Manufacturer Extrusion Performance
	1	2	3	
A	Best	Intermediate	Worst	Acceptable
B	Best	Worst	-------	Impacted
C	Best	Intermediate	Worst	Line Stopped

All solvents for chemical/spectroscopic analyses were purchased from Fisher Scientific and used as received. Lithium bromide (LiBr) was purchased from Sigma Aldrich and dried at 120 °C prior to use.

TPU pellets were dried in a vacuum oven at 80 °C for three days prior to characterization, which ensured moisture was removed. FT-IR data was collected on a Nicolet iS10 spectrometer equipped with an ATR stage, and the data was averaged over 64 scans. Differential scanning calorimetry (DSC) was used to investigate any thermal transitions present within the polyurethane lots. Approximately 7 mg of each TPU sample as received (i.e. pellets) from the manufacturer was placed in an aluminum T-Zero pan using a hermetically sealed lid. A TA Instruments DSC 2500 running under a constant nitrogen flow (50 ml min^{-1}) was used for these experiments. An empty T-Zero pan with a hermetically sealed lid was used for reference. All DSC experiments were

conducted at a heating/cooling rate of 10 °C min^{-1}. Endotherms are indicated in the positive direction. Because the urethane bond becomes unstable at temperatures exceeding 220 °C, second heat experiments were stopped at this temperature. While modulated DSC (MDSC) experiments would have yielded marginally better insight into the kinetics of structural change during the degradation process, the goal was to develop a simple and effective screening method to predict processability. Therefore, to increase accessibility for future researchers, linear non-isothermal DSC temperature ramps were utilized.

Pellets were dissolved in DMSO for ^{1}H NMR tests. ^{1}H NMR spectra were recorded using a Bruker Avance NEO 500 MHz NMR equipped with a 5mm iProbe. Data was averaged from 256 scans with a 5 s relaxation time. Prior to dynamic light scattering (DLS) experiments, a solubility study probed the strong intermolecular forces holding the TPU samples together. The TPU pellets were tested both as received from the manufacturers in pellet form and after melt pressing at 205 °C for 5 min at 5000 PSI. Approximately 15 mg of TPU was submerged in 3 mL of either tetrahydrofuran (THF), dimethyl formamide (DMF), or a 0.05 M LiBr solution in DMF (DMF+LiBr). After being submersed overnight in solvent, visual inspection and DLS were used to identify solubility success.

For rheology tests, the samples were initially pressed into 1 mm thick, 25 mm diameter discs at 220 °C and 5000 PSI for five minutes. The pressure was released to eliminate any air bubbles, and five more minutes of compression was performed. However, when the disc was placed into the rheometer at 190 °C, the material degraded after five minutes. To ensure that this was not an artifact of the rheometer causing degradation, the melt-pressed samples were placed into an oven at 190 °C for 30 minutes; once again, all samples degraded. An example of this for TPU from manufacturer B is presented in Figure 3.2.

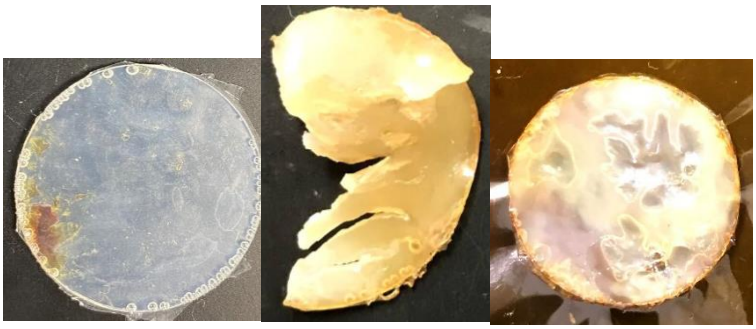

Figure 3.2: (Left) Pellets of TPU from manufacturer B pressed at 220 °C for 5 minutes, (Middle) melt pressed sample after being left in a rheometer at 190 °C for 5 minutes, (Right) melt pressed sample after being left in an oven at 190 °C for 30 minutes.

Thus, pellets of TPU had to be loaded directly into the rheometer, allowed to transition into their flow state, and then brought to the appropriate gap height. All rheological tests were performed using 25 mm stainless steel parallel plates with a 1 mm gap on a Discovery HR-30 rheometer (TA Instruments, Newcastle, DE, USA). Temperature ramps were performed from 190-230 °C at 1 °C/min. Time sweeps were conducted for 20 minutes at 200 °C. All measurements were taken in oscillatory mode at a frequency of 1 Hz and a strain of 0.5% which was within the linear viscoelastic region.

3.4 Results and Discussion

An initial discussion in this section provides evidence that physical crosslinking likely dominates the formation of solid particulate buildup. Those details are discussed in brief in order to limit overlap with the dissertation of James Brown. For further information, please consult his dissertation entitled “Structure-Processing-Property Relationships in Molecular Assembly Across Length Scales: From Semicrystalline Polymers to Small Molecule Surfactants.” The results in section 3.4.2 are my unique contributions.

3.4.1 Evidence of Physical Crosslinking

Four lots of TPU (A1, B1, B2, C3) were subjected to a series of chemical characterization methods. These lots were chosen because they capture a wide range of extrusion performances ("acceptable," "impacted," and "line stopped"). Spectroscopic techniques were initially used to probe for differences in chemical structure with the goal to correlate findings with potential differences in extrusion processing. ^{1}H NMR confirmed that the structure of every TPU batch took the form of a PTMO-BDO-MDI polyurethane, which was consistent with literature [25]. FTIR and ^{1}H NMR spectra are provided in Figure S9.1.1 of the supporting information and suggest that 1) no quantifiable differences in chemical structure can be established based off spectroscopy alone and 2) the ratio of the chemical shift peaks at 1.70 and 1.47 ppm indicate 60% hard segments and 40% soft segments, respectively.

DSC analysis provided in Figure S9.1.2 illustrates heat-isotherm-cool-heat experiments of TPU pellets as received from the manufacturer. Although lots A1 and B1 display no early onset isotherm, lots B2 and C3 display endothermic peaks at approximately 170-180 °C – attributed to MDI-BDO-MDI sequence agglomeration [26]. Larger endotherms suggest a greater presence of these agglomerates/stable phases. During the second heat, two peaks are present. The first peak between 170 °C and 207 °C failed to correlate with processability, but the second endothermic event beginning at 208 °C correlated directly with poor processability, suggesting that larger endotherms contribute towards thermal transitions which negatively impact extrusion performance. [26].

Solubility studies were also performed to probe for the presence of physical (as opposed to covalent) crosslinking. Three solvents of increasing strength (THF, DMF, and DMF+LiBr) were used to identify the degree to which solubility was possible. When dissolved in THF or DMF, solubility was not possible for any of the as received pellets. However, upon melt pressing, every

TPU was dissolvable in both of these solvents except C3. This finding suggests that either chemical or physical crosslinking prevented dissolution prior to heat treatment for the worst performing lot of TPU. The addition of LiBr to the DMF facilitated dissolution of all lots – both as received in pellet form and after melt pressing. This strongly polar solvent solution effectively screened for the presence of strong intermolecular interactions within the polyurethane, which enabled dissolution and validated the prominence of physical (as opposed to covalent) crosslinking in the form of hard segment aggregation after heat treatment [27]. This finding also confirmed that the as received pellets were not covalently crosslinked to any meaningful extent. The inability of melt pressed samples from the C3 lot to dissolve in just DMF suggests that these stable, intermolecularly concentrated phases were increasingly present in C3 post-melt pressing.

Subsequent DLS experiments (see Figure S9.1.3) established the presence of similarly sized TPU chains post-melt pressing, but worse performing lots contained TPU chains with smaller hydrodynamic radii prior to heat treatment. It is well documented that these smaller hydrodynamic radii can be attributed to branched architectures (e.g. biuret and allophanate branching), and that worse performing lots possess these branches to a greater extent due to side reactions during the upstream supplier synthetic process, thus predisposing them to poor processability and aggregation [22, 28]. During this segment rearrangement, lots B2 and C3 established stable intermolecular interactions in the polyurethane which negatively impacted extrusion performance. The impact of these microstructural rearrangements on process-relevant viscoelastic properties is subsequently discussed, although the exact mechanism of this phenomenon is unclear and serves as a potential research topic in future work.

3.4.2 Rheological Analysis

The viscoelastic properties most relevant to degradation processes are outlined in Equations (S9.1.1)-(S9.1.6) in the supplementary information. To probe for changes in viscoelasticity over a range of temperatures, temperature ramps were conducted from 190-230 °C at a rate of 1 °C min^{-1}. Because this range covered typical TPU processing temperatures, it was hypothesized that this test would reveal a region where solidification began. Thermal degradation of the urethane bond in TPU has been confirmed to occur within this temperature range, which directly impacts rheological properties in the melt flow state [22]. The results of these temperature ramps are illustrated in Figure 3.3 for manufacturer A, which indicates that the complex viscosity decreases, and the loss tangent rises with temperature. This is expected since thermoplastic materials become more fluidic with elevated temperatures. However, there is no evidence of solidification between the processing temperature (~200-205 °C) and the degradation temperature (>220 °C).

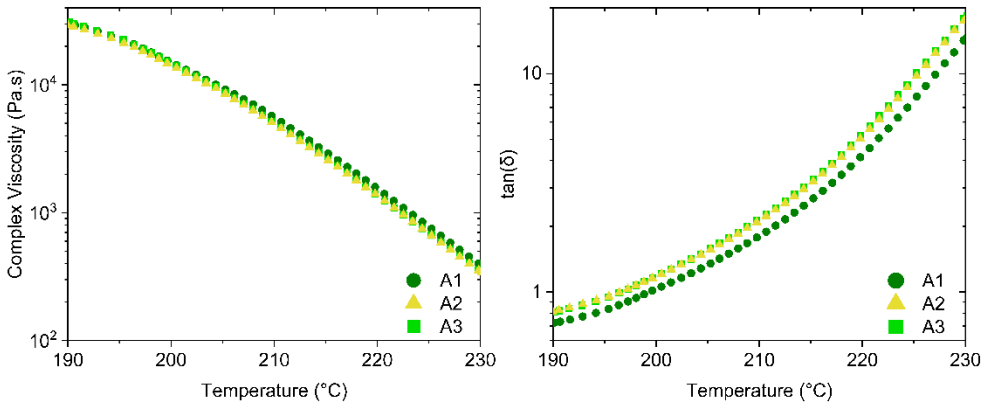

Figure 3.3: (Left) Temperature dependence of complex viscosity and (Right) loss tangent during temperature ramps of TPU from manufacturer A.

Thus, there are likely time-dependent factors which are not sufficiently captured within the timescale of this temperature ramp. It is also plausible that larger pressures associated with melt extrusion processing accelerate the solidification process, which explains why melt pressed samples degrade so rapidly compared to pellets that are directly loaded onto the rheometer plate.

To account for this behavior, time sweeps at 200 °C were performed for 20 minutes as illustrated in Figure 3.4.

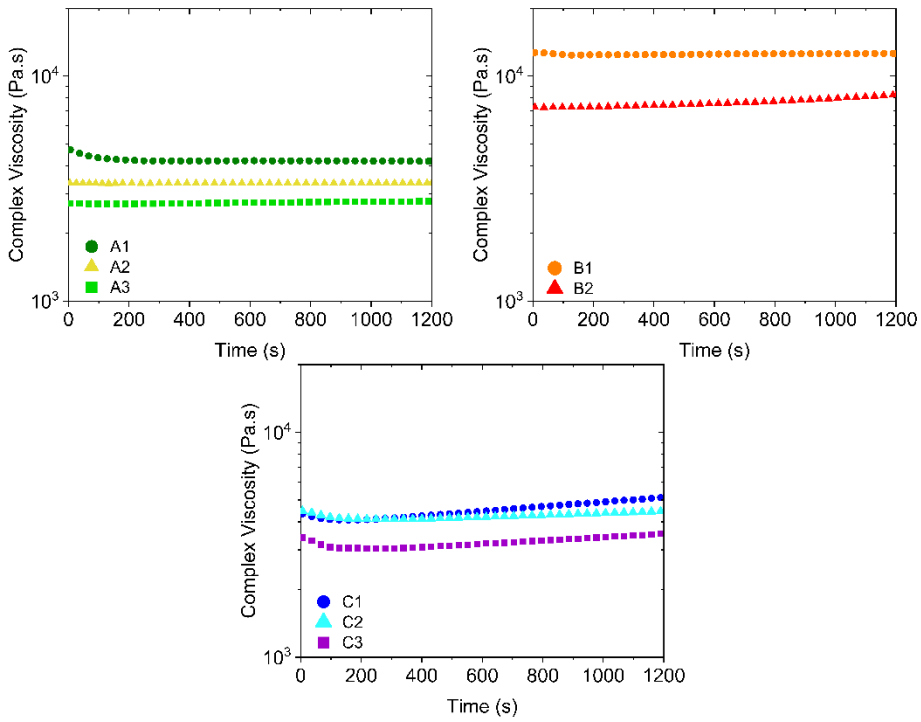

Figure 3.4: Isothermal time sweeps at 200 °C tracking the complex viscosity for each lot of TPU from (Top Left) manufacturer A, (Top Right) manufacturer B, and (Bottom) manufacturer C.

Figure 3.4 highlights that TPU from manufacturer A (overall "acceptable" extrudability) does not exhibit time-dependent changes in complex viscosity. In contrast, TPU from manufacturer B exhibits time-dependent increases complex viscosity readings; TPU B2 specifically becomes more viscous over time. This finding aligns with Table 3.1, which suggests that B2 has poorer extrusion capabilities than B1. Finally, the complex viscosity plot for manufacturer C indicates that all lots of TPU (C1, C2, and C3) become more viscous with time. Once again, these viscosity profiles corroborate with Table 3.1, which suggests that TPU from manufacturer C stopped the extrusion line, with a large potential for solid-like formation. For every

given manufacturer, the worst performing TPU lot possesses the lowest viscosity. Previous studies have suggested that for polymers of equal molecular weight, branched polymers exhibit lower viscosities compared to linear polymers; it is hypothesized here that the lowest viscosity TPUs from each manufacturer are more branched, which contributes towards solidification [29-31]. To further evaluate the solidification process of these TPUs, the loss tangent was analyzed across this 20-minute timeframe. The results of this analysis are presented in Figure 3.5.

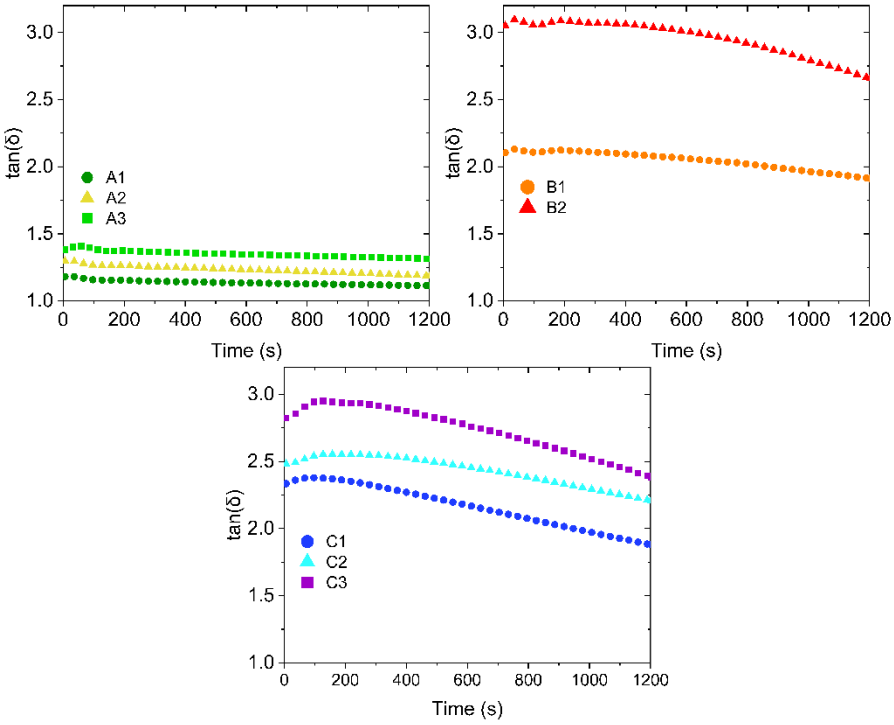

Figure 3.5: Isothermal time sweeps at 200 °C tracking the loss tangent for each lot of TPU from (Top Left) manufacturer A, (Top Right) manufacturer B, and (Bottom) manufacturer C.

While the loss tangent varies widely between companies and lots, all samples show relatively fluidic behavior (tan(δ) > 1) which suggests that extrusion should be feasible. However, some samples approach a loss tangent of 1 more rapidly than others, where a loss tangent below 1

suggests solid-like behavior. To quantify this finding, the rate of change for the loss tangent $\frac{dtan(\delta)}{dt}$ was calculated using the last 10 minutes of data (when viscoelastic properties changed linearly with time, and temperature fluctuations became negligible). These findings are presented in Table 3.2.

Table 3.2: The rate of change of the loss tangent for each lot of TPU.

Manufacturer	$\frac{dtan(\delta)}{dt}$ of each lot [s^{-1}]		
	1	2	3
A	-3.7×10^{-5}	-8.6×10^{-5}	-6.1×10^{-5}
B	-2.5×10^{-4}	-5.9×10^{-4}	----------
C	-4.2×10^{-4}	-4.9×10^{-4}	-6.4×10^{-4}

When making comparisons across companies, TPU from manufacturer A appears to be the most stable material for extrusion. It experiences relatively low rates of change of tan(δ) – on the order of 10^{-5} s^{-1}. By contrast, $\frac{dtan(\delta)}{dt}$ for manufacturer B increases by an order of magnitude compared to manufacturer A. This increased rate reflects the worsening extrusion capabilities of manufacturer B's TPU, as well as the solidification process which occurs within the extruder. Similarly, $\frac{dtan(\delta)}{dt}$ for TPU from manufacturer C is on the same order of magnitude as TPU from manufacturer B, which reflects both of their poor extrusion capabilities. C3 has the most rapid rate of solidification, aligning with extrusion performance findings.

When making intra-lot comparisons, Table 3.2 suggests that the rate of solidification does not change meaningfully between lots for manufacturer A. This comparison aligns with findings from Table 3.1 which highlights that TPU A extrudes acceptably overall, with no noticeable differences in extrusion performance. For manufacturer B, the rate of solidification increases from B1 to B2, which aligns with the complex viscosity profiles in Figure 3.4. and the relative extrusion capabilities listed in Table 3.1 (B1 is "best" while B2 is "worst"). Similarly for manufacturer C,

the TPU with the "best" extrusion capabilities (C1, according to Table 3.1) exhibits the lowest rate of solidification, while the worst extruding material from manufacturer C (C3, according to Table 3.1) experiences the highest rate of solidification. Thus, these rheological findings accurately reflect extrusion performance when comparing individual lots of TPU from a given manufacturer (e.g., C1 performs better than C3), and also when comparing TPU between companies (e.g., manufacturer A performs better than manufacturer C). The preceding discussions on solubility, calorimetry, and spectroscopy further substantiate these findings and suggest that this approach adequately probes into the mechanistic details causing variations in extrusion success.

3.5 Conclusion

The relative proximity of the processing and degradation temperatures of TPU complicates melt extrusion due to the presence of undesirable side reactions and morphological rearrangements, which collectively produce solid particulate buildup in the extrusion line. Through this research, we have shown that the degree to which this aggregation occurs is batch-dependent; in fact, the presence of these hard segment aggregates is not only manufacturer-dependent, but also lot-dependent. While spectroscopic techniques could not establish quantifiable differences between samples in terms of chemical composition, calorimetric methods identified endothermic transitions consistent with the presence of stable phases which negatively impact extrusion performance. These high temperature endotherms correlated directly with poor processability (i.e. manufacturer A possessed smaller endotherms than manufacturer C). Based on the solubility studies, these stable phases resulted from hard segment aggregation – due to biuret and allophanate branch formation during the synthetic process – which could be effectively broken through strong polar solvents, thus validating the presence of physical crosslinking as opposed to covalent crosslinking. The worst performing lot of TPU required the strongest and most polar solvent to

dissolve, suggesting that a larger presence of these stable phases contributes towards extrusion line shutdown. DLS confirmed that smaller hydrodynamic radii, which directly correlate with worse performing lots, predisposed the TPU to more branched architectures during synthesis, specifically attributed to the aforementioned biuret and allophanate side reactions.

A simple rheological screening method to predict the extrusion performance of TPU off-line was also introduced, which rapidly screened for solidification while using minimal sample quantities. This process involved a 20-minute time sweep (representative of a typical extruder residence time) at process-relevant temperatures using small amplitude oscillatory shear. A qualitative view of complex viscosity profiles, as well as the rate at which tan(δ) approached 1, provided the best evidence of solidification. The viscoelastic properties of manufacturer A were essentially time-independent at process-relevant temperatures, which aligned with its acceptable extrusion performance. However, manufacturers B and C saw changes in viscoelasticity over time (e.g. tan(δ) decreasing and η* increasing) which provided confirmation of solid-like buildup. The timescales associated with the solidification process were more rapid for manufacturer C than manufacturer B, which agreed with manufacturer extrusion performance, as well as calorimetric and solubility studies. The fact that the lowest viscosity materials possessed the worst extrusion performance confirmed the presence of branched architectures prior to processing, which predisposed these materials to further aggregation. Thus, by performing a simple oscillatory experiment in a torsional rheometer, it is possible to predict whether extrusion line shutdown will occur, and this technique is able to distinguish between TPUs from different manufacturers, as well as different lots of TPU from the same manufacturer. We have therefore demonstrated that this hard segment aggregation can be probed using a variety of characterization methods, and from

an economic perspective, the novel rheological analysis presented here can save significant amounts of resources while limiting process downtime.

3.6 References

[1] D. Nichetti, S. Cossar, N. Grizzuti, Effects of molecular weight and chemical structure on phase transition of thermoplastic polyurethanes, J. Rheol. 49(6) (2005) 1361-1376. https://doi.org/10.1122/1.2071987.
[2] A. Kumar, R.K. Gupta, Fundamentals of Polymers, McGraw-Hill 1998.
[3] J. Guo, T. Chai, Y. Liu, J. Cui, H. Ma, S. Jing, L. Zhong, S. Qin, G. Wang, X. Ren, Kinetic research on the curing reaction of hydroxyl-terminated polybutadiene based polyurethane binder system via FT-IR measurements, Coatings 8(5) (2018) 175. https://doi.org/10.3390/coatings8050175.
[4] C. Korah Bina, K. Kannan, K. Ninan, DSC study on the effect of isocyanates and catalysts on the HTPB cure reaction, J. Therm. Anal. Calorim. 78(3) (2004) 753-760. https://doi.org/10.1007/s10973-005-0442-0.
[5] V. Sekkar, S. Venkatachalam, K.N. Ninan, Rheokinetic studies on the formation of urethane networks based on hydroxyl terminated polybutadiene, Eur. Polym. J. 38(1) (2002) 169-178. https://doi.org/10.1016/S0014-3057(01)00106-9.
[6] M.A. Pérez-Limiñana, F. Arán-Aís, A.M. Torró-Palau, C. Orgilés-Barcel, J.M. Martín-Martínez, Influence of the hard-to-soft segment ratio on the adhesion of water-borne polyurethane adhesive, J. Adhes. Sci. Technol. 21(8) (2007) 755-773. https://doi.org/10.1163/156856107781362635.
[7] J. Silva, D. Meltzer, J. Liu, M. Cox, J. Maia, The influence of thermo-mechanical history on structure development of elastomeric and amorphous glass thermoplastic polyurethanes, Polymer Engineering & Science 54(6) (2014) 1383-1393. https://doi.org/10.1002/pen.23673.
[8] A. Frick, A. Rochman, Characterization of TPU-elastomers by thermal analysis (DSC), Polym. Test. 23(4) (2004) 413-417. https://doi.org/10.1016/j.polymertesting.2003.09.013.
[9] G. Kim, E. Barocio, R.B. Pipes, R. Sterkenburg, 3D printed thermoplastic polyurethane bladder for manufacturing of fiber reinforced composites, Addit. Manuf. 29 (2019) 100809. https://doi.org/10.1016/j.addma.2019.100809.
[10] T. Xu, W. Shen, X. Lin, Y.M. Xie, Mechanical properties of additively manufactured thermoplastic polyurethane (TPU) material affected by various processing parameters, Polymers 12(12) (2020) 3010. https://doi.org/10.3390/polym12123010.
[11] X. Lin, P. Coates, M. Hebda, R. Wang, Y. Lu, L. Zhang, Experimental analysis of the tensile property of FFF-printed elastomers, Polym. Test. 90 (2020) 106687. https://doi.org/10.1016/j.polymertesting.2020.106687.
[12] H.Y. Mi, X. Jing, M.R. Salick, W.C. Crone, X.F. Peng, L.S. Turng, Approach to fabricating thermoplastic polyurethane blends and foams with tunable properties by twin-screw extrusion and microcellular injection molding, Adv. Polym. Tech. 33(1) (2014). https://doi.org/10.1002/adv.21380.
[13] G. Lu, D.M. Kalyon, I. Yilgör, E. Yilgör, Rheology and extrusion of medical-grade thermoplastic polyurethane, Polymer Engineering & Science 43(12) (2003) 1863-1877. https://doi.org/10.1002/pen.10158.

[14] M.J. Bortner, V. Bhanu, J.E. McGrath, D.G. Baird, Shear rheological properties of acrylic copolymers and terpolymers suitable for potentially melt processable carbon fiber precursors, J. Appl. Polym. Sci. 93(6) (2004) 2856-2865. https://doi.org/10.1002/app.20833.
[15] B. Lucio, J.L. de la Fuente, Kinetic and chemorheological modelling of the polymerization of 2, 4-Toluenediisocyanate and ferrocene-functionalized hydroxyl-terminated polybutadiene, Polymer 140 (2018) 290-303. https://doi.org/10.1016/j.polymer.2018.02.058.
[16] G. Santhosh, S. Reshmi, C.R. Nair, Rheokinetic characterization of polyurethane formation in a highly filled composite solid propellant, J. Therm. Anal. Calorim. 140(1) (2020) 213-223. https://doi.org/10.1007/s10973-019-08793-6.
[17] M. Špírková, M. Kubin, K. Dušek, Side reactions in the formation of polyurethanes: Stability of reaction products of phenyl isocyanate, Journal of Macromolecular Science-Chemistry 27(4) (1990) 509-522. https://doi.org/10.1080/00222339009349572.
[18] M. Špírková, M. Kubin, K. Dušek, Side reactions in the formation of polyurethanes: Model reactions between phenylisocyanate and 1-butanol, Journal of Macromolecular Science—Chemistry 24(10) (1987) 1151-1166. https://doi.org/10.1080/00222338708076935.
[19] E. Sacher, A re-examination of the polyurethane reaction, Journal of Macromolecular Science, Part B: Physics 16(4) (1979) 525-538. https://doi.org/doi.org/10.1080/00222347908215180.
[20] A.M. Heintz, D.J. Duffy, S.L. Hsu, W. Suen, W. Chu, C.W. Paul, Effects of reaction temperature on the formation of polyurethane prepolymer structures, Macromolecules 36(8) (2003) 2695-2704. https://doi.org/10.1021/MA021559H.
[21] Y. Suryawanshi, P. Sanap, V. Wani, Advances in the synthesis of non-isocyanate polyurethanes, Polym. Bull. 76 (2019) 3233-3246. https://doi.org/doi.org/10.1007/S00289-018-2531-7.
[22] E. Delebecq, J.-P. Pascault, B. Boutevin, F. Ganachaud, On the versatility of urethane/urea bonds: reversibility, blocked isocyanate, and non-isocyanate polyurethane, Chem. Rev. 113(1) (2013) 80-118. https://doi.org/10.1021/cr300195n.
[23] K. Dušek, Theory of network formation by additional crosslinking of polyurethanes due to biuret and allophanate formation, Polym. Bull. 17 (1987) 481-488. https://doi.org/10.1007/BF00255622.
[24] J.N. Gibb, J.M. Goodman, The formation of high-purity isocyanurate through proazaphosphatrane-catalysed isocyanate cyclo-trimerisation: computational insights, Organic & Biomolecular Chemistry 11(1) (2013) 90-97. https://doi.org/10.1039/C2OB26547H.
[25] Q. Tang, K. Gao, Structure analysis of polyether-based thermoplastic polyurethane elastomers by FTIR, 1H NMR and 13C NMR, Int. J. Polym. Anal. Charact. 22(7) (2017) 569-574. https://doi.org/10.1080/1023666X.2017.1312754.
[26] D.J. Martin, G.F. Meijs, P.A. Gunatillake, S.P. Yozghatlian, G.M. Renwick, The influence of composition ratio on the morphology of biomedical polyurethanes, J. Appl. Polym. Sci. 71(6) (1999) 937-952. https://doi.org/10.1002/(sici)1097-4628(19990207)71:6<937::aid-app9>3.0.co;2-0.
[27] L. Zeng, X. Lin, P. Li, F.-Q. Liu, H. Guo, W.-H. Li, Recent advances of organogels: From fabrications and functions to applications, Prog. Org. Coat. 159 (2021) 106417. https://doi.org/10.1016/J.PORGCOAT.2021.106417.
[28] J.F. Douglas, J. Roovers, K.F. Freed, Characterization of branching architecture through" universal" ratios of polymer solution properties, Macromolecules 23(18) (1990) 4168-4180. https://doi.org/10.1021/ma00220a022.

[29] M.G. McKee, S. Unal, G.L. Wilkes, T.E. Long, Branched polyesters: recent advances in synthesis and performance, Prog. Polym. Sci. 30(5) (2005) 507-539. https://doi.org/10.1016/j.progpolymsci.2005.01.009.
[30] J.M. Dennis, R.J. Mondschein, J.D. Wolfgang, M. Hegde, R. Odle, T.E. Long, Synthesis and characterization of long-chain branched poly (ether imide) s with A3 comonomers, ACS Applied Polymer Materials 2(2) (2020) 958-965. https://doi.org/10.1021/acsapm.9b01148.
[31] J.D. Wolfgang, K.J. Reynolds, C.B. Arrington, R.R. Odle, S.I. Nazarenko, T.E. Long, Influence of dianhydride regiochemistry on thermomechanical and rheological properties of 3, 3′-and 4, 4′-polyetherimides, Polymer 212 (2021) 123277. https://doi.org/10.1016/j.polymer.2020.123277.

Chapter 4

Chemorheological Kinetic Modeling of Uncatalyzed Hydroxyl-Terminated Polybutadiene and Isophorone Diisocyanate

4. Chemorheological Kinetic Modeling of Uncatalyzed Hydroxyl-Terminated Polybutadiene and Isophorone Diisocyanate

John P. Reynolds[a,b], Tiffany N. Thompson[b,c], Cailean Q. Pritchard[a,b], Michael D. Schulz[b,c], John J. La Scala[d], Michael J. Bortner[a,b,*]

[a]Department of Chemical Engineering, Virginia Tech, Blacksburg, VA 24061

[b]Macromolecules Innovation Institute, Virginia Tech, Blacksburg, VA 24061

[c]Department of Chemistry, Virginia Tech, Blacksburg, VA 24061

[d]U.S. Army Combat Capabilities Development Command's Army Research Laboratory, FCDD-RLW-M, Aberdeen Proving Ground, MD 21005

*Corresponding author | mbortner@vt.edu | 635 Prices Fork Road, Goodwin Hall, Blacksburg, VA, USA

This chapter is presented as a research article currently under review in the *Macromolecular Materials and Engineering* Journal.

4.1 Abstract

Catalysts are often employed to enable non-isothermal reaction kinetic studies when tracking cure progression of polyurethane reactions. However, when quickly reacting, catalyzed materials are prepared through mixing followed by the addition of fillers or additives, subsequent processing of the partially reacted material becomes difficult. Here, chemorheology is used to track changes in viscoelastic properties of uncatalyzed polybutadiene-diisocyanate reactions for multiple days, which quantifies the degree of cure during polymerization. Viscosity profiles are accurately captured by the two-stage Arrhenius model (r^2>0.95), and conversion progress is adequately represented by the Kamal-Sourour model (r^2>0.76). Transition state analysis via Wynne-Jones-Eyring-Evans theory reveals the presence of an associative mechanism according to entropic and enthalpic activation energies $\Delta S^{\#}$ = -96.9 J K^{-1} and $\Delta H^{\#}$ = 36.4 kJ, respectively. These rheokinetic modeling results align with Fourier transform infrared spectroscopy findings. To our knowledge, no rheokinetic studies have tracked cure progress of this uncatalyzed system for the extended timeframe presented here. The cure profile also presents unique viscosity growth, representative of molecular weight buildup, compared to catalyzed systems. This finding emphasizes the novelty of applying previously developed chemorheological models to multi-day thermosetting reactions within a flow field in a manner that is generalizable to many long-term curing systems.

4.2 Introduction

Polyurethanes are a diverse class of materials that can be processed into fibers and foams which find use as heat and sound insulators, flame retardants, and crash protection devices [1]. They also serve as coatings, adhesives, and binder materials, with the ability to sustain large loading levels of solids [2, 3]. A variety of synthesis pathways are available to produce

polyurethanes, most often involving a polyol, such as hydroxyl-terminated polybutadiene (HTPB), and a diisocyanate. The selection of diisocyanate can have a significant influence on the mechanical properties, glass transition temperature, and pot life of the resulting polyurethane [4]. Toluene diisocyanate (TDI), methylene diphenyl diisocyanate (MDI), hexamethylene diisocyanate (HMDI), and isophorone diisocyanate (IPDI) are some of the most frequently encountered reactants. Aromatic diisocyanates, which possess superior electron withdrawing capabilities over their aliphatic counterparts, have been studied more extensively due to the faster reaction time; as such, polyurethanes involving TDI and MDI have been studied to a much further extent than IPDI [4].

With so many avenues to produce polyurethanes, it is imperative that an uncatalyzed, baseline formulation is available with which kinetic data can be compared to quantify the impact of precursor choice and catalysis. By establishing these baseline kinetics, modeling of cure behavior can be performed, which is critical to understanding the time scale available for processing. Mahanta and Pathak provide an overview of the three most common approaches to kinetic parameter determination using non-isothermal differential scanning calorimetry (DSC) methods: the Kissinger method, the Flynn-Wall-Ozawa (FWO) method, and the Kissinger-Akahira-Sunose (KAS) method [5]. The Kissinger method provides the most simplistic approach to determining kinetic parameters by requiring the evaluation of heating rate as a function of peak temperature, though it assumes the reaction is first order leading to a lack of robustness [6]. The FWO method assumes that the temperature integral used in most kinetic models takes an exponential form (Doyle's approximation), allowing the activation energy to be determined as a function of conversion [7]. Similarly, the Coats-Redfern approximation can be used to solve for the temperature integral in the KAS model, which also allows for kinetic parameter determination

at a variety of conversions [5]. In some cases, the KAS model gives better isoconversional estimates of activation energy than the FWO method [7].

While non-isothermal DSC tests can be a powerful tool for determining activation energy, the analysis cannot be conducted within a flow field. Therefore, results might not be representative of manufacturing-relevant processes (e.g. reactive extrusion). Non-isothermal DSC is also constrained based on the thermal ramp rate and upper temperature limit. Thus, a majority of studies to date involve a catalyst to accelerate the relatively sluggish kinetics of (particularly aliphatic) isocyanates, which ensures complete reaction progress. Several catalysts including triphenyl bismuth (TPB), ferric acetyl acid (FeAA), dibutyltin dilaurate (DBTDL), and tin(II) 2-ethylhexanoate (TECH) are commonly employed during non-isothermal DSC experiments [8-12]. Importantly, previous studies have shown that uncatalyzed reactions during these non-isothermal DSC experiments were unable to approach completion within the required timeframe rendering methods such as the FWO analysis inapplicable [10].

Thus, chemorheology becomes an essential tool for tracking viscoelastic parameters and fitting cure profiles to previously developed models for reactions with cure times longer than a few hours (i.e. well beyond the limits of non-isothermal studies). An Arrhenius-based approach to chemorheological modeling can predict the viscosity growth over the course of several hours as a function of temperature-dependent rate and viscosity constants [13]. Lucio and de la Fuente have extended this concept to a two-stage reaction, expressed as two separate Arrhenius equations [14]. Although their work is frequently concerned with (ferrocenylbutyl)dimethylsilane-grafted HTPB, it has provided the groundwork for utilization of the two-stage Arrhenius model as well as the Kamal-Sourour kinetic model. The Kamal-Sourour model analyzes the conversion rate as a

function of conversion, which provides insight on the contribution of the autocatalytic effect towards overall reaction rate [15]. In addition, the Sestak-Berggren equation can describe complex kinetic behavior by relating reaction rate constants to a proposed mechanism [16].

To our knowledge, chemorheological experiments have not been conducted for uncatalyzed HTPB+IPDI at sufficient times scales to capture the changing reaction kinetics over long times (e.g. 90+ hours). Several groups have tracked viscosity profiles for shorter time periods (10 hours or less), but without any insight into viscoelastic properties and their relationship to reaction mechanisms [4, 11, 17, 18]. In fact, some groups have suggested that HTPB+IPDI systems show two-stage viscosity buildup *only* in the presence of a catalyst [19]. Thus, there is a clear opportunity to understand isothermal curing kinetics of a slow-reacting uncatalyzed polyurethane in the presence of a flow field. In this study, we apply a variety of kinetic and transition state models, including the two-stage Arrhenius, Kamal-Sourour, and Wynne-Jones-Eyring-Evans (WJEE) models, to chemorheology measurements measured over long time periods (>90 hours). These findings are compared to temperature-controlled Fourier transform infrared spectroscopy (FTIR) measurements at comparable curing timeframes. Supplemental information is provided regarding the use of the Sestak-Berggren model. The supporting information also contains pertinent findings comparing time-dependent chemorheological and spectroscopic cure profiles. We show that these approaches successfully capture kinetic parameters of a slow reacting diisocyanate and polyol, where the reaction kinetics and long reaction profiles are not well described by current methods and models. Since these reactions are commonly conducted at room temperature over the course of weeks or months, there is clear value in accelerating the prediction of cure profiles for these materials. Here, we enable the prediction of extended cure profiles in

slow reacting systems, where the kinetics change in a discontinuous manner over the course of many hours or days.

4.3 Materials and Methods

HTPB was obtained from RCS Rocket Motor Components with a number average molecular weight of M_n = 2700 g mol^{-1} and functionality of 2.16. Functionality f was determined using Equation (4.1).

$$f = \frac{(M_n)(OH)}{1000 * M_{w_{KOH}}} \tag{4.1}$$

The hydroxyl number OH is 44.88, and the molecular weight of potassium hydroxide $M_{w_{KOH}}$ is 56.1 g mol^{-1}. Since hydroxyl number must be expressed in units of milliweight per weight, a factor of 1000 is included. The hydroxyl number was calculated using Equation (4.2), where OH_{eq} is the hydroxyl equivalent weight, which is equal to 1250 according to the manufacturer.

$$OH = \frac{1000 * M_{w_{KOH}}}{OH_{eq}} \tag{4.2}$$

IPDI was supplied by Oakwood Chemical. The stoichiometric ratio, r, representing the ratio of the hydroxyl groups relative to isocyanate groups was set to 1 for our reactions, shown in Equation (4.3):

$$r = \frac{[OH]}{[NCO]} = 1 \tag{4.3}$$

A stoichiometric ratio of 1 was chosen to limit the amount of unreacted material at the end of the cure and avoid side reactions. Samples were mechanically mixed via high shear with a

mixing paddle blade for one minute. After mixing, samples were promptly loaded onto the rheometer plate or KBr window for characterization.

4.3.1 Chemorheology

A Discovery HR 30 Rheometer (TA Instruments, Newcastle, DE, USA) with stainless steel 25 mm parallel plates was used for all rheological tests. Time sweeps were conducted for up to four days, or until the reaction appeared to reach completion, in oscillatory mode at 0.1% strain with an initial gap of 1 mm. The reaction was deemed complete once the viscosity profile plateaued. A constant normal force of 0.0 ± 0.1 N was applied to ensure no material was spilled out of the sides of the plates during early stages of the reaction. This level of normal force control also prevented negative normal forces from occurring during the cure process when shrinkage was apparent. Controlled strain using non-iterative sampling was applied to set a minimum torque of 5 μN-m, which increased the resolution of the data during early periods of the reaction (i.e. when viscosity was very low). The auto strain adjustment feature was also employed to remain within the linear viscoelastic region for the duration of the cure. Storage modulus (G'), loss modulus (G''), and complex viscosity (η^*) were obtained at 60, 70, and 80°C. The temperature was maintained using the environmental test chamber attachment. The Cox-Merz rule has been validated by previous studies for similar materials, suggesting that oscillatory measurements of complex viscosity are equivalent to measurements of shear viscosity in continuous flow [20].

4.3.2 Fourier Transform Infrared Spectroscopy

FTIR curing studies were performed in transmittance mode using a temperature-controlled demountable cell (PIKE Technologies, Fitchburg, WI, USA) in a Nicolet iS-50 FTIR Spectrometer. Samples were prepared using the same procedure as chemorheology studies. The

heated cell was allowed to reach the desired temperature and equilibrate for 15 minutes before each experiment. The HTPB+IPDI resin was then deposited between two KBr windows using a 50 μm pathlength Teflon spacer. The samples were cured at 60, 70, and 80°C for the same timeframes as their respective chemorheology experiments. Spectroscopy data was gathered at 30-minute intervals by averaging 32 scans with a resolution of 2 cm^{-1}.

4.4 Results and Discussion

There are several major goals for this study. Using chemorheology, we aim to analyze the cure kinetics of an uncatalyzed multi-day reaction that was previously studied for only up to 10 hours. Utilizing a variety of fitting techniques, we match our data to previously developed models for the purpose of predicting multi-day cure reactions. Temperature controlled FTIR is used to validate the presence of a multi-stage reaction, and rheokinetic modeling parameters are subsequently compared to FTIR spectroscopy results. This process facilitates a discussion regarding the advantages and shortcomings of each method, along with appropriate non-linear curve fitting techniques. Transition state theory for multi-day reactions is then explored to understand the associative mechanism during polyurethane synthesis, which helps explain the sluggish nature of the reaction, while providing support for autocatalytic process. This information is vital to understanding the underlying reaction mechanism while providing quantitative kinetic data for prediction of long-term curing behavior.

4.4.1 Cure Profile

Because the isocyanate groups on IPDI are asymmetrically reactive, Lee et al. suggested that reactivity of the secondary isocyanate group is more favorable than the primary group [21]. Guo et al. had similar findings, and cited a study by Rochery, which concluded that due to the

substitution effect, after one isocyanate group reacts, the second is slower to react. Out of the eight possible isomers of IPDI, the one with functional groups in the equatorial position is most prominent, with the primary isocyanate group reacting slower [22, 23]. An illustration of this reaction is presented in Figure 4.1.

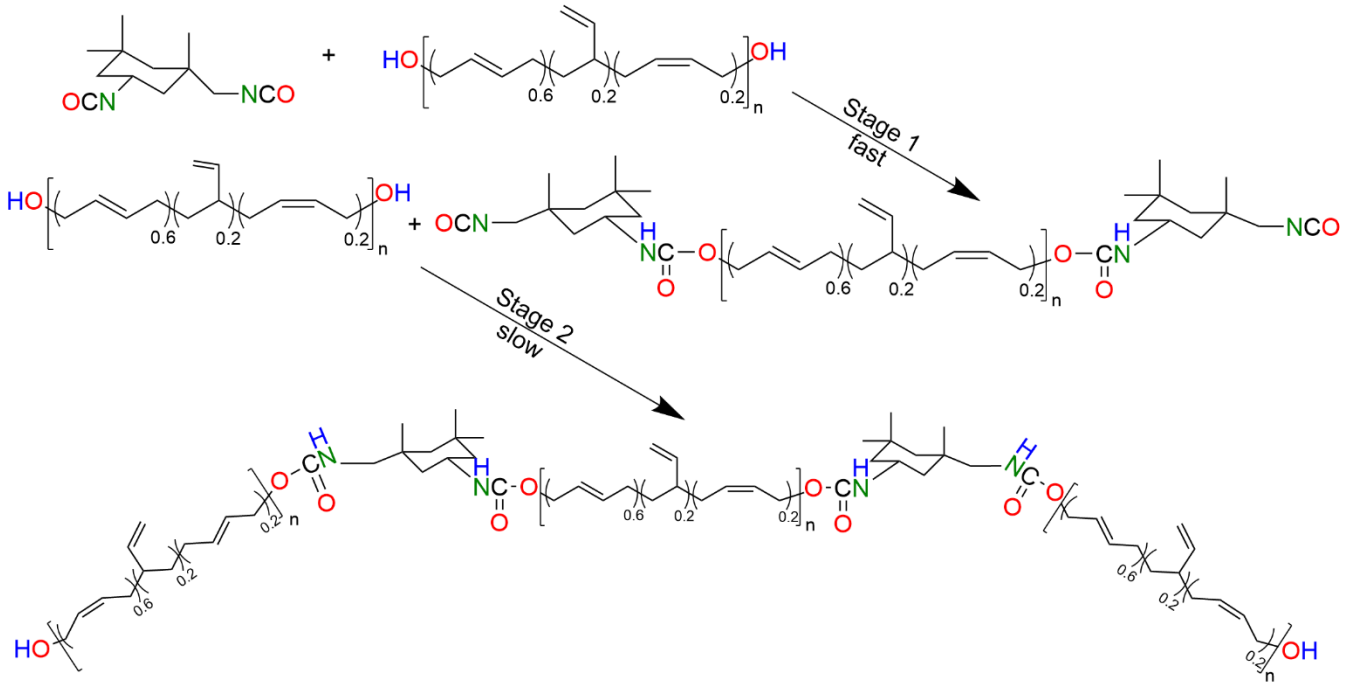

Figure 4.1: Two-step process of linear polyurethane formation involving a fast step (secondary isocyanate reaction) followed by a slow, delayed step (primary isocyanate reaction), assuming that the most prominent isomer drives reactivity.

Each stage of the reaction can be observed using viscosity profiles from torsional rheology. Typically, one would expect an initial increase in viscosity due to monourethane formation, followed by a delayed increase associated with diurethane development. Previous authors successfully verified this two-stage viscosity buildup using uncatalyzed HTPB+TDI, but sufficiently long timescales were not achieved during their tests to observe this two-stage behavior for uncatalyzed HTPB+IPDI.[4] To fill this gap in knowledge and generalize this approach for

other, slow reacting diisocyanates, a multi-day cure of uncatalyzed HTPB+IPDI is illustrated in Figure 4.2.

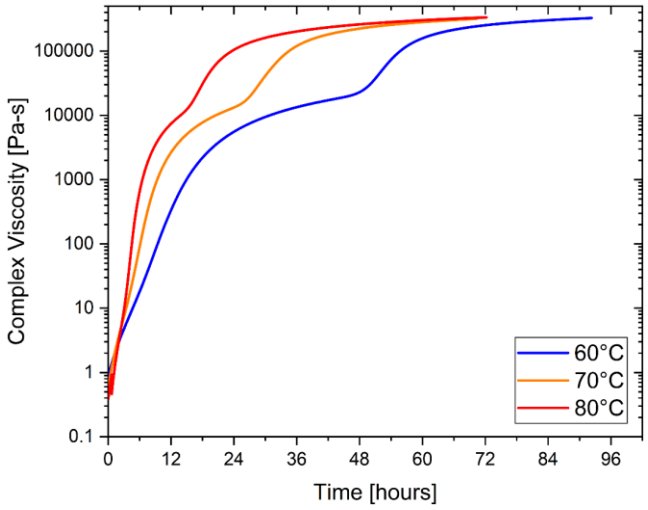

Figure 4.2: Viscosity buildup of HTPB+IPDI during polymerization over the course of multiple days.

Without a catalyst present, the curing behavior appears to depict a unique non-linear viscosity buildup. First, as the secondary group on the IPDI molecule reacts, there is rapid growth of viscosity. Then, a plateau of the viscosity appears, after which viscosity once again increases due to the primary group of the diisocyanate reacting. Finally, there is a second plateau once the reaction finishes. The length of the first plateau is dependent on the reaction temperature, shortening with increasing temperature. The fact that the first plateau has the same viscosity range for the three different cure temperatures suggests that upon monourethane formation, the reaction becomes limited by the diffusion of the monourethane throughout the system. Because this novel behavior has not been previously reported in literature, it is essential that the conversion progress is directly verified through Fourier transform infrared spectroscopy. These results enable kinetic

modeling using a variety of experimental setups, which provides useful information regarding the prediction of cure profiles for long-term polymerizations.

4.4.2 Fourier-Transform Infrared Spectroscopy

Temperature controlled FTIR studies were conducted at the same temperatures and timeframes as the rheological studies in order to directly quantify the degree of cure. This way, it is possible to confirm the presence of a two-stage reaction, such that subsequent modeling can be performed to predict reaction progress. Conversion during FTIR is calculated using Equations (4.4) and (4.5) [22].

$$\alpha_{NCO} = \frac{\left(\frac{A_{2260}}{A_{1640}}\right)_{t=0} - \left(\frac{A_{2260}}{A_{1640}}\right)_{t}}{\left(\frac{A_{2260}}{A_{1640}}\right)_{t=0}} \tag{4.4}$$

$$A = 2 - \log(T) \tag{4.5}$$

In Equations (4.4) and (4.5), A is the absorbance of a peak at a given wavenumber, α_{NCO} is the conversion of the isocyanate bond, t is time, and T is the transmittance of a given peak. The peak at 2260 cm^{-1} is representative of the NCO peak which increases in transmittance over time as it converts to urethane linkages. The selected reference band at 1640 cm^{-1} is representative of the C=C reference band and does not change meaningfully during the reaction [22]. The rate of isocyanate conversion as a function conversion progress is illustrated in Figure 4.3.

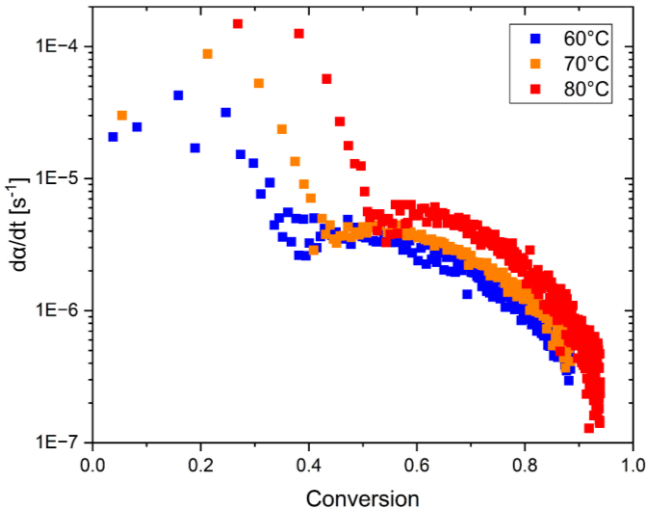

Figure 4.3: Reaction rate as a function of isocyanate conversion during FTIR analysis. A semi-log plot is used to emphasize the presence of two distinct reaction rate peaks.

Figure 4.3 illustrates two peak reaction rates during polymerization. There is an initial, large peak between 0-50% conversion, and then a second smaller peak between 50-100% conversion. These peaks are representative of the maximum reaction rates during secondary and primary isocyanate conversion, respectively. This finding provides evidence that the two stages of viscosity growth present in Figure 4.2 occur due to reaction of these functional groups, such that reaction of the secondary group drives an initial increase in viscosity, followed by a slower delayed growth in viscosity due to reactivity of the primary isocyanate. As such, we have verified the presence of a two-stage reaction process, and can apply a series of modeling/curve fitting techniques to validate the unique diffusion controlled regime found in Figure 4.2.

4.4.3 Chemorheological Modeling

The Arrhenius equation empirically relates the rate of a chemical reaction to a change in temperature as shown in Equation (4.6).

$$k = Ae^{-\frac{E_a}{RT}} \tag{4.6}$$

In this case, k is a reaction rate constant, E_a is the activation energy, T is the absolute temperature, and A is the pre-exponential factor. The exponential form in Equation (4.6) is often linearized using logarithmic transformations, which enables the activation energy and pre-exponential factor to be quantified across a short range of temperatures. For rheological experiments, this form of the equation presents an issue since rate constants are not known. Fortunately, alternative approaches for applying an Arrhenius relationship to viscoelastic data for crosslinking polymers have been discussed in previous studies, and are hypothesized to be appropriate for oligomeric precursors such as HTPB [13]. The steps to construct such a plot are outlined in Equations (4.7), (4.8), and (4.9).

$$\ln \eta^*(t) = \ln \eta_r + kt \tag{4.7}$$

$$\eta_r = \eta_\infty e^{\left(\frac{\Delta E_\eta}{RT}\right)} \tag{4.8}$$

$$k = k_\infty e^{\left(\frac{\Delta E_k}{RT}\right)} \tag{4.9}$$

η^* is the complex viscosity, η_r and k are the temperature dependent viscosity and rate constants, η_∞ and k_∞ are the infinite temperature viscosity and rate constants, ΔE_η and ΔE_k are the temperature-independent activation energies associated with viscosity and reaction rate, respectively, R is the universal gas constant, and T is temperature in Kelvin [13]. The Arrhenius approach presented here analyzes a distinct linear section of a semi-log plot of viscosity as a function of time, with the intent to fit the complex viscosity using both temperature dependent viscosity and rate constants. As confirmed through FTIR, these types of polyurethane formations possess two stages of polymerization (and consequently, two stages of viscosity buildup). Hence, it is possible to identify two linear sections of the semi-log viscosity plot, whereby the viscosity

increases rapidly at first, then plateaus before increasing again as a result of the primary functional group reacting. Application of the two-stage Arrhenius model at three different temperatures is illustrated in Figure 4.4.

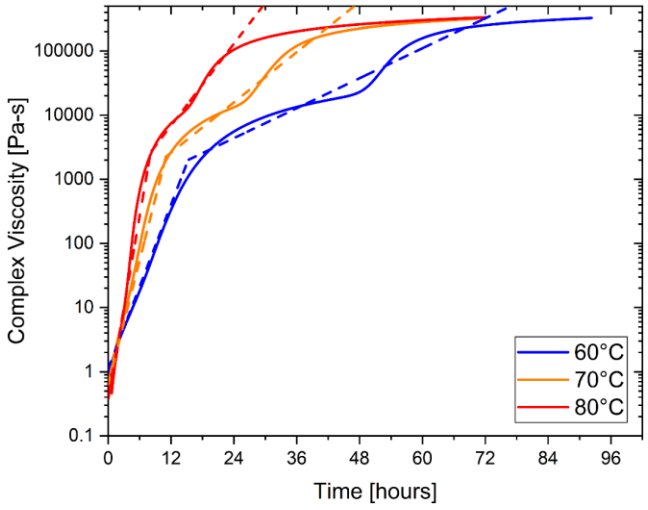

Figure 4.4: Two-stage Arrhenius model depicting the time and temperature dependence of viscosity buildup during curing. Solid lines (—) indicate empirically measured viscosity, while dashed lines (- -) represent the Arrhenius model.

To accurately capture this unique curing behavior, the second stage of the Arrhenius approach uses all data points from the beginning of the first plateau to the beginning of the second plateau. This region was chosen for the second stage analysis to enable continuous prediction across the entire reaction timeframe. All kinetic parameters of the two-stage Arrhenius model are presented in Table 4.1.

Table 4.1: Kinetic parameters from the two-stage Arrhenius model.

	ΔE_k	ΔE_η	k_∞	η_∞
	[kJ mol^{-1}]	[kJ mol^{-1}]	[s^{-1}]	[Pa-s]

Stage 1	39.2	53.4	190	4.64×10^{-9}
Stage 2	49.1	16.4	1260	1.39

Correlation coefficients for each stage of the Arrhenius model were above 0.95 at each temperature. Because the Arrhenius model will inevitably deviate from the data in the second stage due to completion of the curing process, correlation coefficients were only applied up until the model began to deviate from the second plateaued region. This finding supports the conclusion that HTPB+IPDI systems indeed show two-stage viscosity buildup, and prediction of these profiles is relatively straightforward from a computational standpoint.

While the Arrhenius model expectedly illustrates that ΔE_k increases from stage 1 to stage 2, k_∞ is also higher for stage 2. This stands in contrast to FTIR results in Figure 4.3, which suggest that the secondary group (stage 1) reacts faster than the primary group (stage 2). These findings highlight the subjectivity involved when choosing a region of linearity, which can influence results. Thus, while this approach offers a quantitative method for analyzing activation energy and rate constants, it requires several assumptions of linear reaction progress, and presumes a direct relationship between viscosity growth and isocyanate conversion. To address this challenge, degree of conversion profiles can be used which enable a more rapid and accurate representation of reaction progress compared to viscosity patterns alone, which is especially pertinent when comparing dissimilar systems. Approaches such as the Kamal-Sourour model relax these assumptions by applying power law relationships to conversion profiles, which captures complex kinetic behavior, as shown in Equation 4.10.

$$\frac{d\alpha}{dt} = (k_1 + k_2\alpha^a)(1-\alpha)^b \tag{4.10}$$

Here, α is the conversion, k_1 and k_2 are reaction rate constants, a and b are reaction order constants, and t is time. It has been suggested that when $a < 1$, the autocatalytic effect has a higher contribution to the overall reaction rate [15]. To determine conversion from rheological experiments, the storage modulus can be used as a proxy measurement to quantify the degree of cure. This is accomplished by relating the storage modulus at a given timepoint to the initial and final cured modulus [24]. The model has been used widely to study cure behavior and is listed in Equation (4.11) [15, 20].

$$\alpha = \frac{G'_t - G'_0}{G'_\infty - G'_0} \tag{4.11}$$

In this way, G'_t is the storage modulus at a given time, G'_0 is the initial storage modulus, and G'_∞ is the storage modulus at the end of the reaction. Previous studies provided a theoretical basis for estimating k_1, as well as the relationships among reaction order parameters, with the intention of creating clear bounds during curve fitting [15]. Assuming $k_1 \ll k_2$, the derivative of Equation (4.10) with respect to conversion is null at the peak reaction rate. This yields $\alpha_{peak} = a/(a+b)$, where α_{peak} is the conversion at peak reaction rate. At low conversions (i.e. $\alpha \approx 0$), k_1 can be approximated as the conversion rate. There is a small, plateaued section at the beginning of the reaction where this can be approximated as observed in Figure 4.5(b). Non-linear curve fitting is used to solve for the remaining variables; this method is henceforth termed "estimation of parameters". Alternatively, non-linear fitting can be used to solve for *all* parameters, without accurately estimating parameters initially. The isocyanate conversion progress as a function of time can be found in Figure 4.5(a), and the Kamal-Sourour model with and without estimation of parameters is represented in Figure 4.5(b).

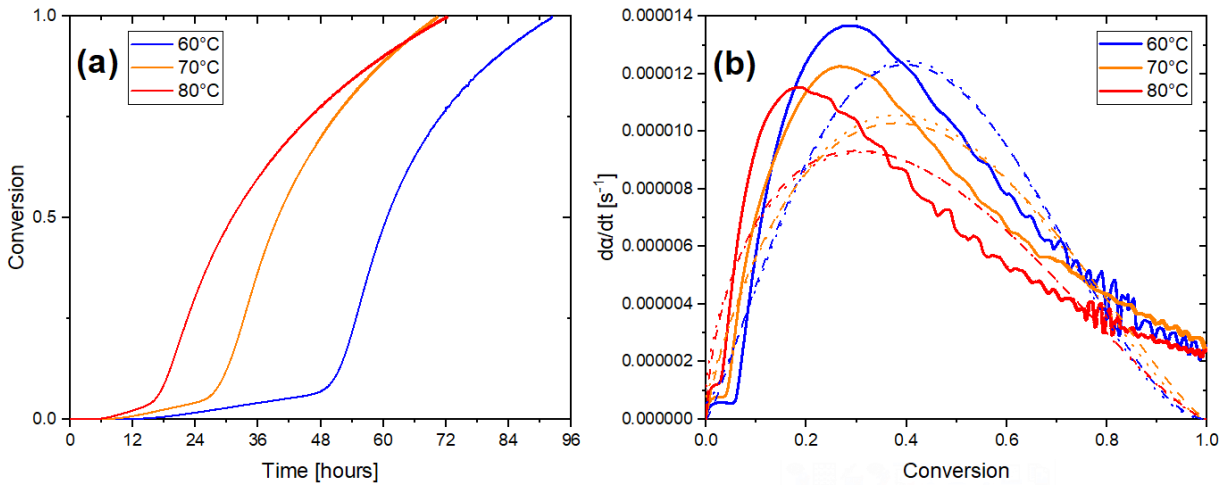

Figure 4.5: (a) Conversion as a function of time using storage modulus as a proxy for conversion. (b) Reaction rate as a function of conversion during chemorheology. Solid lines (—) represent raw conversion using storage modulus, dashed lines (- -) are fitted using the Kamal-Sourour model by estimation of parameters, and dotted lines (⋯) do not use the estimation of parameters method.

Since data was collected at approximately 6 second intervals, local fluctuations in the viscoelasticity were apparent. To smooth the data and reduce noise, Savitzky-Golay smoothing (2nd order, 800 points of window) was used. This type of noise reduction applies a local polynomial regression to the nearest 800 datapoints, which introduces a smoothed value of the conversion rate at each level of conversion.

In both fitting methods, the model adequately represents the reaction rate, but the non-zero reaction rate at the end of the experiment, as well as the assumption that 100% conversion was reached, limited the prediction capability of the model. Comparable reaction rates can be found in literature when using the "estimation of parameters" method, listed in Table 4.2 [15, 20]. Specifically, k_1 and k_2 here are comparable to Butacene-TDI and Butacene-HMDI systems, which

is encouraging given the similarity between the chemical structures. Additionally, the reaction order constant *a* is similar across both bodies of literature, although for this HTPB+IPDI system, *b* appears to be quite large. This is likely a result of the reaction rate being non-zero at the end of the experiment which results in the overestimation of *b*. On the other hand, when the parameters are fitted without first accurately estimating their initial values (Table 4.3), k_1 becomes unreasonably low (note values listed are multiplied by 10^{21} in Table 4.3), which makes its physical significance less meaningful. For this reason, even though both methods provide adequate fits to the data, the estimation of parameters technique appears to provide more context for the reaction process. Furthermore, although the conversion profiles in Figure 4.5(a) did not completely plateau, sufficient reaction progress was obtained to adequately capture the most important kinetic processes during this timescale. This finding is substantiated by FTIR results in Figure 4.3, which highlights that there was approximately 90% conversion of isocyanates at these timescales and temperatures.

Table 4.2: Kinetic parameters of the Kamal-Sourour model using estimation of parameters, with comparison to one body of literature. Literature data is denoted with the subscript *lit* [15].

Temperature [°C]	$k_1 \times 10^5$ [s^{-1}]	$k_2 \times 10^5$ [s^{-1}]	a	b	r^2	$k_{1,lit} \times 10^5$ [s^{-1}]	$k_{2,lit} \times 10^5$ [s^{-1}]	a_{lit}	b_{lit}
60	0.0562	12.4	0.83	3.94	0.85	0.0100	2.28	0.44	1.61
70	0.0774	5.41	0.56	3.04	0.82	0.0278	3.55	0.36	1.47
80	0.113	3.26	0.32	3.42	0.76	0.0293	8.25	0.37	1.38

Table 4.3: Kinetic parameters of the Kamal-Sourour model with only non-linear fitting.

Temperature [°C]	$k_1 \times 10^{21}$ [s^{-1}]	$k_2 \times 10^5$ [s^{-1}]	a	b	r^2

60	7.04	0.102	0.43	6.38	0.86
70	431	0.043	0.30	4.15	0.84
80	4.03	0.031	0.31	2.93	0.79

Correlation coefficients, r^2, quantitatively suggest that the Kamal-Sourour model adequately fits the data. Additionally, when k_1 is much less than k_2, there is an implied autocatalytic affect taking place, where a product of the reaction contributes towards the overall reaction rate [20]. This finding is confirmed here, with an apparent decrease in the contribution of the autocatalytic effect towards overall reaction rate with increasing temperature (i.e. the difference between k_1 and k_2 decreases with temperature). To further substantiate this claim, curve fitting using the Sestak-Berggren equation was performed; similar findings were obtained regarding the degree of the autocatalytic effect towards overall reaction progress, which can be found in the supporting information.

Figure 4.5(b) suggests that there is only one reaction peak present during chemorheological analysis. This single peak contrasts the two peaks identified during FTIR analysis in Figure 4.3. A potential reason for this is that viscoelastic properties such as storage modulus increase nonlinearly with conversion, which results in a discrepancy between the two methods. Specifically, conversion using viscoelastic properties likely underestimates reaction progress early in the reaction, such that the Kamal-Sourour analysis in Figure 4.5(b) only captures the second stage of the reaction (primary isocyanate conversion). To confirm this hypothesis, a Kamal-Sourour analysis was performed on the FTIR data from 50% conversion onwards (i.e. secondary isocyanate conversion finished, and only primary isocyanate conversion was modeled using the second, smaller peak in Figure 4.3). The results are presented in Figure 4.6 and quantified in Table 4.4.

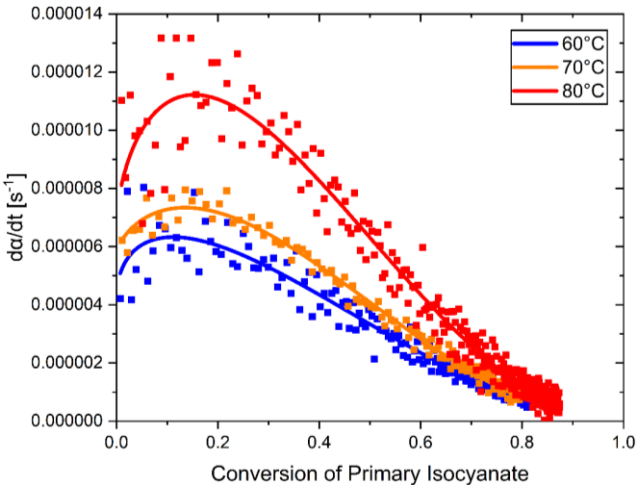

Figure 4.6: Kamal-Sourour analysis of truncated FTIR results, which models primary isocyanate conversion. Square dots (■) illustrate the raw conversion data using absorbance values, and solid lines (—) represent the results of curve fitting to the Kamal-Sourour model.

Table 4.4: Kamal-Sourour kinetic parameters from FTIR analysis.

Temperature [°C]	$k_1 \times 10^5$ [s^{-1}]	$k_2 \times 10^5$ [s^{-1}]	a	b	r^2
60	0.42	1.09	0.33	2.90	0.94
70	0.58	1.98	0.41	4.35	0.99
80	0.68	3.10	0.65	2.10	0.96

The rheokinetic parameters from chemorheology experiments in Table 4.2 generally align with the kinetic parameters from the truncated FTIR results in Table 4.4. This finding suggests that the Kamal-Sourour model during chemorheological testing predominately models primary isocyanate reactivity in stage 2 of the reaction, which results from nonlinear relationships between increases in viscoelastic properties during polymerization and conversion progress. One exception to this parameter agreement is k_1 which is approximately an order of magnitude higher for FTIR compared to chemorheology. This once again likely results from the nonlinear relationships

between reaction kinetics and viscoelasticity, which predisposes rheological analyses to underestimate reaction progress early during polymerization.

As a result, several arguments supporting the presence of an autocatalytic reaction during FTIR experiments can be made. Table 6 indicates that $k_1 << k_2$, and difference between k_1 and k_2 decreases with increasing temperature. Furthermore, the reaction rate order constant a is less than 1 at each reaction temperature. These findings were present during both the chemorheological and spectroscopic analyses; thus, there is further verification of an autocatalytic reaction [15].

As emphasized previously, the corroboration of kinetic parameters using chemorheology (Table 4.2) and truncated FTIR data (Table 4.4) suggests that the rheokinetic model in Figure 4.5(b) is primarily identifying large molecular weight growth during diurethane formation. Thus, rheokinetic modeling of multi-stage reactions is marginally less effective than FTIR at screening for early onset reactions which exhibit minimal molecular weight growth. The inability of the Kamal-Sourour model to detect early-stage reactivity during chemorheological testing is believed to occur because conversion data using rheology is based on increases in viscoelastic properties. For the first stage of conversion, molecular weight growth is insignificant given the chain length of the oligomer – which is essentially a series of end capped prepolymers. However, the stage 2 mechanism results in significant molecular weight growth which is readily captured using the rheokinetic model in Figure 4.5(b). By contrast, FTIR effectively screens for early-onset conversion in stage 1 because it directly measures changes in absorption peaks of the NCO functional groups. These findings collectively suggest that FTIR may more effectively detect slow, low molecular weight growth reactions, but chemorheology and FTIR have similar outcomes once changes in viscoelastic properties (indicative of molecular weight growth) become a driving factor

for conversion. This finding is further confirmed in Figure S9.2.2, which illustrates how chemorheology tends to underestimate reaction progress for low molecular weight products compared to FTIR. However, it is important to note that the two-stage Arrhenius analysis using chemorheology is still effective at tracking/predicting reaction progress since the complex viscosity profiles are on a log scale; the early-stage reaction progress can be observed more clearly in this scenario compared to the linear plots required for the Kamal-Sourour analysis, although the kinetic parameters between stages are not necessarily comparable.

Importantly, these methods of chemorheological and spectroscopic characterization substantiate the conclusion that uncatalyzed HTPB+IPDI systems possess a unique cure profile that has been previously unstudied. In addition, similar systems possess comparable kinetic parameters, which suggests that the novel profiles introduced here are not artifacts of experimental setup, but rather unique characteristics of a slow reacting, uncatalyzed polyurethane.

4.4.4 Transition State Theory Analysis

Transition state theory quantifies the entropic and enthalpic activation energies of a reaction, which can be used to determine the overall reaction energy barrier of a system. Mahanta & Pathak provide a detailed approach to calculating these parameters for curing systems using Wynne-Jones-Eyring-Evans (WJEE) theory, for the purpose of unveiling the reaction mechanism of an HTPB+TDI system [5]. The generalized equation used in transition state theory is shown in Equation (4.12).

$$k_\mu = \frac{k_B T}{h} e^{\frac{\Delta S^\#}{R}} e^{-\frac{\Delta H^\#}{RT}} \tag{4.12}$$

k_μ is the temperature dependent rate constant equivalent to k found in Equation (4.7), k_B is the Boltzmann constant, h is Plank's constant, $\Delta S^{\#}$ is the activation entropy, and $\Delta H^{\#}$ is the activation enthalpy. The slope of $\ln(k_\mu/T)$ as a function of $1/T$ gives $\left(-\frac{\Delta H^{\#}}{R}\right)$, and the intercept represents $ln\left(\frac{k_B}{h}\right) + \frac{\Delta S^{\#}}{R}$. Using this information, the Gibbs energy of activation can be optionally solved using $\Delta G^{\#} = \Delta H^{\#} - T\Delta S^{\#}$. Table 4.5 provides these transition state parameters derived using the chemorheological data described previously, along with a comparison to chemorheology literature for an uncatalyzed HTPB+TDI system [5]. The plots used to calculate the experimental values in Table 4.5 can be found in Figure S9.2.3 of the supporting information.

Table 4.5: Activation energy parameters derived using transition state theory using various methods.

	$\Delta S^{\#}$ [J K^{-1}]	$\Delta H^{\#}$ [kJ]
Chemorheology (Literature) [5]	-180	33.1
Chemorheology (Experimental)	-96.9	36.4
FTIR (Literature) [25]	-198	41.1
FTIR (Experimental)	-243	33.7

As it relates to kinetics, the data presented here do not provide direct evidence of a slow reaction, but rather they specify the kinetic barrier of the saddle point during the transition state, which is useful for understanding the reaction mechanism. For example, large negative values of entropic activation energy, approaching hundreds of J K^{-1}, tend to promote associative, ordered mechanisms, leading to an overall reinforcement of the autocatalytic effect discussed previously [26]. Additionally, some works have suggested that negative entropic activation energies provide sufficient evidence for an apparent second-order rate law of HTPB+IPDI in the bulk state during

FTIR analysis [25]. Evidence of this associative mechanism is not readily apparent through the previous rheokinetic analysis, which exemplifies the need for this additional transition state analysis.

To further support these findings, WJEE analysis was performed using the FTIR results. The main challenge when utilizing FTIR data instead of chemorheological data is that k_μ cannot be gathered from the Arrhenius approach outlined in Equations (4.7)-(4.9). To address this concern, a second-order reaction is assumed which enables calculation of the rate constant using Equation (4.13) [5, 22].

$$\frac{\alpha_{NCO}}{1-\alpha_{NCO}} = kt \tag{4.13}$$

The first 10 hours of conversion data were found to accurately capture the first stage of molecular weight growth, which facilitated calculation of k in Equation (4.13). Subsequently, WJEE revealed the entropic activation energy $\Delta S^{\#}$ = -243 J K^{-1} and enthalpic activation energy $\Delta H^{\#}$ = 33.7 kJ, which are included in Table 4.5. Other researchers found similar entropic and enthalpic activation energy values for uncatalyzed HTPB+IPDI during FTIR, such that $\Delta S^{\#}$ = -198 J K^{-1} and $\Delta H^{\#}$ = 41.1 kJ [25]. These findings align with the other values discussed in Table 4.5, which supports the use of both chemorheology and FTIR for elucidating transition state kinetic parameters of multi-day curing reactions.

4.5 Conclusion

Multi-day chemorheological studies on uncatalyzed HTPB+IPDI systems, and polyurethane reactions in general, have been largely neglected due to their time requirements and the complexity of interpreting results. Although polyurethane synthesis is often catalyzed for the

sake of timeliness, we have shown through the two-stage Arrhenius analysis that unique cure profiles form under uncatalyzed conditions which causes discontinuous molecular weight growth. Understanding this non-linear cure progression is critical when building process-structure-property relationships for manufacturing methods such as reactive extrusion.

Other autocatalytic models, such as the Kamal-Sourour model, proved useful in tracking/predicting the rate of conversion based on several different kinetic parameters. The use of these models has validated the unique cure profile of uncatalyzed HTPB+IPDI reactions. Further validation of the autocatalytic effect was provided through transition state theory using WJEE analysis, which unveiled the associative, ordered mechanism of uncatalyzed polyurethane formation.

A comparison to FTIR spectroscopy was also performed to 1) verify the rheokinetic findings of this multi-day cure and 2) validate the presence of a two-stage reaction. FTIR effectively screened for early-onset conversion during monourethane formation (stage 1) because it directly measured changes in absorption peaks of the NCO functional groups. This early rate of reaction appeared faster by an order of magnitude for FTIR compared to chemorheology which resulted from nonlinear relationships between increases in viscoelasticity and reaction progress. As a result, the Kamal-Sourour model failed to detect any meaningful reaction progress during stage 1 of polymerization (i.e. reaction of the secondary isocyanate group) during chemorheological testing. However, upon reaction of the primary isocyanate group during stage 2 of polymerization, the molecular weight increased rapidly, which caused large increases in viscoelastic properties, and hence conversion rate. Truncation of the FTIR data just before stage 2 resulted in excellent agreement between kinetic parameters determined by chemorheology and

FTIR, suggesting that FTIR may more effectively detect initial, low molecular weight growth reactions compared to chemorheology alone. However, given the relatively large cost of running FTIR experiments for thermosetting reactions, there is clear value in utilizing chemorheology studies; KBr windows for FTIR experiments currently cost hundreds of dollars per experiment and cannot be reused, whereas rheometer plates can be cleaned easily, or cheap disposable plates can be utilized.

A multitude of future endeavors still exist, including studying the effect of fillers on cure behavior and exploration of unique empirical models that may more accurately grasp the complex curing behavior of uncatalyzed polyurethane reactions [27, 28]. Furthermore, methods which relate gel point conversion to viscosity buildup present a unique method of chemorheological characterization using multi-frequency time sweeps [29, 30]. For these reasons, the intersection of spectroscopy and chemorheology for multi-day curing studies should be more widely employed to facilitate the accelerated kinetic analyses presented here, especially given the limitations and constraints of non-isothermal DSC measurements in this context.

4.6 Acknowledgements

Our group would like to acknowledge funding from DEVCOM ARL through cooperative agreement W911NF-20-2-0052. We also thank the DREAMS lab at Virginia Tech for insightful scientific discussion, as well as James Brown from the Long group at Arizona State University for providing polyurethane reaction mechanism insights. This work was made possible by the use of Virginia Tech's Materials Characterization Facility, which is supported by the Institute for Critical Technology and Applied Science, the Macromolecules Innovation Institute, and the Office of the Vice President for Research and Innovation.

4.7 References

[1] M. Paulino, F. Teixeira-Dias, On the Use of Polyurethane Foam Paddings to Improve Passive Safety in Crashworthiness Applications, in: F. Zafar, E. Sharmin (Eds.), Polyurethane, IntechOpen, Rijeka, 2012.
[2] J.O. Akindoyo, M.D. Beg, S. Ghazali, M.R. Islam, N. Jeyaratnam, A.R. Yuvaraj, Polyurethane types, synthesis and applications–a review, RSC Adv. 6(115) (2016) 114453-114482. https://doi.org/10.1039/C6RA14525F.
[3] S. Chaturvedi, P.N. Dave, Solid propellants: AP/HTPB composite propellants, Arabian J. Chem. 12(8) (2019) 2061-2068. https://doi.org/10.1016/j.arabjc.2014.12.033.
[4] V. Sekkar, S. Venkatachalam, K.N. Ninan, Rheokinetic studies on the formation of urethane networks based on hydroxyl terminated polybutadiene, Eur. Polym. J. 38(1) (2002) 169-178. https://doi.org/10.1016/S0014-3057(01)00106-9.
[5] A.K. Mahanta, D.D. Pathak, HTPB-polyurethane: a versatile fuel binder for composite solid propellant, Polyurethane 1 (2012). https://doi.org/10.5772/47995.
[6] B. Lucio, J.L. de la Fuente, Non-isothermal DSC and rheological curing of ferrocene-functionalized, hydroxyl-terminated polybutadiene polyurethane, React. Funct. Polym. 107 (2016) 60-68. https://doi.org/10.1016/j.reactfunctpolym.2016.08.002.
[7] A. Olejnik, K. Gosz, Ł. Piszczyk, Kinetics of cross-linking processes of fast-curing polyurethane system, Thermochim. Acta 683 (2020) 178435. https://doi.org/10.1016/j.tca.2019.178435.
[8] S. Lee, J.H. Choi, I.-K. Hong, J.W. Lee, Curing behavior of polyurethane as a binder for polymer-bonded explosives, J. Ind. Eng. Chem. 21 (2015) 980-985. https://doi.org/10.1016/j.jiec.2014.05.004.
[9] K. Catherine, K. Krishnan, K. Ninan, A DSC study on cure kinetics of HTPB-IPDI urethane reaction, J. Therm. Anal. Calorim. 59(1-2) (2000) 93-100. https://doi.org/10.1023/A:1010127727162.
[10] C. Korah Bina, K. Kannan, K. Ninan, DSC study on the effect of isocyanates and catalysts on the HTPB cure reaction, J. Therm. Anal. Calorim. 78(3) (2004) 753-760. https://doi.org/10.1007/s10973-005-0442-0.
[11] M. Hui, L. Yu-Cun, C. Tao, H. Tuo-Ping, G. Jia-Hu, Y. Yan-Wu, Y. Jun-Ming, W. Jian-Hua, Q. Ning, Z. Liang, Kinetic studies on the cure reaction of hydroxyl-terminated polybutadiene based polyurethane with variable catalysts by differential scanning calorimetry, e-Polymers 17(1) (2017) 89-94. https://doi.org/10.1515/epoly-2016-0245.
[12] X. Zhang, Y. Liu, T. Chai, Z. Ma, K. Jia, Curing Reaction Kinetics of the EHTPB-Based PBX Binder System and Its Mechanical Properties, Coatings 10(12) (2020) 1266. https://doi.org/10.3390/coatings10121266.
[13] M.J. Bortner, V. Bhanu, J.E. McGrath, D.G. Baird, Shear rheological properties of acrylic copolymers and terpolymers suitable for potentially melt processable carbon fiber precursors, J. Appl. Polym. Sci. 93(6) (2004) 2856-2865. https://doi.org/10.1002/app.20833.
[14] B. Lucio, J.L. de la Fuente, Rheological cure characterization of an advanced functional polyurethane, Thermochim. Acta 596 (2014) 6-13. https://doi.org/10.1016/j.tca.2014.09.012.
[15] B. Lucio, J.L. de la Fuente, Kinetic and chemorheological modelling of the polymerization of 2, 4-Toluenediisocyanate and ferrocene-functionalized hydroxyl-terminated polybutadiene, Polymer 140 (2018) 290-303. https://doi.org/10.1016/j.polymer.2018.02.058.
[16] P. Šimon, Fourty years of the Šesták–Berggren equation, Thermochim. Acta 520(1-2) (2011) 156-157. https://doi.org/10.1016/j.tca.2011.03.030.

[17] C. Prasad, S. Babu, P.K. Raju, V. Ranganathan, K. Ninan, Effect of process parameters and cure catalysis on the HTPB-IPDI based solid propellant behavior, International Journal of Novel Research and Development 3(4) (2018).
[18] V. Sekkar, T.S.K. Raunija, Issues Related with Pot Life Extension for Hydroxyl-Terminated Polybutadiene-Based Solid Propellant Binder System, Propellants Explos. Pyrotech. 40(2) (2015) 267-274. https://doi.org/10.1002/prep.201400054.
[19] B. Lucio, J.L. de la Fuente, Rheokinetic analysis on the formation of metallo-polyurethanes based on hydroxyl-terminated polybutadiene, Eur. Polym. J. 50 (2014) 117-126. https://doi.org/10.1016/j.eurpolymj.2013.10.013.
[20] B. Lucio, J.L. de la Fuente, Chemorheology and Kinetics of High-Performance Polyurethane Binders Based on HMDI, Macromol. Mater. Eng. 306(3) (2021) 2000617. https://doi.org/10.1002/mame.202000617.
[21] S. Lee, C.H. Choi, I.-K. Hong, J.W. Lee, Polyurethane curing kinetics for polymer bonded explosives: HTPB/IPDI binder, Korean J. Chem. Eng. 32(8) (2015) 1701-1706. https://doi.org/10.1007/s11814-014-0366-y.
[22] J. Guo, T. Chai, Y. Liu, J. Cui, H. Ma, S. Jing, L. Zhong, S. Qin, G. Wang, X. Ren, Kinetic research on the curing reaction of hydroxyl-terminated polybutadiene based polyurethane binder system via FT-IR measurements, Coatings 8(5) (2018) 175. https://doi.org/10.3390/coatings8050175.
[23] M. Rochery, I. Vroman, T.M. Lam, Kinetic model for the reaction of IPDI and macrodiols: study on the relative reactivity of isocyanate groups, 37 (2000). https://doi.org/10.1081/MA-100101092.
[24] G. Santhosh, S. Reshmi, C.R. Nair, Rheokinetic characterization of polyurethane formation in a highly filled composite solid propellant, J. Therm. Anal. Calorim. 140(1) (2020) 213-223. https://doi.org/10.1007/s10973-019-08793-6.
[25] D. Kincal, S. Özkar, Kinetic study of the reaction between hydroxyl-terminated polybutadiene and isophorone diisocyanate in bulk by quantitative FTIR spectroscopy, J. Appl. Polym. Sci. 66(10) (1997) 1979-1983.
[26] B. Lucio, J.L. de la Fuente, Kinetic and thermodynamic analysis of the polymerization of polyurethanes by a rheological method, Thermochim. Acta 625 (2016) 28-35. https://doi.org/10.1016/j.tca.2015.12.012.
[27] R. Lade, K. Wasewar, R. Sangtyani, A. Kumar, D. Shende, D. Peshwe, Influence of the addition of aluminium nanoparticles on thermo-rheological properties of hydroxyl-terminated polybutadiene-based composite propellant and empirical modelling, J. Therm. Anal. Calorim. 138(1) (2019) 211-223. https://doi.org/10.1007/s10973-019-08149-0.
[28] B.M. Bandgar, K.C. Sharma, T. Mukundan, V.N. Krishnamurthy, Rheokinetic modeling of HTPB–TDI and HTPB–DOA–TDI systems, J. Appl. Polym. Sci. 89(5) (2003) 1331-1335. https://doi.org/10.1002/app.12254.
[29] O. Yuksel, M. Sandberg, I. Baran, N. Ersoy, J.H. Hattel, R. Akkerman, Material characterization of a pultrusion specific and highly reactive polyurethane resin system: Elastic modulus, rheology, and reaction kinetics, Composites, Part B 207 (2021) 108543. https://doi.org/10.1016/j.compositesb.2020.108543.
[30] D.S. Kim, C.W. Macosko, Reaction kinetics and chemorheology of a highly reactive PU system, Korea Polym. J. 4(1) (1996) 54-60.

Chapter 5

A Rheological Method to Predict Printability of High Solids Content Inks via Ultraviolet-Assisted Material Extrusion

5. A Rheological Method to Predict Printability of High Solids Content Inks via Ultraviolet-Assisted Material Extrusion

John P. Reynolds[a,b], Daniel A. Rau[b,c], Christopher B. Williams[b,c], Michael J. Bortner[*a,b]

[a]Department of Chemical Engineering, Virginia Tech, Blacksburg, VA 24061

[b]Macromolecules Innovation Institute, Virginia Tech, Blacksburg, VA 24061

[c]Department of Mechanical Engineering, Virginia Tech, Blacksburg, VA 24061

*Corresponding author | mbortner@vt.edu | 245 Goodwin Hall, 635 Prices Fork Road, Blacksburg, VA 24061

This chapter is presented as a research article published in the *Additive Manufacturing* journal.

J.P. Reynolds, D.A. Rau, C.B. Williams, M.J. Bortner, A rheological method to predict printability of high solids content inks via ultraviolet-assisted material extrusion, Addit. Manuf. (2023) 103753.

5.1 Abstract

A major challenge faced during material extrusion of highly loaded viscous ink suspensions is disruption of the interparticle network, which causes the extrudate to temporarily remain fluidic on the build bed. As a result, print quality and height retention diminish due to spreading/sagging of the extruded bead. One way to mitigate this thixotropic behavior is via in situ exposure to ultraviolet light, which partially solidifies the material as it is deposited. The rheological approach proposed here – the UV-assisted three interval thixotropy test – uses stepwise changes in strain to determine the recoverability of a highly filled, photocurable ink. The strain is altered in a low-high-low fashion, such that UV light can be turned on in the third interval to improve structural recovery. Improvements in structural recovery are realized as increases in the rate of modulus recovery and the final recovered modulus. These viscoelastic properties are used to quantify structural deformation/recovery parameters, as well as the mutation number. The parameters are compared to print heights measured during single- and multi-layer printing studies. From this analysis, we are able to determine the maximum filler loading level where UV light positively impacts print height (i.e. the percolation threshold); beyond this concentration, only print resolution improves. It is revealed that highly filled inks below the percolation threshold rely on improvements in the rate of modulus recovery to become printable – although multi-layer builds still suffer structurally. Conversely, when UV light is applied to highly loaded systems beyond the percolation threshold, improvements in build quality are driven by relatively higher levels of the final recovered modulus. These findings highlight this rheological method's ability to predict printability limits, decrease experimentation time and reduce sample waste dramatically compared to printing studies alone.

5.2 Introduction

Additive manufacturing (AM) technologies are rapidly expanding as an area of interest for engineers and investors due to their ability to produce geometrically complex products with minimal waste at potentially lower costs compared to subtractive manufacturing methods [1, 2]. These products are built in a layer-wise fashion such that the dimensional accuracy of each layer is vital towards the overall mechanical properties and quality of the printed product. Because of the pressure-driven design, direct ink write (DIW) 3D printing has become a staple for highly viscous and/or colloidal systems [3]. Here, we use the terms "highly filled," "high solids content," or "highly loaded" to describe a matrix which has been filled with a sufficiently large (often >40 vol%) amount of solid fillers such that interparticle interactions (e.g. Van der Waals forces) cannot be ignored [4, 5]. Typically, DIW works by applying pressure to a plunger which dispenses the material through a nozzle at a given rate. This method has the advantage of start-stop deposition similar to fused filament fabrication, but operates at ambient temperature allowing for extrusion of non-thermoplastic materials. Major advancements in this area have allowed for 3D printing of various highly loaded materials, including large concrete structures, cellulose, glass/carbon fiber reinforced polymers, clays, a variety of reactive fillers, and even food products [6-11].

The rheology of these high solids content inks is a growing field of interest with constant developments in material formulation and testing protocol [12]. As the filler concentration increases, yield stresses form such that a stress threshold must be exceeded in order for flow to occur [13]. When subjected to these large shear stresses or shear rates, highly filled materials decrease in viscosity and modulus due to the effects of shear thinning and interparticle network disruption. These viscoelastic parameters take time to recover as the interparticle network reestablishes itself, resulting in a form of hysteresis known as thixotropy [14]. This phenomenon is especially prominent during DIW extrusion – whereby highly thixotropic inks continue to flow

out of a printing nozzle even after extrusion pressure has been halted [15]. Thixotropic materials which fail to recover their storage modulus quickly on the build-bed will spread excessively post-extrusion [16]. In fact, the high shear region of the nozzle contributes significantly to interparticle network disruption, which causes the extrudate to collapse after deposition [17]. Thus, a pervasive issue in DIW systems is the lack of structural stability for multi-layer builds. Without sufficient strength, stacked layers will yield under their own weight, resulting in buckling or sag [18].

In an effort to mitigate this behavior, a growing body of literature has looked at using *in situ* UV light to partially or fully cure the material during printing, thus increasing the recovered modulus and preventing the effects of sag post-extrusion [19]. This process is typically denoted as UV-assisted direct ink write (UV-DIW) and is well established in literature. For example, work from Tu et al. (2021) explored the use of a dual-cure mechanism for UV-DIW in vinyl esters; an *in situ* UV light partially cured the extrudate to preserve the shape of the printed bead, and a subsequent thermal cure was used to fully crosslink the printed product [20]. Other works by Kopatz et al. (2021) focused on a dual-cure approach to printing epoxy/acrylate resins by using UV-DIW, followed by a post-print UV flood cure *and* thermal cure [21]. Hysteresis can also be mitigated through dual-component, reactive, thermosetting mechanisms which quickly build storage modulus, thus promoting interlayer adhesion and increasing the resolution of vertical builds [22].

To the authors' knowledge, rheological protocols which can assess/predict printability for highly filled UV-DIW processes have not been developed. A variety of rheological techniques attempt to characterize or predict the printability of high solids content inks, but an overwhelming majority of this research still relies on "visual inspection or image analysis" to determine print

quality [17]. In other words, visualization of a material after it has been printed is currently the most reliable way to determine printability. One of the most common rheological techniques for measuring thixotropy – the thixotropic loop – characterizes the degree of hysteresis by increasing the shear rate over time, followed by a decreasing of the shear rate on a torsional rheometer. When plotting the viscosity as a function shear rate, the area between the two curves is used as a quantitative measure of hysteresis. Unfortunately, this technique is heavily influenced by rotor inertia, the maximum shear imposed, and the loading/preparation history of the material before testing [14, 23]. The slow ramping of shear rate is also not representative of the DIW process.

With regards to the DIW process, a more representative way to assess the recovery of a material after periods of high stress, strain, or shear rate is the three interval thixotropy test (3ITT). This method works in three steps. First, small amplitude oscillatory shear (SAOS) is used to gather low strain modulus data within the linear viscoelastic region (LVR). The modulus data collected here represents "at rest" behavior of the material within the barrel of the print head. The shear strain is then immediately increased in the second interval using large amplitude oscillatory shear (LAOS), which increases the stress on the sample and mimics the large stresses/strains experienced during extrusion. These large stresses decrease both the viscosity and storage modulus of the sample due to interparticle network disruption. In the third interval, there is a return to low strains, which represents the material after it has been extruded and is sitting on the build bed. During this period, viscoelastic properties recover to their original values – sometimes incompletely [24].

Numerous variations of this technique have been previously explored in literature, but without regard to UV-reactive systems. Researchers have previously reported instantaneously changing the strain between intervals and tracking recovery using modulus data [15, 24]. To

simulate the large shear stresses *and* shear rates experienced during DIW, other researchers have increased *both* the strain and frequency during the second interval [25]. Related studies have also found use for 3ITT in steady shear rotation, where the shear rate is increased from 0.1 s^{-1} to 200 s^{-1} and then back to 0.1 s^{-1} (although this method does not allow modulus data to be gathered, which is vital towards arguments regarding viscoelasticity) [26]. More innovative approaches to 3ITT explored oscillation-rotation-oscillation protocols, which enable LVR measurements during baseline and recovery, while allowing for more significant network destruction in the second interval compared to oscillation alone [27]. Evidently, the 3ITT protocol can be altered in many ways for a variety of materials to simulate DIW, but UV-reactive, highly filled polymers have been largely neglected thus far.

Here, we introduce a novel version of the 3ITT that is specifically designed to be representative of the UV-DIW process: the UV-assisted three interval thixotropy test (UV-3ITT). This rheological method introduces stepwise jumps in the oscillation strain from low to high, followed by a return to low strain, but UV light is optionally turned on during the third interval using the UV capabilities of a photorheometer. This method allows for comparison of viscoelastic recovery during the third interval with and without UV light intervention. By gathering recovery data, two separate analyses are made. First, structural deformation parameters are used to assess changes in recovery that result from high stress environments with and without UV light [28-31]. Next, the mutation number – a ratio of recovered modulus relative to recovery rate – is utilized to make comparative arguments of whether a material's final storage modulus or initial rate of modulus recovery is driving printability [32]. Rheological findings are compared to actual UV-DIW printing studies of highly filled photopolymers, whose print height and quality are assessed. Understanding the structural recovery of these colloidal systems using rheological analyses prior

to additive manufacturing is essential to link theory to practice, reducing experimentation time and decreasing the amount of material required for printing studies, while accelerating material discovery for AM processes [28].

5.3 Materials and Methods

Ebecryl® 230 (E230), a commercially available, UV-curable, aliphatic urethane diacrylate, was supplied by Allnex and used as the polymer matrix. The matrix was filled at various loading levels with glass bubbles (iM30k) supplied by 3M. These glass bubbles have an advertised diameter of 18 μm. To confirm this reported particle diameter, 100 glass bubbles were analyzed using scanning electron microscopy (Figure 5.1), and then sized using ImageJ software. This method confirmed that the average diameter of the particles was 16.3 ± 5.6 μm. Formulations consisted of either 45, 50, 55, 60, or 62.5 vol% glass filler. To promote polymerization during exposure to ultraviolet light, 2.5 wt% of Phenylbis(2,4,6-trimethylbenzoyl)phosphine oxide (BAPO) was also included in each formulation as a photoinitiator. Samples were mixed using a DAC 1200-500 VAC FlackTek Speedmixer. Each formulation was made in 20 gram batches and mixed at 1200 RPM for one minute followed by 2000 RPM for two minutes. The sides of the mixing cup were then scraped and mixed by hand to incorporate any filler that was stuck to the walls of the container. The same mixing procedure was then performed a second time. SEM imaging in Figure S9.3.1 of the supporting information confirms that the glass spheres were not broken during the mixing process.

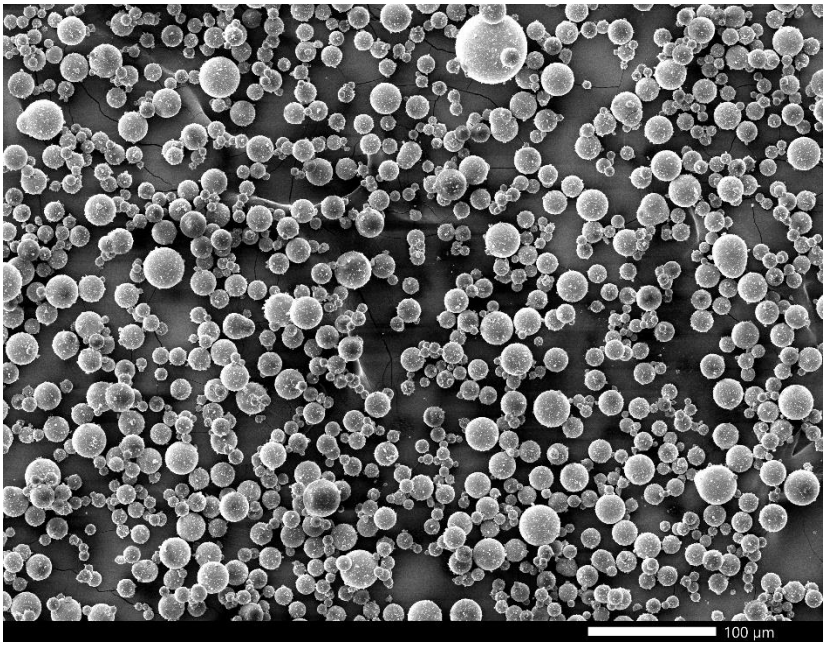

Figure 5.1: Scanning electron microscopy images of the iM30k glass fillers.

5.3.1 Rheology

Torsional rheology was performed on a Discovery HR30 rheometer (TA Instruments, Newcastle, DE, USA) using a 20 mm stainless steel parallel upper plate. A transparent 20 mm glass bottom plate allowed UV light to cure the material during experimentation. The UV light guide accessory in combination with an Excelitas Omnicure S2000 UV mercury lamp (broadband with a 320-500 nm filter) source provided the UV light. The UV intensity was set at 100 mW cm^{-2} and calibrated using a UV-full Silverline Radiometer. All experiments were conducted in oscillation mode since continuous shear measurements suffered from edge fracture and slip. Additionally, modulus data is extremely valuable for these experiments, which can only be gathered in oscillation mode. These tests were conducted at ambient room temperature.

A gap of 0.5 mm was chosen to be representative of the 500 µm bead height during prints. Strain sweeps were conducted at 1 Hz from 0.001% to 10% strain in order to verify the limits of the linear viscoelastic region for each sample. Frequency sweeps were also performed at 0.02%

strain from 0.1-100 rad s^{-1} to determine the degree of shear thinning for each sample. Cure depth measurements using the method outlined by Rau et al. (2022) were performed on the lowest and highest concentration inks to determine the effect of solids loading level on cure depth [33]. These inks were subjected to SAOS (0.02% strain, 1 Hz, 500 μm gap) for 60 seconds without UV light, and then for 180 seconds with UV light enabled. Excess material was then wiped from the rheometer plate, and the top geometry was lowered until an axial force of 5 N was reached. The corresponding height of the top geometry indicated the cure depth of each sample. This process was performed three times each for the 45 and 62.5 vol% inks.

Normally, the three interval thixotropy test tracks structural recovery of a material after large amounts of strain outside the LVR have been applied. The novel test proposed here – the UV-assisted three interval thixotropy test – identifies improvements in structural recovery as a result of UV light intervention after periods of high strain. The test consisted of three successive steps. First, one minute of low strain (0.02%) data were gathered within the LVR to understand the baseline viscoelastic properties of the material – representative of "at rest" behavior of the ink within the barrel of the printer. This period also helped to eliminate any stress history the material might have experienced during sample preparation or loading. Second, one minute of high strain (2%) oscillation outside the LVR was performed to disrupt the interparticle network, characteristic of the high stresses experienced during extrusion. Third, three minutes of low strain (0.02%) data were gathered to track structural recovery, representing the behavior of the ink as it lays on the build bed post-extrusion. At the start of this third step, UV light was optionally turned on to assess changes in structural recovery as a result of the curing process. A frequency of 1 Hz was used with fast sampling enabled, allowing for two data points per second to be obtained.

5.3.2 DIW Printing and Design

Experimental UV-DIW printing was performed on a custom three axis DIW platform (Figure 5.2a). Movement at controlled distance and speed was provided via three Zaber LRT0500 linear stages with 500 mm of travel. A Nordson EFD HPx high pressure extrusion head and a Nordson EFD Ultimus V precision dispenser provided control of extrusion. The pneumatic system controls extrusion via the selective application of air pressure. Increasing air pressure results in increasing flow rate. *In situ* photocuring was achieved through the integration of a Dymax QX4 LED spot-cure system that directs UV light towards the exit of the extrusion nozzle, illustrated in Figure 5.2b. The Dymax PrimeCure heads provide UV irradiation at 385 nm. Lastly, to measure the cross-sectional profile of the printed beads, a Keyence LJ-V7000 laser profilometer was used, shown in Figure 5.2c. Since the laser profilometer was attached to the gantry next to the extruder, transitioning from extrusion to profilometry took less than five seconds.

In experimental printing studies a constant translation speed of 500 mm s^{-1}, a layer height of 0.5 mm, and nozzle diameter of 0.5 mm were used. For inks with various loadings of solids, extrusion pressure was varied to produce homogenous and consistent beads with width equal to the diameter of the nozzle. These pressures were 18, 20, 35, 50, and 70 psi for the 45, 50, 55, 60, and 62.5 vol% inks, respectively. For *in situ* curing, UV intensity was calibrated at 100 mW cm^{-2} during extrusion.

To understand the relationship between filler loading level and part fidelity, a single layer of material was extruded using the DIW printer. Here, we use the term “print height” in reference to the measured height of a single line, or a multi-layer build. “Print resolution” or “print quality” is a qualitative, visual inspection of a printed part. “Print fidelity” refers to both height and quality

as an all-encompassing term. The average height of three individual printed lines was measured at three different time points (immediately after extrusion, 3 minutes after extrusion, and 10 minutes after extrusion), with and without *in situ* UV light. The height of a three 15-layer walls was also measured, with and without UV light, for each concentration.

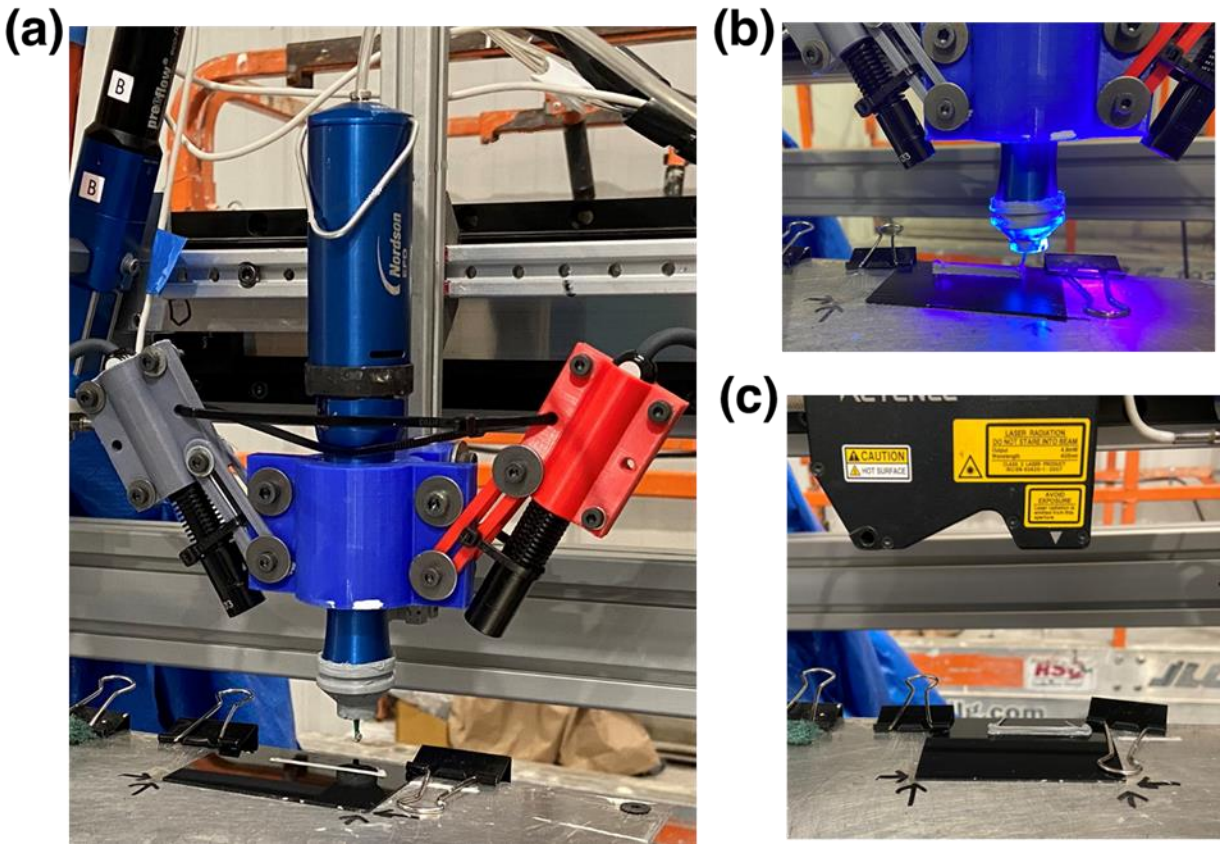

Figure 5.2: (a) Nordson EFD HPx High Pressure Head used to extrude the viscous inks and the Dymax QX4 UV LEDs that provide *in situ* UV curing. UV light is off in the photo. (b) Example of *in situ* UV curing provided by the UV LEDs focused on the ink as it exits the nozzle. (c) Scanning of extruded bead to get its cross-sectional profile using a Keyence LJ-V7000 laser profilometer.

5.4 Results and Discussion

Essential rheological tests (strain and frequency sweeps) were performed to gather information regarding the LVR and degree of shear thinning for uncured samples. These tests also helped to probe the presence of a percolation threshold. Single-layer print heights of inks ranging from 45-62.5 vol% glass were then measured, with and without *in situ* ultraviolet light. To understand structural stability during multi-layer builds, the height of a three 15-layer walls was measured and averaged for each testing condition. The printing results were compared to UV-3ITT findings to determine rheological factors most important to printability.

5.4.1 Strain and Frequency Sweeps of Unreacted Ink

A strain sweep is used to determine the limits of the LVR for unreacted inks. This information is vital for understanding the rheology of the ink before any UV curing process occurs. Figure 5.3 suggests that as the loading level of solids increases, the storage modulus at any given strain also increases. This is expected, since as the volume fraction of solids increases, packing density rises, thus increasing the number of interactions with neighboring particles [9]. This also causes a shortening of the linear viscoelastic region, according to Figure 5.3.

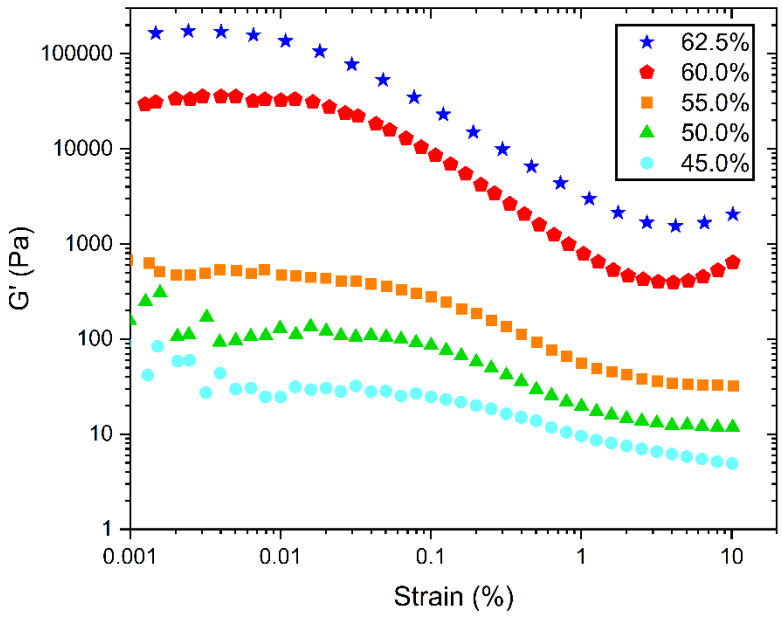

Figure 5.3: Strain sweeps to determine the linear viscoelastic region of each ink. Higher filler concentrations reduce the range of the LVR and increase the modulus at any given strain percentage.

During DIW, it is often desired for inks to possess a yield stress so that the material does not uncontrollably flow through the nozzle. A yield stress is typically present when tan(δ) – the ratio of loss to storage modulus – is below unity. Interestingly, none of the samples possessed a yield stress in the sense that tan(δ) was always greater than 1 within the LVR. Plots of *G'*, *G"*, and tan(δ) as a function of strain can be found in Figures S9.3.2 and S9.3.3 within the supporting information.

Another important feature of highly filled systems is their ability to be shear thinning. That is, at elevated shear rates (i.e. through the nozzle), viscosity will drop which facilitates deposition without the risk of clogging. An effective way to characterize shear thinning is through a power law model in Equation (5.1).

$$\eta = K\dot{\gamma}^{n-1} \tag{5.1}$$

Where η is the viscosity, K is the consistency index, $\dot{\gamma}$ is the shear rate in s^{-1}, and n is the power law index [4]. As the power law index decreases, the degree of shear thinning increases. Measurements of complex viscosity for highly filled systems tend to overestimate the viscosity, and it should be noted that the Cox-Mertz rule does not apply to these systems, but the analysis remains useful when model fitting is desired [12]. Additionally, as discussed in the Experimental section, measurements of viscosity using continuous shear experiments are not favorable because 1) edge fracture/slip is abundant and 2) the cured network from the UV light can be destroyed.

Figure 5.4 illustrates the frequency sweep results for all inks, along with the power law model for each loading level.

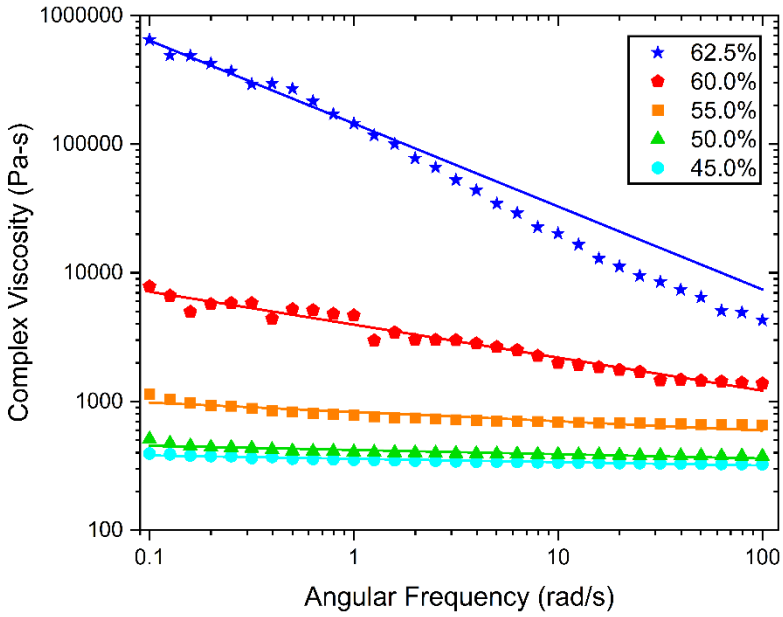

Figure 5.4: Frequency sweeps to identify the degree of shear thinning of each ink. Solid lines indicate power law fitting models.

Nearly Newtonian behavior is observed for loading levels up to 55 vol%. Beyond this level of solids loading, the degree of shear thinning begins to increase drastically. Correlation coefficients for these power law models, along with values of the consistency index and power law index, are presented in Table 5.1.

Table 5.1: Consistency and power law indices for each loading level of solid filler, along with respective correlation coefficients.

Vol% Filler	K	n	r^2
45%	358	0.974	0.93
50%	420	0.967	0.78
55%	830	0.928	0.84

60%	3961	0.744	0.95
62.5%	144912	0.355	0.99

Most notably, changes in the consistency and power law indices are exponential beyond 55 vol% solids content (n=0.928 at 55 vol%, n=0.744 at 60 vol%). The shear thinning capabilities of an ink enable fluidic behavior within the nozzle – where shear stress and shear rate are high. Thus, even materials with large viscosities (60 and 62.5 vol%) can be extruded at sufficiently high shear rates. Furthermore, the percolation threshold can be defined as the limit where zero shear viscosity approaches infinity; from Figure 5.4, there is evidence that filler concentrations beyond 55 vol% may exhibit percolation behavior [34]. When the percolation threshold is attained, a filler network is noticed at low shear rates which contributes to large increases in viscosity [34]. From a DIW standpoint, these low shear rates are representative of "at rest" behavior within the barrel of the print head before extrusion, and on the build bed post-extrusion. While we have not probed extremely low rates to determine whether a Newtonian zero shear plateau is reached, the measurements in Figure 5.4 help us understand that a significant transition in fluid structure is being observed under hydrodynamic stresses. The disruption of this interparticle network can cause sagging and spreading of inks, which is subsequently studied.

5.4.2 Single layer printing and profilometry

For an ink to be printable, a desirable trait is accurate part resolution at a variety of timepoints post-deposition. While low levels of solid loading lessen the likelihood of clogging, the lack of a yield stress may cause the material to flow out of the nozzle uncontrollably. Conversely, highly loaded systems can be made printable through adequate backpressures, but subjection to high levels of shear stress can cause sag over time due to thixotropy/hysteresis [35]. Increasing the concentration further may reduce these effects, but nozzle clogging then becomes a factor [9, 36].

Hence, the rheological requirements for an ink to be printable are often ambiguous. To understand the relationship between hysteresis and filler concentration, single layers of highly loaded inks ranging from 45-62.5 vol% glass were printed and optionally subjected to *in situ* UV light. Figure 5.5a illustrates how rest time post-deposition affects single layer print height when no UV light is utilized, for a variety of concentrations.

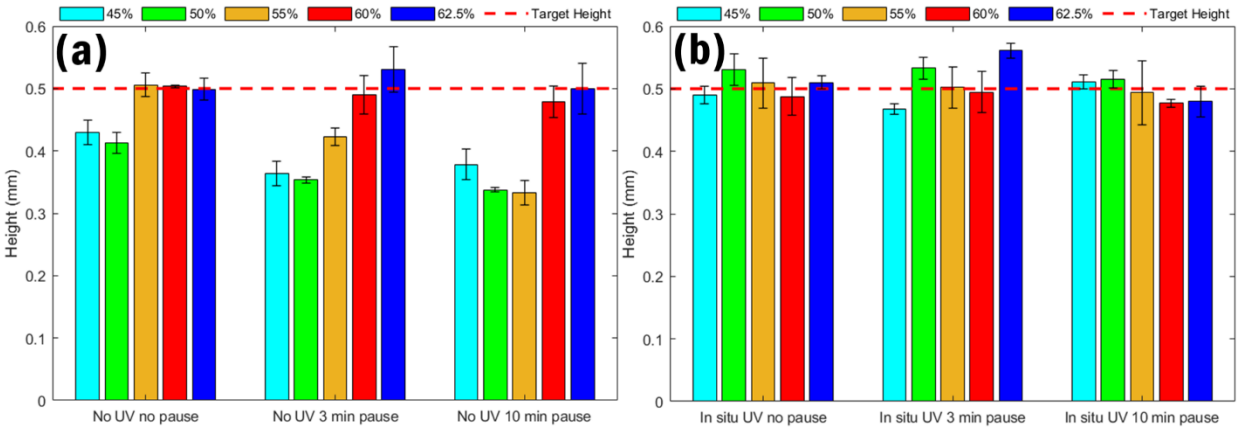

Figure 5.5: Height of a single printed layer at various times post-extrusion (a) without *in situ* UV light and (b) with *in situ* UV light. Error bars indicate standard deviations of the final print height.

Without UV, the 45 and 50 vol% systems show immediate sag once the inks are deposited onto the print bed, and the level of sag appears to worsen with time. Interestingly, the 55 vol% ink has no immediate sag, but after three minutes, the height begins to lower. The height continues to decrease after ten minutes of rest. The 55 vol% ink appears to mark a transition to higher loading levels where sag is no longer apparent over time, supporting the prior argument about the transition in shear thinning behavior at this loading level (Figure 5.4); the 60 and 62.5 vol% have no meaningful sag even after ten minutes of resting on the build bed.

There are a variety of reasons why printed inks spread over time. One reason is that they do not have a sufficient at-rest storage modulus or yield stress, as observed by the strain behavior in the 45 and 50 vol% inks in Figure 5.3 [37]. The high shear region of the nozzle may also distrupt the interparticle network, resulting in time-dependent recovery similar to the 55 vol% ink in Figure 5.5a [30]. To combat these factors, a second printing experiment was conducted by applying *in situ* UV light during prints. The hypothesis was that UV intervention would improve the rate of recovery and final modulus of the extrudate. Height profiles of 45, 50, 55, 60, and 62.5 vol% inks via UV-DIW are illustrated in Figure 5.5b.

With the presence of UV light, the lower loading level inks are able to reach their target bead heights, and the time-dependent sag is no longer apparent. Additionally, the higher loaded inks do not meaningfully deviate from their targeted print heights, suggesting no negative consequences of *in situ* UV light on single layer bead height. This emphasizes that *in situ* UV light can be used to enable 3D printing of lower concentrated inks with improved height retention.

5.4.3 Multi-layer builds

Multi-layer build studies were implemented to understand the influence of UV assisted green strength development to support additional load, and to quantify improvements in print height and part resolution when *in situ* UV light is applied. These 15 layer parts must support the increased weight of subsequent layers, and thus require increased strength and stiffness compared to the single layer study in section 5.4.2 (Figure 5.5). The heights of three individual 15-layer walls, with and without UV intervention, are represented in Figure 5.6. Note that the “ideal height” in Figure 5.6 is a simple calculation showing how tall 15 layers of a 0.5 mm bead would be if each printed line contacted each subsequent layer infinitesimally. Pragmatically, there is some desirable

amount of overlap between layers such that interlayer adhesion helps to build mechanical properties of the final product. However, determination of optimal interlayer contact is outside the scope of this manuscript.

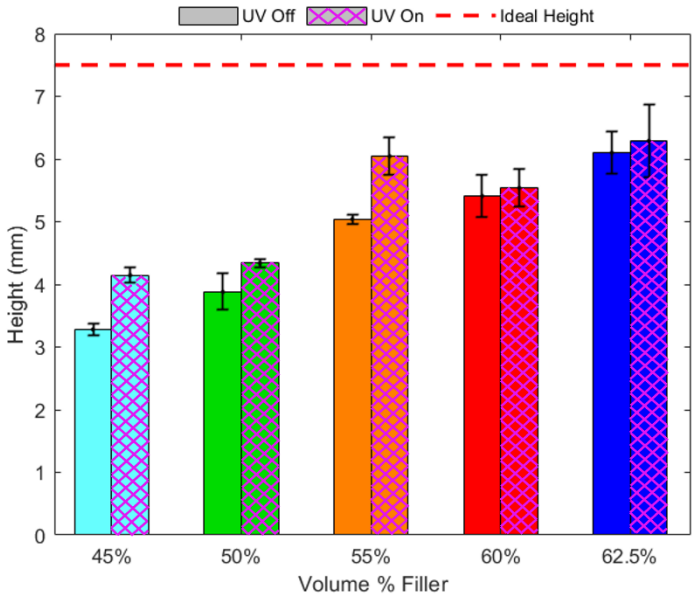

Figure 5.6: Average print heights of three individual 15-layer walls, without and with *in situ* UV, for a range of filler concentrations. Solid bars did not have *in situ* UV light, but cross-hatched bars utilized *in situ* UV light. Error bars indicate standard deviations of the final print height.

Expectedly, there is a positive correlation between the loading level of solids and the final height of the uncured printed part. *In situ* UV light causes a notable increase in print height for the 45-55 vol% samples. Beyond 55 vol%, UV light does not significantly affect print height (as seen by the overlapping error bars of the UV off and UV on samples for the 60 and 62.5 vol% inks). One possible reason for this is that high loading levels of fillers lowers the cure depth, thus inhibiting strength improvements during UV light intervention [38]. Based on work from Rau et. al (2023), large volume fractions of fillers can prevent a material from fully curing unless a post-

processing thermal cure is leveraged via a "dual-cure approach" [39]. However, using the rheological method to measure cure depth published by Rau et al. (2022), we show that loading level has no effect on cure depth in this formulation; after three minutes of exposure to UV light using the photorheometer, the average cure depth of the 45 vol% sample was 230 ± 44 μm, and the cure depth of the 62.5 vol% sample was 226 ± 18 μm, suggesting no significant differences ($p=0.89$) in cure depth between the lowest and highest concentration inks [33]. Instead, this finding indicates an approach to the percolation threshold – when fillers begin to contact their closest neighbors and the rheological properties increase exponentially [40, 41]. Within this regime, the presence of a filler network is driving print height improvements more than the photocurable network. Hence, UV light does not meaningfully contribute to build height, although future work aims to directly relate the degree of cure during UV-DIW to the effects of interlaminar adhesion on mechanical/structural properties of printed parts.

To further support this argument, the maximum packing fraction can be approximated as the bulk density of particles divided by the true density of particles. The maximum packing fraction is advertised as 0.6 according to the iM30k glass bubble technical specifications. Because UV light does not significantly impact multi-layer build heights at 60 vol% and above, this finding provides significant support for the argument that this concentration is representative of a percolation limit [42]. Therefore, the interparticle interactions dominate over the capabilities of a UV cure, and build height is strictly governed by this percolation threshold. This finding is further explored in Figure 5.7, which contains pictures of each 15-layer wall with and without *in situ* UV light for every loading level.

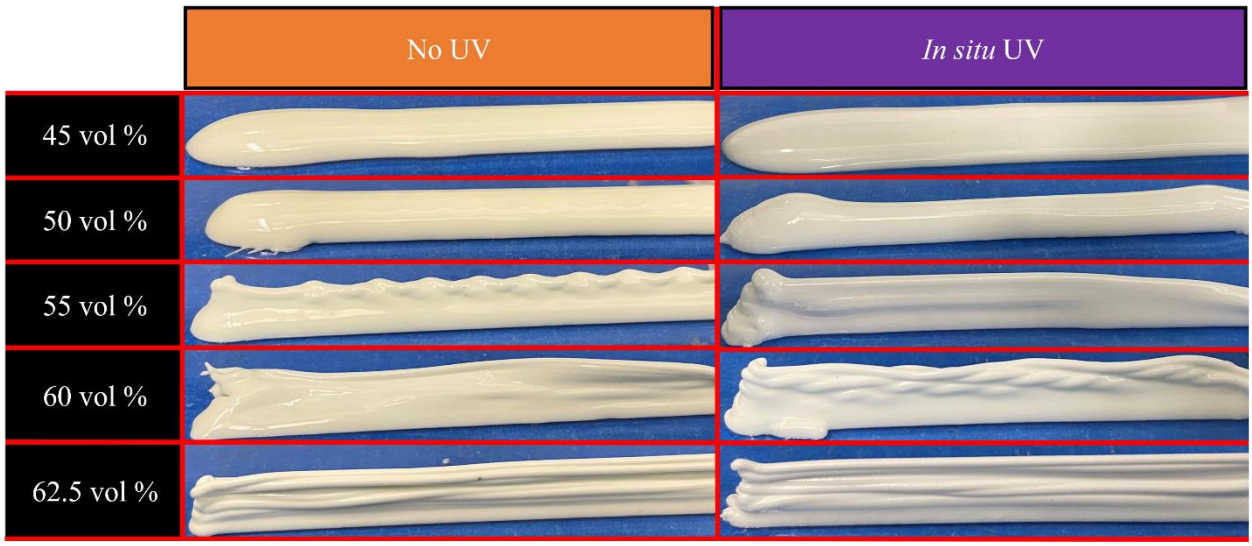

Figure 5.7: Photographs of the 15-layer printed walls at each loading level, with and without UV intervention.

The 45 and 50 vol% samples portray similar print quality with and without UV, and no individual printed beads are visible. This observation correlates with the data in Figure 5.6, which suggests that these low loading levels fail to produce sufficiently high print heights with suitable structural properties. Without UV light at 55 vol%, the printed wall becomes slightly more resolute, but individual layers are not visible and there is "rippling" at the top of the printed part due to sag. When *in situ* UV light is used, the interlayer adhesion increases, and this rippling effect diminishes. Once 60 vol% solids are reached, printed lines can be slightly seen without UV light, and the presence of UV light increases this resolution. This effect is further substantiated for the 62.5 vol% samples. As emphasized in Figures 5.5b and 5.6, the print height of a single lines and multi-layer builds did not improve at 60 and 62.5 vol% with *in situ* UV light, but there is a clear improvement in bead shape retention. Altogether, these print tests suggest that the 60 vol% sample represents the percolation threshold in this formulation, which is further analyzed in section 5.4.4 of this manuscript with a goal of extending broadly to any highly loaded formulation.

5.4.4 UV-3ITT

Recovery of a filled polymer system after subjection to high amounts of stress plays a crucial role in its ability to retain shape post-extrusion. The UV-3ITT addresses this issue by tracking changes in modulus after periods of high strain to determine if structural reformation can be improved by introducing UV light during recovery. An example of this test for the lowest concentration (45 vol %) and highest concentration (62.5 vol %) samples, with and without UV light, is shown in Figure 5.8. Examples of the UV-3ITT experiment for each concentration ink can be found in Figure S9.3.4 of the supporting information.

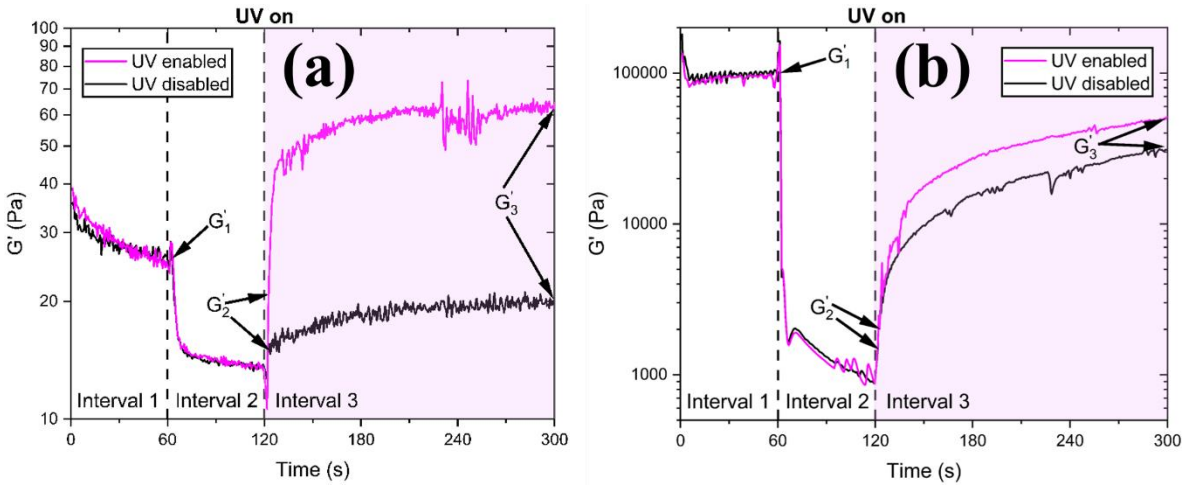

Figure 5.8: Example of a UV-3ITT experiment for a (a) 45 vol% sample and (b) 62.5 vol% sample. UV light is optionally turned on at the start of the third interval, which causes the material to experience rapid growth in *G'* compared to the uncured sample. Note the difference in scale for the modulus between Figures (a) and (b).

Three minutes of UV light exposure was chosen for three main reasons. First, relevant viscoelastic properties plateaued within this timeframe. Low concentration systems experienced minimal changes in *G'* after approximately two minutes, suggesting that structural reformation

due to free radical polymerization finished within this timeframe (see Figure 5.8(a)). High concentration inks, in Figure 5.8(b), still experienced increases in *G'* after 3 minutes, but tan(δ) was no longer time dependent. Hence, solidification due to the UV cure had completed (regardless of whether final cured modulus was reached). Second, because recovery times are extensive, a short three minute exposure to UV light prevented any thermal effects (i.e. thermal curing or viscosity reduction) due to heat from the UV light source. Third, exposure time during the printing process is well below three minutes, so any curing studies beyond this time frame is not within the scope of UV-DIW applications.

Previous studies have developed structural recovery parameters to characterize the degree to which a material deforms after periods of high stress [29]. Other works built upon these findings to create printability maps by introducing variations of the recovery parameters, shown in Equations (5.3) and (5.4) [28].

$$De = \frac{G_1' - G_2'}{G_1'} \times 100 \tag{5.3}$$

$$Rec = \frac{G_3'}{G_1'} \times 100 \tag{5.4}$$

De is the degree of structural deformation, G_1' is the storage modulus at the end of the first interval, and G_2' is the storage modulus at the beginning of the third interval (i.e. one second after the third interval begins). *Rec* is the degree of structural recovery, and G_3' is the recovered storage modulus at the end of the third interval. By plotting *De* as a function of *Rec*, the degree to which a material deforms relative to its reformation capabilities can be analyzed [30]. This plot, for each loading level with and without UV light, is illustrated in Figure 5.9.

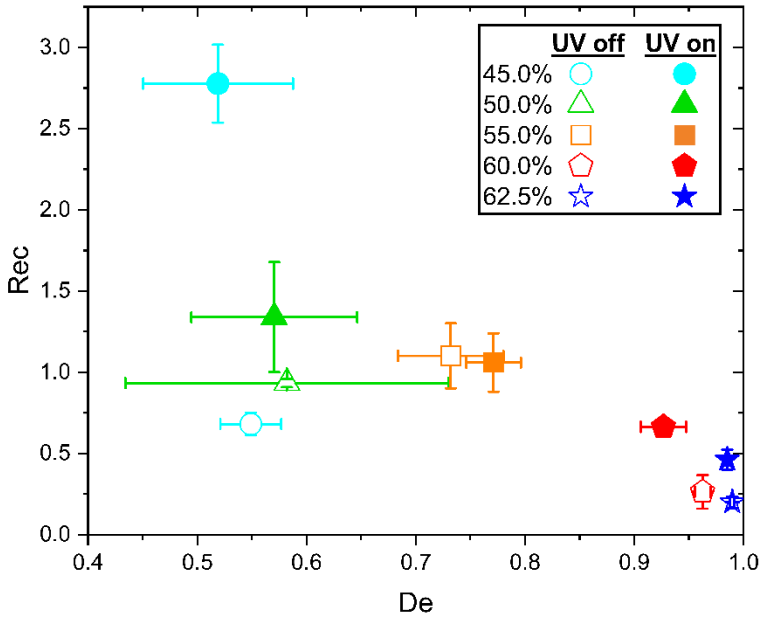

Figure 5.9: Degree of structural recovery as a function of structural deformation. Higher loading levels have greater degrees of structural deformation, but UV light improves structural recovery in most cases. Error bars illustrate standard deviations of each value.

Figure 5.9 provides several rheological insights. First, the structural deformation parameter for the "UV off" samples suggest that as the loading level of solid filler increases, materials experience more structural deformation. This is because an increase in solids density causes more frequent interparticle interactions, thus increasing the potential for flocculates to form [4]. Within the LVR, flocculates increase the modulus, but after experiencing large strains, the flocculates take time to reform, resulting in thixotropy [13]. This same analysis applies to the "UV on" samples. UV light does not have a meaningful effect on *De* for a given solids loading level, since G_2' is gathered just one second after cessation of high strain; the timescale of the curing process (3 minutes) is much longer than the timescale of data collection (less than a second) in this case.

Next, we turn to the structural recovery parameter *Rec*. The most notable finding here is the parabolic shape of the "UV off" samples as the loading level increases. Increasing the

concentration of fillers increases the degree of structural recovery initially, but above 55 vol%, recovery diminishes. This finding is not unique to this system, and has been previously reported in compression set recoverability studies for charcoal-filled natural rubber foams [43]. The result, however, appears counterintuitive because more concentrated systems have better print qualities – especially the 60 and 62.5 vol% inks. A potential reason for this behavior is that below 55 vol%, there are limited, dispersed agglomerates, which are broken up during LAOS measurements. There is also a higher amount of matrix material at these filler concentrations, whose polymer chains are disentangled during this high shear regime. Re-entanglement of polymer chains happens relatively quickly during the recovery stage, but re-agglomeration of the disperse interparticle network is driven by slow, Brownian diffusion. This process can take multiple hours, which is reflected by the low values of *Rec* [24]. Above 55 vol%, strong interparticle interactions drive an initial increase in modulus recovery, but reorganization of the filler network remains incomplete within this timescale because of the large agglomerates which must reform. This process has been previously confirmed for carbon nanotube-filled polycarbonate melts [5]. For any given concentration, if UV light is introduced, *Rec* increases. This is expected since the creation of a photocurable network during the recovery interval increases the modulus of the ink.

The question then becomes: why does print quality continue to improve if recovery appears to reach a peak at 55 vol% for "UV off" samples, but then drop for higher concentration inks? One possible explanation is that even though *Rec* worsens above 55 vol%, there is an adequately large modulus within the LVR that is rapidly recovered for 60 and 62.5 vol% inks. Previous studies have shown that a resting modulus anywhere at or above ~2-10 kPa facilitates high resolution DIW prints [19, 27, 32]. Here, the 60 and 62.5 vol% systems have LVR moduli of approximately 9.6 and 103 kPa respectively, which meets this criterion. By contrast, the LVR modulus of the 55 vol%

system is less than 1 kPa. While this LVR modulus argument is valid for typical DIW prints, it fails to mechanistically explain how changes in viscoelastic properties during UV light exposure can improve printability during UV-DIW. As researchers continue material discovery of DIW inks, it is inevitable that many of these materials will not possess this LVR modulus. To enable printability of these advanced materials, printing parameters and processes must be modified to compensate for the non-optimal rheology of the ink. Thus, it is necessary to deconvolute the effects of thixotropy and UV curing in order to provide a fundamental mechanistic understanding of printability.

The prior discussion introduces an important consideration of whether the rate of modulus recovery or final recovered modulus drives printability. Recovery parameters are useful for determining the relative levels of reformation and deformation, but they are calculated using only the first and final data point in the third interval. This removes any time dependence of the structural recovery process. Instead, another option is to analyze the initial rate of recovery during the first five seconds of the third interval, and then compare it to the final recovered modulus. This method allows for the mutation number to be calculated according to Equation (5.5), which defines a materials stiffness relative to its initial reformation time [32].

$$\lambda_{mutation} = \frac{G_3'}{\frac{dG'}{dt}} \tag{5.5}$$

Here, $\frac{dG'}{dt}$ is the rate of modulus recovery during the first five seconds of the third interval. Using this method, we can compare the rate of recovery to G_3' and determine whether the initial rate of recovery or final modulus is driving print height/print quality improvements. The rate of

modulus recovery as a function of G_3' is depicted in Figure 5.10(a) for each loading level, with and without UV light.

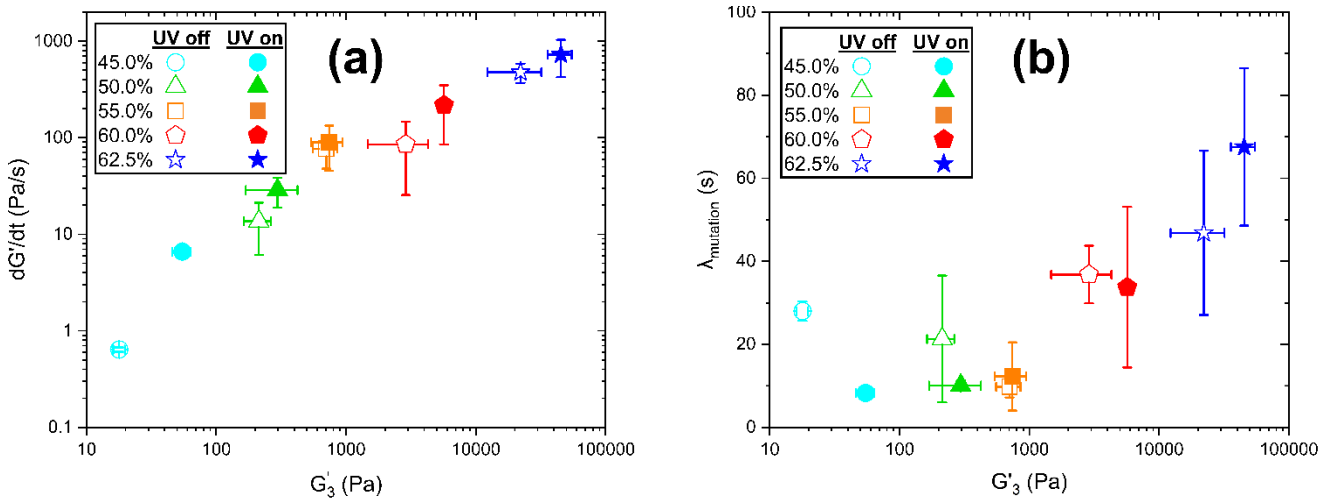

Figure 5.10: (a) Rate of recovery and final modulus improvements as a result of UV curing. (b) Changes in the mutation number by varying the vol% solids and applying UV during recovery. Error bars illustrate the standard deviation of each respective value.

Without UV light, increasing the concentration of fillers raises the recovered modulus and the rate of modulus recovery. When UV light is introduced, both the rate of modulus recovery and the G_3' increase for any given concentration. At 55 vol%, these effects appear to diminish, similar to the peak in *Rec* for the "UV off" samples in Figure 5.9. To better understand the effects UV light has on curing kinetics, $\lambda_{mutation}$ can be plotted as a function of the G_3'. In this sense, $\lambda_{mutation}$ acts as a normalizer by determining whether recovery improvement is driven more by an increase in G_3', or by an increase in the modulus recovery rate. A plot of the mutation number as a function of G_3' is illustrated in Figure 5.10b.

Looking only at the "UV off" samples, increasing the filler concentration from 45 to 55 vol% causes G_3' to rise, but the mutation number lowers. According to Equation (5.5), this implies

that the modulus recovery rate is increasing more quickly, and is thus driving improvements in material recovery. Contrastingly, beyond 55 vol%, the mutation number rises rapidly. This finding suggests that higher concentration inks rely on increases in G_3' to be printable. This corroborates with the previous finding that a minimum modulus of ~2-10 kPa is needed to facilitate high resolution prints. Figures 5.6 and 5.7 also reflect this finding, since higher concentration systems were able to sustain multi-layer builds without buckling or sag – the result of a sufficiently high modulus. Extrusion-based printability models agree with these findings, suggesting that materials with higher moduli possess larger time windows for printability [44].

Next, we turn to the effect that UV light has on the mutation number. At concentrations from 45-55 vol%, UV light causes $\lambda_{mutation}$ to drop. This finding indicates that UV light increases the modulus recovery rate more than the final recovered modulus. From a printability standpoint, these lower concentration systems saw improvements in single layer print height, which was likely driven from this increase in $\frac{dG'}{dt}$. This finding is further substantiated considering that multilayer builds of 45-55 vol% inks lacked a sufficient resting modulus for structural stability, even with UV light intervention. However, the mutation number rapidly increases beyond 55 vol%, such that the mutation number starts to become larger for "UV on" samples than the "UV off" samples. Because $\lambda_{mutation}$ increases when UV light is turned on in this case, increases in G_3' are more significant than increases in $\frac{dG'}{dt}$. This suggests that UV light benefits higher concentration systems by increasing G_3' rather than the rate of recovery. Hence, improvements in multi-layer print resolution for the 60 and 62.5 vol% inks shown in Figure 5.7 are likely driven by increases in final modulus rather than increases modulus recovery rate. Once again, the UV-3ITT suggests that the 55 vol% system is acting as transition region between low loading levels and the percolation

threshold. Beyond this threshold, the final recovered modulus due to interparticle network recovery is driving printability – even when UV light is introduced. This means that as long as the percolation threshold is attained, slumping and spreading of highly filled, multi-layer builds will be prevented purely based on the final recovered modulus of the ink; UV light will simply increase this modulus and improve build quality. But, if the percolation threshold is not reached, resolution and build quality of multiple layers will suffer greatly, and UV light will only partially assist prints via improvements in the modulus recovery rate.

5.5 Conclusion

In this work, we introduce a novel rheological test to assess print height/quality improvements for highly filled photopolymer systems. Printing studies were used to quantify height retention of single-layer prints over time, and then measure the height of multi-layer builds for a range of filler loading levels with optional *in situ* UV intervention. The results indicate that the percolation threshold of a system marked a transition where sag/spreading could be prevented. Below the percolation threshold, sag of single layers was apparent, but UV light prevented any sort of spreading. However, structural stability of multi-layer prints suffered heavily even with UV photocuring. When the percolation threshold was reached at 60 vol% solids, interparticle interactions became a driving force for recoverability, and UV light further improved this recoverability, hence increasing the quality of multi-layer builds.

These findings were realized via UV-3ITT, and the rheological factors most important to printability were determined through structural recovery/deformation parameters and the mutation number. This method illustrated that UV light prevented sag of low-concentration, single-layer printed inks via higher rates of modulus recovery relative to final recovered modulus. However,

because the driving force was the *rate* of recovery, the samples did not possess a large enough *recovered* modulus to enable multi-layer builds – even when *in situ* UV was used. In contrast, inks beyond the percolation threshold facilitated high fidelity prints based on relative increases in the final recovered modulus, rather than increases in modulus recovery rate. When UV light was applied to these samples, there were no changes in build height, but print resolution increased dramatically due to relatively higher levels of the final recovered modulus. Therefore, using a purely rheological method, it is now possible to predict whether print height and/or quality will improve during UV-DIW, thus accelerating the screening process and material discovery for potential future DIW formulations.

5.6 Acknowledgements

Our group would like to acknowledge funding from DEVCOM ARL through cooperative agreement W911NF-20-2-0052. This work was made possible by the use of Virginia Tech's Materials Characterization Facility, which is supported by the Institute for Critical Technology and Applied Science, the Macromolecules Innovation Institute, and the Office of the Vice President for Research and Innovation.

5.7 References

[1] T. Wohlers, T. Gornet, History of additive manufacturing, Wohlers report 24 (2015) 118.
[2] W. Yang, R. Hu, L. Zheng, G. Yan, W. Yan, Fabrication and investigation of 3D-printed gun propellants, Mater. Des. 192 (2020) 108761. https://doi.org/10.1016/j.matdes.2020.108761.
[3] A. M'barki, L. Bocquet, A. Stevenson, Linking rheology and printability for dense and strong ceramics by direct ink writing, Sci. Rep. 7(1) (2017) 1-10. https://doi.org/10.1038/s41598-017-06115-0.
[4] A.V. Shenoy, Rheology of filled polymer systems, Springer Science & Business Media 1999.
[5] S. Richter, M. Saphiannikova, K.W. Stöckelhuber, G. Heinrich, Jamming in filled polymer systems, Macromol. Symp., Wiley Online Library, 2010, pp. 193-201. https://doi.org/10.1002/masy.201050523.
[6] R. Duballet, O. Baverel, J. Dirrenberger, Classification of building systems for concrete 3D printing, Autom. Constr. 83 (2017) 247-258. https://doi.org/10.1016/j.autcon.2017.08.018.

[7] Y. Ju, J. Ha, Y. Song, D. Lee, Revealing the enhanced structural recovery and gelation mechanisms of cation-induced cellulose nanofibrils composite hydrogels, Carbohydr. Polym. 272 (2021) 118515. https://doi.org/10.1016/j.carbpol.2021.118515.
[8] M. Invernizzi, G. Natale, M. Levi, S. Turri, G. Griffini, UV-assisted 3D printing of glass and carbon fiber-reinforced dual-cure polymer composites, Materials 9(7) (2016) 583. https://doi.org/10.3390/ma9070583.
[9] S.S. Chan, R.M. Pennings, L. Edwards, G.V. Franks, 3D printing of clay for decorative architectural applications: Effect of solids volume fraction on rheology and printability, Addit. Manuf. 35 (2020) 101335. https://doi.org/10.1016/j.addma.2020.101335.
[10] N.V. Muravyev, K.A. Monogarov, U. Schaller, I.V. Fomenkov, A.N. Pivkina, Progress in additive manufacturing of energetic materials: Creating the reactive microstructures with high potential of applications, Propellants Explos. Pyrotech. 44(8) (2019) 941-969. https://doi.org/10.1002/prep.201900060.
[11] J.I. Lipton, M. Cutler, F. Nigl, D. Cohen, H. Lipson, Additive manufacturing for the food industry, Trends Food Sci. Technol. 43(1) (2015) 114-123. https://doi.org/10.1016/j.tifs.2015.02.004.
[12] C. Kukla, I. Duretek, J. Gonzalez-Gutierrez, C. Holzer, Rheology of highly filled polymers, Polym. Rheol., IntechOpen2018, pp. 153-173.
[13] J. Mewis, A. Spaull, Rheology of concentrated dispersions, Adv. Colloid Interface Sci. 6(3) (1976) 173-200. https://doi.org/10.1016/0001-8686(76)80008-5.
[14] F. Rubio-Hernández, J. Sánchez-Toro, N. Páez-Flor, Testing shear thinning/thixotropy and shear thickening/antithixotropy relationships in a fumed silica suspension, J. Rheol. 64(4) (2020) 785-797. https://doi.org/10.1122/1.5131852.
[15] B. Nan, F.J. Galindo-Rosales, J.M. Ferreira, 3D printing vertically: Direct ink writing free-standing pillar arrays, Mater. Today 35 (2020) 16-24. https://doi.org/10.1016/j.mattod.2020.01.003.
[16] R. McKenzie, H. Koerner, Enabling direct writing of an epoxy resin with thermo-activated organic thixotropes, Addit. Manuf. 31 (2020) 100905. https://doi.org/10.1016/j.addma.2019.100905.
[17] L. del-Mazo-Barbara, M.-P. Ginebra, Rheological characterisation of ceramic inks for 3D direct ink writing: A review, J. Eur. Ceram. Soc. 41(16) (2021) 18-33. https://doi.org/10.1016/j.jeurceramsoc.2021.08.031.
[18] S.K. Romberg, M.A. Islam, C.J. Hershey, M. DeVinney, C.E. Duty, V. Kunc, B.G. Compton, Linking thermoset ink rheology to the stability of 3D-printed structures, Addit. Manuf. 37 (2021) 101621. https://doi.org/10.1016/j.addma.2020.101621.
[19] D.A. Rau, J. Herzberger, T.E. Long, C.B. Williams, Ultraviolet-assisted direct ink write to additively manufacture all-aromatic polyimides, ACS Appl. Mater. Interfaces 10(41) (2018) 34828-34833. https://doi.org/10.1021/acsami.8b14584.
[20] R. Tu, H.A. Sodano, Additive manufacturing of high-performance vinyl ester resin via direct ink writing with UV-thermal dual curing, Addit. Manuf. 46 (2021) 102180. https://doi.org/10.1016/j.addma.2021.102180.
[21] J.W. Kopatz, J. Unangst, A.W. Cook, L.N. Appelhans, Compositional effects on cure kinetics, mechanical properties and printability of dual-cure epoxy/acrylate resins for DIW additive manufacturing, Addit. Manuf. 46 (2021) 102159. https://doi.org/10.1016/j.addma.2021.102159.

[22] O. Rios, W. Carter, B. Post, P. Lloyd, D. Fenn, C. Kutchko, R. Rock, K. Olson, B. Compton, 3D printing via ambient reactive extrusion, Mater. Today Commun. 15 (2018) 333-336. https://doi.org/10.1016/j.mtcomm.2018.02.031.
[23] S. Jamali, G.H. McKinley, The Mnemosyne number and the rheology of remembrance, J. Rheol. (2022). https://doi.org/10.48550/arXiv.2201.01201.
[24] Y. Chen, Y. Wang, Q. Yang, Y. Liao, B. Zhu, G. Zhao, R. Shen, X. Lu, S. Qu, A novel thixotropic magnesium phosphate-based bioink with excellent printability for application in 3D printing, J. Mater. Chem. B 6(27) (2018) 4502-4513. https://doi.org/10.1039/c8tb01196f.
[25] J.T. Kolawole, R. Combrinck, W.P. Boshoff, Rheo-viscoelastic behaviour of fresh cement-based materials: Cement paste, mortar and concrete, Constr. Build. Mater. 248 (2020) 118667. https://doi.org/10.1016/j.conbuildmat.2020.118667.
[26] H. Hong, H. Jiyong, K.-S. Moon, X. Yan, C.-p. Wong, Rheological properties and screen printability of UV curable conductive ink for flexible and washable E-textiles, J. Mater. Sci. Technol. 67 (2021) 145-155. https://doi.org/10.1016/j.jmst.2020.06.033.
[27] H. Ji, J. Zhao, J. Chen, S. Shimai, J. Zhang, Y. Liu, D. Liu, S. Wang, A novel experimental approach to quantitatively evaluate the printability of inks in 3D printing using two criteria, Addit. Manuf. 55 (2022) 102846. https://doi.org/10.1016/j.addma.2022.102846.
[28] Y. Eom, F. Kim, S.E. Yang, J.S. Son, H.G. Chae, Rheological design of 3D printable all-inorganic inks using BiSbTe-based thermoelectric materials, J. Rheol. 63(2) (2019) 291-304. https://doi.org/10.1122/1.5058078.
[29] M.T. Yilmaz, C. Vatansever, Three interval thixotropy test to determine structural regeneration of a glucomannan based hydrocolloid film at air/water interface: Interfacial, molecular, thermal and surface characterization, Food hydrocolloids 61 (2016) 458-468. https://doi.org/10.1016/j.foodhyd.2016.06.004.
[30] Y. Ju, J. Ha, Y. Song, J.S. Yun, D. Lee, Optimizing the printability and dispersibility of functionalized zirconium oxide/acrylate composites with various nano-to micro-particle ratios, Ceram. Int. 46(17) (2020) 26903-26910. https://doi.org/10.1016/j.ceramint.2020.07.168.
[31] S.H. Ji, D.S. Kim, M.S. Park, D. Lee, J.S. Yun, Development of multicolor 3D-printed 3Y-ZrO2 sintered bodies by optimizing rheological properties of UV-curable high-content ceramic nanocomposites, Mater. Des. 209 (2021) 109981. https://doi.org/10.1016/j.matdes.2021.109981.
[32] A. Corker, H.C.-H. Ng, R.J. Poole, E. García-Tuñón, 3D printing with 2D colloids: Designing rheology protocols to predict 'printability'of soft-materials, Soft Matter 15(6) (2019) 1444-1456. https://doi.org/10.1039/c8sm01936c.
[33] D.A. Rau, J.P. Reynolds, J.S. Bryant, M.J. Bortner, C.B. Williams, A rheological approach for measuring cure depth of filled and unfilled photopolymers at additive manufacturing relevant length scales, Addit. Manuf. 60 (2022) 103207. https://doi.org/10.1016/j.addma.2022.103207.
[34] M.M. Rueda, M.-C. Auscher, R. Fulchiron, T. Perie, G. Martin, P. Sonntag, P. Cassagnau, Rheology and applications of highly filled polymers: A review of current understanding, Prog. Polym. Sci. 66 (2017) 22-53. https://doi.org/10.1016/j.progpolymsci.2016.12.007.
[35] O.S. Toker, S. Karasu, M.T. Yilmaz, S. Karaman, Three interval thixotropy test (3ITT) in food applications: A novel technique to determine structural regeneration of mayonnaise under different shear conditions, Food Res. Int. 70 (2015) 125-133. https://doi.org/10.1016/j.foodres.2015.02.002.
[36] T. Beran, T. Mulholland, F. Henning, N. Rudolph, T.A. Osswald, Nozzle clogging factors during fused filament fabrication of spherical particle filled polymers, Addit. Manuf. 23 (2018) 206-214. https://doi.org/10.1016/j.addma.2018.08.009.

[37] Z. Andrea, C. Paolo, M. Gomes Cynthia, G. Jens, Additive Manufacturing of Ceramics: Issues, Potentialities, and Opportunities, J. Am. Ceram. Soc. 98(7) (2015) 1983-2001. https://doi.org/10.1111/jace.13700.
[38] M.S. McClain, A. Afriat, J.F. Rhoads, I.E. Gunduz, S.F. Son, Development and characterization of a photopolymeric binder for additively manufactured composite solid propellant using vibration assisted printing, Propellants Explos. Pyrotech. 45(6) (2020) 853-863. https://doi.org/10.1002/prep.201900387.
[39] D.A. Rau, J.S. Bryant, J.P. Reynolds, M.J. Bortner, C.B. Williams, A dual-cure approach for the ultraviolet-assisted material extrusion of highly loaded opaque suspensions, Addit. Manuf. 72 (2023) 103616. https://doi.org/10.1016/j.addma.2023.103616.
[40] S.F. Kabir, K. Mathur, A.-F.M. Seyam, A critical review on 3D printed continuous fiber-reinforced composites: History, mechanism, materials and properties, Compos. Struct. 232 (2020) 111476. https://doi.org/10.1016/j.compstruct.2019.111476.
[41] P.J. Carreau, B. Vergnes, Rheological characterization of fiber suspensions and nanocomposites, Rheology of Non-spherical Particle Suspensions, Elsevier2015, pp. 19-58.
[42] A. Poslinski, M. Ryan, R. Gupta, S. Seshadri, F. Frechette, Rheological behavior of filled polymeric systems I. Yield stress and shear-thinning effects, J. Rheol. 32(7) (1988) 703-735. https://doi.org/10.1122/1.549991.
[43] T. Prasopdee, W. Smitthipong, Effect of fillers on the recovery of rubber foam: From theory to applications, Polymers 12(11) (2020) 2745. https://doi.org/10.3390/polym12112745.
[44] C. Duty, C. Ajinjeru, V. Kishore, B. Compton, N. Hmeidat, X. Chen, P. Liu, A.A. Hassen, J. Lindahl, V. Kunc, What makes a material printable? A viscoelastic model for extrusion-based 3D printing of polymers, Journal of Manufacturing Processes 35 (2018) 526-537. https://doi.org/10.1016/j.jmapro.2018.08.008.

Chapter 6

Development of a Microcapillary Rheometer for High Shear Rheology of High Solids Content Polymers

6. Development of a Microcapillary Rheometer for High Shear Rheology of High Solids Content Polymers

John P. Reynolds[1,2,+], Ray Peterson[1,2+], Christopher B. Williams[2,3], Michael J. Bortner[1,2*]

[1]Department of Chemical Engineering, Virginia Tech, Blacksburg, VA 24061

[2]Macromolecules Innovation Institute, Virginia Tech, Blacksburg, VA 24061

[3]Department of Mechanical Engineering, Virginia Tech, Blacksburg, VA 24061

+Co-first authors

*Corresponding author | mbortner@vt.edu | 245 Goodwin Hall, 635 Prices Fork Road, Blacksburg, VA 24061

This chapter is presented as a research article currently in preparation for submission to the *Polymer Testing* Journal.

6.1 Abstract

Capillary rheometry is an effective method for determining the high shear rheological properties of highly filled materials at extrusion relevant conditions. Currently, there are two major challenges faced during capillary rheology studies. First, the capillary rheometer itself is relatively expensive (currently over $100,000) which increases the economic barrier for studies. Second, each trial requires dozens of grams of material which presents difficulties when working with limited sample quantities or potentially hazardous materials. To address these concerns, a downscaled version of the capillary rheometer is introduced here, termed the "microcapillary rheometer." This device can be created in a typical lab space for just a few hundred dollars using common laboratory materials and requires only several grams of sample to operate. To validate the findings of the microcapillary rheometer, the high shear (63-1000 s^{-1}) properties of three different highly filled systems (60 vol% glass microbubbles, 7 vol% fumed silica, and 20 vol% calcium carbonate) are evaluated using both full-scale and microcapillary rheometry. Apparent viscosity profiles generally agree between both methods. Applying the Bagley and Weissenberg-Rabinowitsch corrections further increases agreement between true viscosity profiles. These findings substantiate the use of this microcapillary rheometer for high shear measurements of highly filled systems, which enables researchers to conduct similar studies at a fraction of the cost of full-scale capillary rheometry.

6.2 Introduction

High solids content materials, also called "highly filled" materials, are a class of composites which are relevant to the food [1], cement [2], polymer [3], and ceramics [4] industries among many others. The term highly filled is not unanimously defined across literature, although most systems are considered "high solids content" when a sufficient proportion of solid particulate

fillers is incorporated into a resin, such that the filler content exceeds 50 vol% [5]. While this definition is appropriate for ideal fillers (i.e. an aspect ratio of 1 with minimal surface interactions), it is well documented that the shape of the particle in addition to the particle-matrix/particle-particle surface interactions can significantly decrease this threshold [6]. These interparticle interactions often result from weak surfaces forces such as Van der Waals forces, hydrostatic forces, and interparticle friction, which collectively result in the formation of an interparticle network [7]. Thus, high solids content materials can be more generally described as a composite which has been loaded with such a large volume fraction of solid particulate fillers that the rheological properties due to interparticle network interactions outweigh the viscoelastic properties of the resin in which they are dispersed [6, 8-10].

Characterization of these highly filled materials has become an active field of study for predicting extrusion quality [11], development of clogs during high shear processing [12], and solid-liquid phase separation [13, 14]. Typically, several forms of rheometry are utilized to gather viscoelastic properties relevant to processing. One of the most common types of rheological testing – parallel plate rheometry – places a highly filled material between two plates which can be oscillated or continuously sheared. Although continuous shear rheology enables development of a flow field at (potentially) process relevant shear rates, highly filled composites can exhibit sample loss out the sides of the plates at shear rates exceeding 0.1 s^{-1} [3, 15]. Resultingly, oscillatory measurements are more commonly employed because they enable acquisition of viscoelastic properties without the risk of edge fracture. This form of testing provides modulus data which is essential for understanding structural properties of the interparticle network, but the Cox-Merz rule is often invalid for these high solids content systems (i.e. oscillatory measurements of complex viscosity are often larger compared to steady shear viscosity measurements) [3].

To bridge this gap in knowledge, capillary rheometers are frequently used to gather process-relevant, high shear measurements of shear viscosity for highly filled materials. The capillary rheometer utilizes a load frame attached to a piston which drives material through a capillary die. An inline pressure transducer quantifies the pressure drop across the length of the capillary, and depending on the flow rate and capillary geometry, the apparent shear stress, shear rate, and viscosity can be determined [16]. Because sample loss in the form of edge fracture does not occur as frequently during capillary rheometry compared to torsional rheometry, shear rates on the order of thousands of s^{-1} are achievable [17].

The flow field that is developed at these elevated shear rates contributes towards particle alignment and deagglomeration of flocculates; resultingly, viscosity often decreases due to shear thinning [18]. Several constitutive and empirical equations are available to model these relationships, including the power law model [19], Bingham model [20], Carreau-Yasuda model [21], and Cross model [22]. The use of a given model depends on the presence of several rheological phenomena, including yield stresses, infinite shear viscosities, and zero shear viscosities. Before using these models, it is important that corrections be applied to transform apparent shear viscosities into true viscosities. These corrections stem from errors introduced from funneling the material from a large diameter barrel into a small diameter die, non-Newtonian fluid flow, and wall slip. The Bagley correction accounts for artificial increases in viscosity during the funneling process by adjusting pressure drops attributed to entrance/exit effects during capillary flow [17]. The Weissenberg-Rabinowitsch correction accounts for the non-Newtonian behavior of shear thinning fluids to obtain more accurate measurements of shear rate [23]. Additionally, the contribution of wall slip towards overall fluid flow can be optionally quantified by analyzing apparent shear rates across various length-over-diameter ratios using the Mooney analysis [24].

Wall slip is common for highly filled systems because of particle migration away from the wall [25], which results in a resin-rich region along the wall causing slip [26]. This particle migration can further contribute towards partial clogs [12], complete jamming [26], and liquid phase migration/filtering of the resin [27, 28].

Development of clogs due to jamming or curing within the capillary is notoriously burdensome when cleaning the rheometer, which has prompted development of small scale, disposable capillary rheometers [29]. Several previous studies utilized the controlled strain rate/force capabilities of an Instron Universal Testing Machine to provide constant rates or loads to a low-cost, disposable syringe, which enabled characterization of curing systems [28, 29]. Other products have been introduced which line the barrel of a full-scale capillary rheometer, thus preventing any sort of curing to the machine itself [30]. While these methods enable rapid testing of complex, high solids content materials, the cost of the capillary rheometer or Instron itself is still substantial. In fact, smaller versions of the capillary rheometer are often only suitable for low viscosity, dilute suspensions [25, 31, 32]. To this end, there is clear value in developing a downscaled, low-cost version of the capillary rheometer that can characterize high shear properties of high solids content systems, while exploiting small material quantities. This small-scale product is particularly necessary for rapidly characterizing expensive or potentially hazardous materials which are dangerous in larger quantities required for full scale capillary rheometry.

In this work, a microcapillary rheometer is developed which can accurately and precisely measure high shear viscosity profiles of highly filled materials. The microcapillary design is described in detail such that it can be recreated in a standard laboratory setting. Three different highly filled materials, consisting of a polydimethylsiloxane (PDMS) resin and either glass

microbubbles, fumed silica, or calcium carbonate are then tested using the device, and the results are compared to a large, full-scale capillary rheometer which validates the microcapillary data. The Bagley and Weissenberg-Rabinowitsch corrections are applied to all sets of data to explicitly account for entrance/exit effects and non-Newtonian flow regimes, respectively. Torsional rheology is also performed to further validate the presence of a highly filled system. These findings enable researchers to increase the economics of characterization by accelerating capillary rheometry experiments while limiting the amount of material necessary for data acquisition.

6.3 Materials and Methods

The PDMS resin used for all samples was obtained from Gelest, which has a viscosity of 5 Pa-s. iM30k glass bubbles were supplied by 3M with an average diameter of 19 μm. CABO-O-SIL TS-720 Fumed silica (FS) was obtained from Cabot, which is a spherical, nano-scale powder. This material can also form larger nano- and micro-scale agglomerates. Calcium carbonate ($CaCO_3$) was obtained from SkySpring Nanomaterials, which is cubic in geometry and has an advertised particle diameter of 15-40 nm. Scanning electron microscopy (SEM) images of these fillers are presented in Figure 6.1. Three separate highly filled inks were created using 60 vol% iM30k glass bubbles, 20 vol% $CaCO_3$, and 7 vol% FS. These loading levels were specifically chosen because they elicit yield stress behavior, possess a defined linear viscoelastic region, and/or attain loading levels representative of the percolation threshold [33].

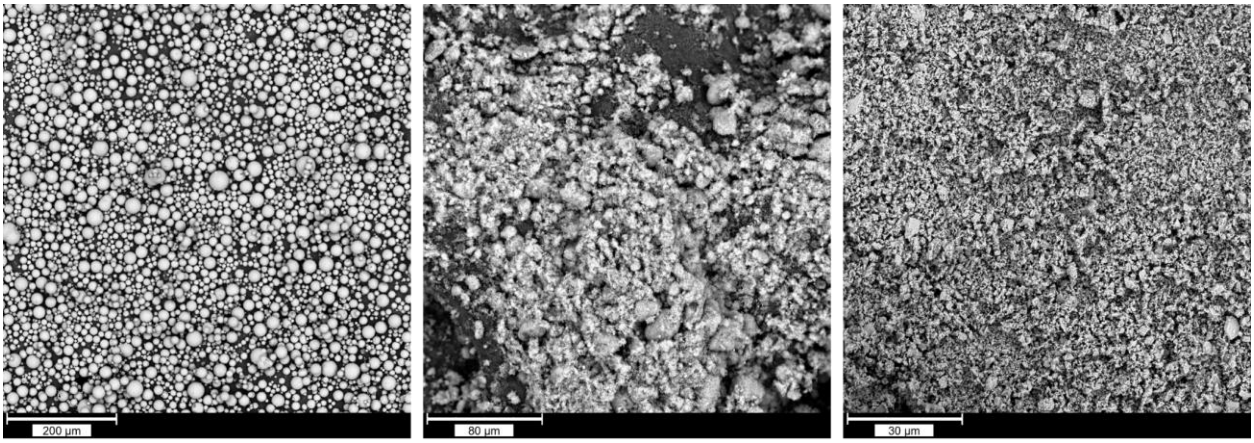

Figure 6.1: SEM images of (left) iM30k glass, (middle) fumed silica, and (right) calcium carbonate. Note the difference in scale for each SEM image.

Torsional rheometry is performed on a TA Instruments ARES-G2 rheometer using 25 mm stainless steel parallel plates and a 1 mm gap. Strain sweeps are conducted from 0.01-10% strain at a frequency of 1 Hz. Frequency sweeps are conducted from 0.1-100 rad s^{-1} at 0.05% strain which is within the linear viscoelastic region (LVR) of all samples. All experiments are performed at room temperature and ambient conditions.

A custom microcapillary rheometer was developed to rapidly test the high shear characteristics of high solids content inks using limited sample quantities. The system consists of a rate controlled linear syringe pump (New Era Pump Systems NE-8000 High Pressure Programmable Syringe Pump) equipped with a load cell (TE Connectivity FX293X-100A-0010-L) attached to the sliding block. As the sliding block and force sensor push the syringe plunger, the material is extruded, and the force sensor measures pumping force. The load cell interfaces with a microcontroller (Arduino UNO), which communicates with a computer running a LabVIEW program. The LabVIEW program uses the geometric parameters of the setup (barrel diameter, capillary length, and capillary diameter) to calculate syringe pump rates. These

geometric parameters and pump rates define the apparent shear rates (Equation (6.1)). During testing, the LabVIEW program reads the load cell force and calculates the pressure (Equation (6.2)), apparent shear stress (Equation (6.3)), and apparent viscosity (Equation (6.4)). These data points are logged every 0.1 seconds into a spreadsheet.

$$\dot{\gamma}_{app} = \frac{32Q}{\pi D^3} \tag{6.1}$$

$$\Delta P = \frac{4F}{\pi D^2} \tag{6.2}$$

$$\tau_{app} = \frac{\Delta P D}{4L} \tag{6.3}$$

$$\eta_{app} = \frac{\dot{\gamma}_{app}}{\tau_{app}} \tag{6.4}$$

Here, $\dot{\gamma}_{app}$ is the apparent shear rate, Q is the volumetric flow rate, D is the capillary diameter, ΔP is the pressure drop along the capillary, F is the force read by the force sensor, τ_{app} is the apparent shear stress, L is the capillary length, and η_{app} is the apparent viscosity. For this setup, the capillary length and diameter are equivalent to the syringe nozzle length and diameter, respectively. The syringe used is a custom stainless-steel syringe with a commercial polytetrafluoroethylene (PTFE) tipped plunger (Hamilton 10cc Gastight Glass Syringe), shown in Figure 6.2. The syringe barrel has an inner diameter approximately 10.27 mm. The syringe is adapted to a Luer-lock fitting where a commercial blunt-tipped Luer-lock syringe can be attached to act as the capillary die. The Luer-lock fitting enables quick swapping of tips of different lengths or diameters.

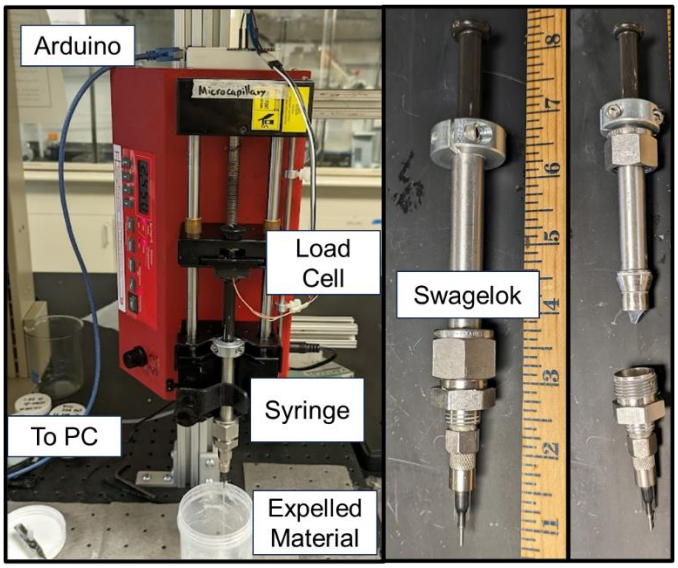

Figure 6.2: Labeled schematics of the (left) microcapillary rheometer and (right) custom fabricated high-pressure syringe showing the assembled and opened state.

To account for the contribution of friction between the syringe plunger and barrel wall, a frictional force correction is applied. The microcapillary system is run at relevant shear rates with an empty syringe, which measures the load associated with these frictional forces. The measured load is generally similar across the range of apparent shear rates (approximately 15 N). Some variations at the beginning and end of the test are observed (see Figure S9.4.1), which is attributed to slight variation in the machined inner diameter of the tubing, especially as the plunger approaches the end of the barrel. To avoid error from these sections of the tubing, testing within the initial or final 0.5 in of the tube does not occur.

To conduct an experiment, the length and diameter of the syringe tip are first measured using calipers. To load the test material, the Swagelok fitting is opened, and the barrel is loaded with material while withdrawing the plunger. This gradual filling process eliminates the formation of air bubbles. After loading, the Swagelok fitting is retightened, and the syringe tip is firmly screwed onto the syringe. The syringe is clamped onto the syringe pump, and the sliding

block/force sensor is set just above the plunger without touching it. The LabVIEW program is then run, which calibrates and zeroes the load cell. This zeroing process averages the zero-load signal from the load cell for 10 seconds while the sliding block moves towards the plunger.

After zeroing, the program automatically adjusts the pump speed to achieve the desired shear rates. Each shear rate is tested until a stable load is measured, which is defined as a load variation of less than 2 N using a minimum stability band of five seconds. To determine the apparent shear stress at each shear rate, the mode of the force readings within the stability band is calculated. Three different lengths of 16-gauge syringe tips (nominally 0.25 in, 0.5 in, and 1 in) are utilized. These syringe tip geometries correspond to L/D ratios of 26.6, 15.5, and 9.8, respectively. Logarithmically spaced shear rate sweeps are performed in triplicate for microcapillary rheometer experiments. The apparent shear rates used are 63, 100, 158, 251, 398, 631, and 1000 s^{-1}.

An Instron SR-20 Capillary Rheometer (full-scale capillary rheometer) is used to validate the findings of the microcapillary rheometer. In order to mimic the experimental setup/design of the microcapillary rheometer, the inline pressure transducer is not used, and instead pressures are calculated using the overhead force transducer and specific capillary die geometry. Three different capillary geometries (L/D = 30/1, L/D = 20/1, and L/D = 10/1) are utilized. The capillary and barrel diameters are fixed at 1 mm and 15 mm, respectively. Logarithmically spaced shear rate sweeps are performed in triplicate for full-scale capillary rheometer measurements. The apparent shear rates used are 63, 100, 158, 251, 398, 631, and 1000 s^{-1}.

6.4 Results and Discussion

6.4.1 Torsional Rheometry

Torsional rheometry was performed on each sample to verify the presence of key rheological properties relevant to highly filled systems. Strain sweeps in Figure 6.3 illustrate a range of viscoelastic phenomena, which depend on the filler type. The 60 vol% iM30k glass filled ink has a relatively large linear viscoelastic region (LVR) and does not possess a yield stress – defined as the crossover over point of *G'* and *G"*. These findings are due to the micro-scale nature of the glass bubbles, which form weak interparticle networks compared to nano-scale fillers. However, this loading level is well documented to encompass the percolation threshold (where fillers contact each of their closest neighboring particles), which verifies this inks status as a highly filled system. The 7 vol% FS ink has substantially larger values of *G'* at every given strain, and a clear crossover point at 2% strain. This increased elasticity and the presence of a crossover point are attributed to the nano-scale nature of fumed silica, which forms a stronger interparticle network compared to micro-scale particles. The 20 vol% $CaCO_3$ ink has even larger values of *G'* at every strain, and the LVR shortens substantially such that the crossover point occurs at 0.05% strain. These findings are attributed to the cubic geometry of $CaCO_3$, which increases the frequency of surface interactions, thus increasing the stiffness of the material while limiting the amount of strain necessary for deformation to occur [10].

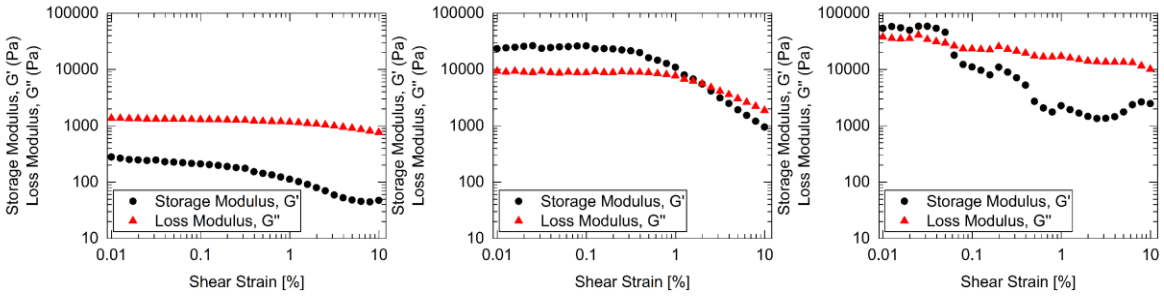

Figure 6.3: Strain sweeps of (left) 60 vol% iM30k glass bubbles, (middle) 7 vol% FS, and (right) 20 vol% $CaCO_3$.

Frequency sweeps illustrated in Figure 6.4 were also performed to identify the degree of shear thinning during oscillatory measurements and validate the presence of a highly filled system; large degrees of shear thinning often indicate the presence of a percolated network, which is a key component of highly filled systems [10, 33]. The 60 vol% iM30k, 7 vol% FS, and 20 vol% $CaCO_3$ systems have degrees of shear thinning n equivalent to 0.85, 0.22, and 0.19, respectively when fitted to a power law model (see Equation (6.5)). This finding highlights that rapid reductions in viscosity are present for stronger interparticle networks due to more pronounced deagglomeration processes during periods of high shear/high frequency. While the Cox-Merz rule does not hold for highly filled systems due large contributions of elasticity via particle inclusion, these findings provide evidence that each material studied here fulfills the requirements of a highly filled system. Thus, these experiments provide useful metrics for validating the findings of the microcapillary rheometer.

$$\eta = K\dot{\gamma}^{n-1} \tag{6.5}$$

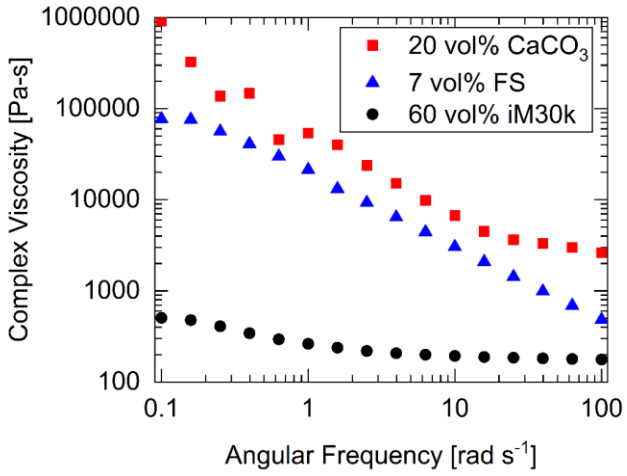

Figure 6.4: Frequency sweeps of each highly filled ink illustrating shear thinning behavior.

6.4.2 Capillary Rheometry

Shear rate sweeps were performed for both the full-scale capillary rheometer and the microcapillary rheometer. Equivalent shear rates were used for both experiments, with the goal of validating the microcapillary rheometer findings by comparing viscosity values to the full-scale capillary rheometer. It is well documented that corrections must be applied to transform the apparent viscosity values into true viscosity values. This is accomplished by applying a Bagley correction and a Weissenberg-Rabinowitsch correction.

The Bagley correction adjusts the apparent shear stresses by accounting for the entrance/exit pressure effects when funneling material from the barrel into the capillary die, while the Weissenberg-Rabinowitsch correction adjusts the apparent shear rates by accounting for non-Newtonian flow patterns [3]. Bagley corrections are obtained by performing a linear regression on pressure drops as a function of L/D for a range of shear rates, such that the y-intercept represents the entrance/exit contributions of the pressure drop $\Delta P_{effects}$. Weissenberg-Rabinowitsch corrections can then be applied by applying a linear regression to the log-log plot of true shear stress τ_{true} as a function of apparent shear rate, which provides a degree of shear thinning n used to calculate the true shear rate $\dot{\gamma}_{true}$. Application of the Bagley correction is presented in Equation (6.6) and Figure 6.5, and the Weissenberg-Rabinowitsch correction is shown in in Equation (6.7). Using these corrections, it is possible to calculate the true viscosity η_{true} using equation (6.8) [34].

$$\tau_{true} = \frac{\left(\Delta P_{app} - \Delta P_{effects}\right)D}{4L} \tag{6.6}$$

$$\dot{\gamma}_{true} = \frac{\dot{\gamma}_{app}(3n+1)}{4n} \tag{6.7}$$

$$\dot{\eta}_{true} = \frac{\tau_{true}}{\dot{\gamma}_{true}} \tag{6.8}$$

Bagley plots, presented in Figure 6.5, illustrate similarities in pressure drop associated with each highly filled composite sample. In general, there is good agreement between the value of pressure drop associated with each shear rate at a given *L*/*D* ratio. The iM30k glass samples during microcapillary measurements deviate from the full-scale data at particularly high *L*/*D* ratios and shear rates because of the large forces required for extrusion, which approached the limits of the force sensor. However, these findings still suggest that Bagley corrections can be accurately and precisely applied to highly filled inks using both full-scale and microcapillary rheometry.

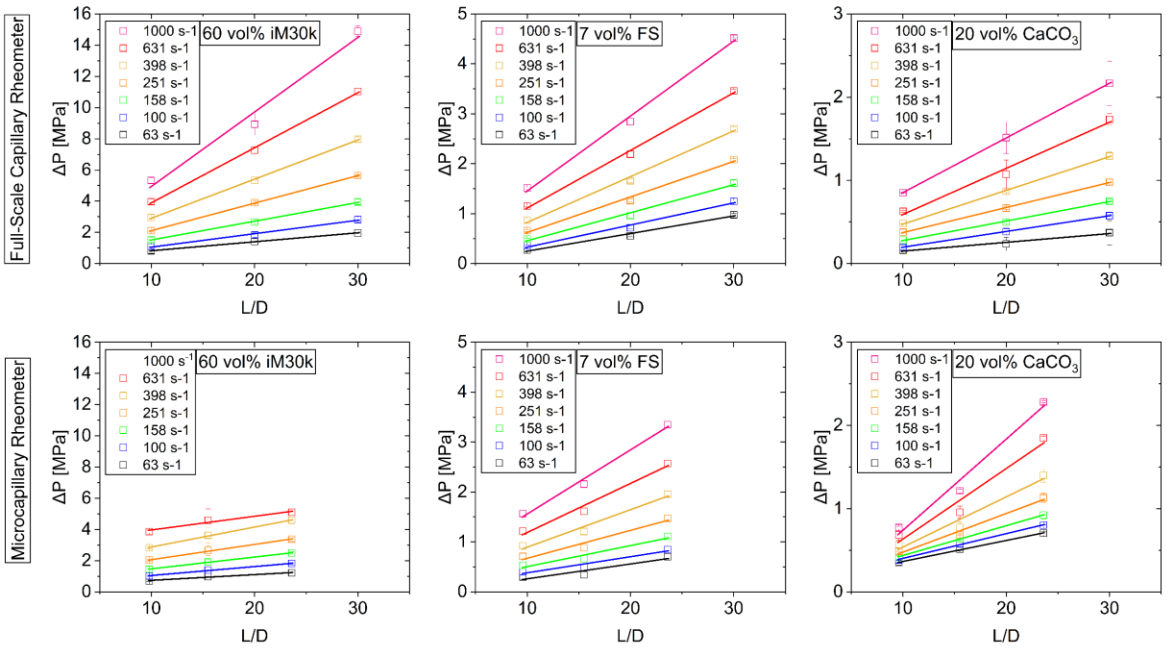

Figure 6.5: Bagley plots for 60 vol% iM30k, 7 vol% FS, and 20 vol% $CaCO_3$ using the full-scale capillary rheometry and microcapillary rheometry. Error bars illustrate standard deviations. Note that 1000 s^{-1} could not be gathered for the 60 vol% iM30k system using the microcapillary rheometer due to force sensor limitations.

Weissenberg-Rabinowitsch corrections, presented in Figure 6.6, are also remarkably similar when comparing testing methods for a given material. In all cases, the non-Newtonian flow of these highly filled systems causes shear thinning, which causes the true shear rate to exceed the apparent shear rate. Thus, the findings in Figure 6.6 suggest that true shear rates associated with non-Newtonian flow can be effectively probed using both the microcapillary rheometer and full-scale capillary rheometer.

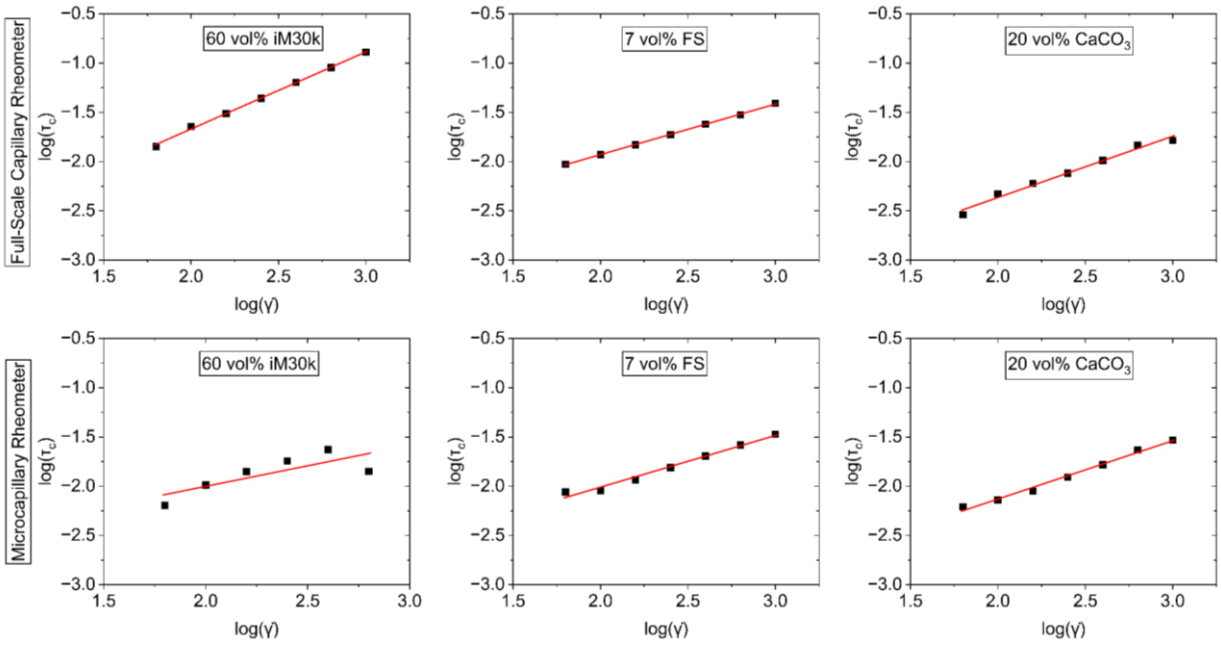

Figure 6.6: Weissenberg-Rabinowitsch plots for 60 vol% iM30k, 7 vol% FS, and 20 vol% $CaCO_3$ using the full-scale capillary rheometry and microcapillary rheometry.

As a result of these corrections, the apparent and true viscosity of each material can be compared using both the full-scale and microcapillary rheometer as presented in Figure 6.7. The 60 vol% iM30k glass-filled ink has nearly identical values of apparent viscosity when using either the full-scale or microcapillary rheometer. When corrections are applied, the corrected microcapillary viscosity decreases more than expected. This finding is attributed to the force limit

being reached during testing using the microcapillary setup, which resulted in pressure drops being lower than expected, thus influencing the Bagley correction and causing an artificially lower value of true viscosity. The 7 vol% FS samples also have extremely similar values of apparent viscosity using both methods, and there is still great agreement after corrections are applied. The apparent viscosity of the $CaCO_3$ differs between full-scale and microcapillary rheometry, but application of the Bagley and Weissenberg-Rabinowitsch corrections improves agreement between the true viscosity values.

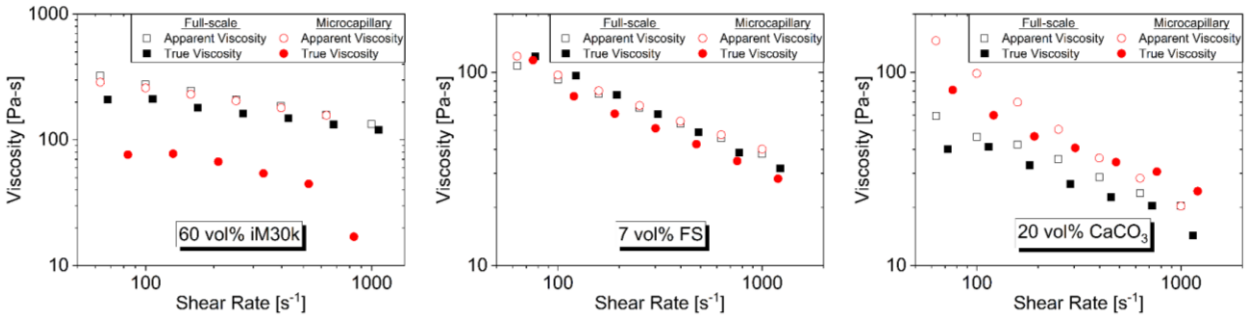

Figure 6.7: Uncorrected and corrected viscosity profiles of 60 vol% iM30k, 7 vol% FS, and 20 vol% $CaCO_3$ using both full-scale and microcapillary rheometry.

The degree of shear thinning can also be compared between methods and materials, with and without Bagley/Weissenberg-Rabinowitsch corrections, as illustrated in Figure 6.8. The degree of shear thinning *n* is determined by applying the power law model (see Equation (6.5)) to the data in Figure 6.7. According to Figure 6.8, the degree of shear thinning for the 60 vol% iM30k ink is generally independent of testing device and correction status. Therefore, whether the data are corrected or uncorrected, both the full-scale and microcapillary rheometer provide similar fits to the power law model. In other cases, such as the 7 vol% FS system, there is an initial agreement between the degrees of shear thinning when the data are uncorrected. When corrections are applied, the degree of shear thinning decreases for both full-scale and microcapillary rheometry, yet the

corrected values still agree. In more extreme cases such as the 20 vol% $CaCO_3$ system, there are large disagreements in the degree of shear thinning when the data are uncorrected. Applying corrections for this material results in nearly equivalent values of shear thinning between testing methods. As a result, there is clear evidence that this microcapillary rheometer device can determine the viscosity of high solids content systems both accurately and precisely, and these findings are validated through the use of a full-scale capillary rheometer.

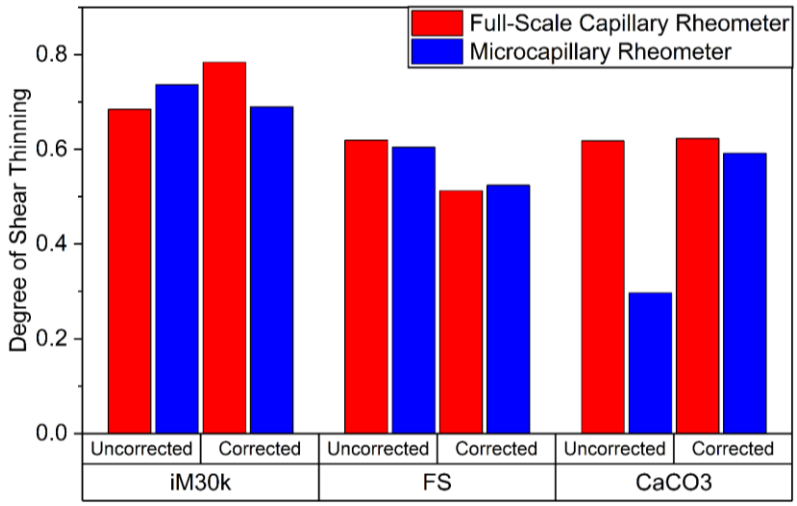

Figure 6.8: Comparison of the degree of shear thinning between full-scale and microcapillary rheometry using a power law model.

6.5 Conclusion

When building process-structure-property relationships among high solids content materials for extrusion processes, it is necessary to characterize high shear viscoelastic properties at process-relevant rates. By evaluating the overall resistance flow (i.e. viscosity), it is possible to tailor process parameters relevant to extrusion performance. The microcapillary rheometer device introduced here reduces the economic burden of high shear characterization by minimizing sample requirements, while substantially lowering the cost of the testing device itself. Currently, full-scale

capillary rheometers require dozens of grams of material and cost well over $100,000, while the microcapillary rheometer costs hundreds of dollars to create and requires only several grams of material.

Torsional rheology studies were used to validate the presence of a highly filled system for three separate samples (60 vol% iM30k glass bubbles, 7 vol% fumed silica, and 20 vol% $CaCO_3$). The combination of yield stress formation, presence of a percolated network, and large degrees of shear thinning all substantiated the high solids content nature of each sample. As a result, capillary rheology studies could be subsequently used to determine the effect of high shear environments on viscosity profiles.

To establish the reliability of data gathered using the microcapillary rheometer, high shear viscosity profiles of these high solids content materials were analyzed using both full-scale and microcapillary rheometry at shear rates covering three orders of magnitude (63-1000 s^{-1}). Both the Bagley and Weissenberg-Rabinowitsch corrections were successfully applied to the data, which resulted in improved agreement between 1) nominal values of true viscosity and 2) the degree of shear thinning. These findings validate the use of this microcapillary device for high shear studies of highly filled inks, and we have demonstrated that these high shear properties can be evaluated with equivalent accuracy and precision regardless of testing method. As a result, this device has the potential to lower the economic barrier for researchers to conduct high shear capillary rheology studies on high solids content materials, while minimizing health risks when working with hazardous materials by substantially reducing sample quantity requirements.

6.6 Acknowledgements

The authors would like to acknowledge funding from DEVCOM ARL through cooperative agreement W911NF-20-2-0052.

6.7 References

[1] C. Feng, M. Zhang, B. Bhandari, Materials properties of printable edible inks and printing parameters optimization during 3D printing: A review, Critical reviews in food science and nutrition 59(19) (2019) 3074-3081. https://doi.org/10.1080/10408398.2018.1481823.
[2] A.M. Mostafa, A. Yahia, New approach to assess build-up of cement-based suspensions, Cem. Concr. Res. 85 (2016) 174-182. https://doi.org/10.1016/j.cemconres.2016.03.005.
[3] C. Kukla, I. Duretek, J. Gonzalez-Gutierrez, C. Holzer, Rheology of highly filled polymers, Polym. Rheol., IntechOpen2018, pp. 153-173.
[4] S.S. Chan, R.M. Pennings, L. Edwards, G.V. Franks, 3D printing of clay for decorative architectural applications: Effect of solids volume fraction on rheology and printability, Addit. Manuf. 35 (2020) 101335. https://doi.org/10.1016/j.addma.2020.101335.
[5] I. Campbell, A. Marnot, M. Ketcham, C. Travis, B. Brettmann, Direct ink write 3D printing of high solids loading bimodal distributions of particles, AlChE J. 67(12) (2021) e17412. https://doi.org/10.1002/aic.17412.
[6] M. Bek, J. Gonzalez-Gutierrez, C. Kukla, K. Pušnik Črešnar, B. Maroh, L. Slemenik Perše, Rheological behaviour of highly filled materials for injection moulding and additive manufacturing: effect of particle material and loading, Applied Sciences 10(22) (2020) 7993. https://doi.org/10.3390/app10227993.
[7] J. Guo, T. Chai, Y. Liu, J. Cui, H. Ma, S. Jing, L. Zhong, S. Qin, G. Wang, X. Ren, Kinetic research on the curing reaction of hydroxyl-terminated polybutadiene based polyurethane binder system via FT-IR measurements, Coatings 8(5) (2018) 175. https://doi.org/10.3390/coatings8050175.
[8] A.V. Shenoy, Rheology of filled polymer systems, 1 ed., Springer Science & Business Media 1999.
[9] J. Walberer, A.J. McHugh, The linear viscoelastic behavior of highly filled polydimethylsiloxane measured in shear and compression, J. Rheol. 45(1) (2001) 187-201. https://doi.org/10.1122/1.1332386.
[10] M.M. Rueda, M.-C. Auscher, R. Fulchiron, T. Perie, G. Martin, P. Sonntag, P. Cassagnau, Rheology and applications of highly filled polymers: A review of current understanding, Prog. Polym. Sci. 66 (2017) 22-53. https://doi.org/10.1016/j.progpolymsci.2016.12.007 0079-6700.
[11] A. Corker, H.C.-H. Ng, R.J. Poole, E. García-Tuñón, 3D printing with 2D colloids: Designing rheology protocols to predict 'printability'of soft-materials, Soft Matter 15(6) (2019) 1444-1456. https://doi.org/10.1039/c8sm01936c.
[12] T. Beran, T. Mulholland, F. Henning, N. Rudolph, T.A. Osswald, Nozzle clogging factors during fused filament fabrication of spherical particle filled polymers, Addit. Manuf. 23 (2018) 206-214. https://doi.org/10.1016/j.addma.2018.08.009.
[13] M. Patel, S. Blackburn, D.I. Wilson, Modelling of paste ram extrusion subject to liquid phase migration and wall friction, Chem. Eng. Sci. 172 (2017) 487-502. https://doi.org/10.1016/j.ces.2017.07.001.

[14] S. Rough, J. Bridgwater, D. Wilson, Effects of liquid phase migration on extrusion of microcrystalline cellulose pastes, Int. J. Pharm. 204(1-2) (2000) 117-126. https://doi.org/10.1016/S0378-5173(00)00478-6.
[15] C.E. Cipriani, Y. Shu, E.B. Pentzer, C.C. Benjamin, Viscoelastic and thixotropic characterization of paraffin/photopolymer composites for extrusion-based printing, Physics of Fluids 34(9) (2022) 093106. https://doi.org/10.3390/sym13101767.
[16] U. Yilmazer, D.M. Kalyon, Slip effects in capillary and parallel disk torsional flows of highly filled suspensions, J. Rheol. 33(8) (1989) 1197-1212. https://doi.org/10.1122/1.550049.
[17] P. Filip, B. Hausnerova, E. Hnatkova, Continuous rheological description of highly filled polymer melts for material extrusion, Applied Materials Today 20 (2020) 100754. https://doi.org/10.1016/j.apmt.2020.100754.
[18] J. Mewis, A. Spaull, Rheology of concentrated dispersions, Adv. Colloid Interface Sci. 6(3) (1976) 173-200. https://doi.org/10.1016/0001-8686(76)80008-5.
[19] V.A. Krauss, E.N. Pires, A.N. Klein, M.C. Fredel, Rheological properties of alumina injection feedstocks, Materials Research 8 (2005) 187-189. https://doi.org/10.1590/S1516-14392005000200018.
[20] D. Bonn, M.M. Denn, L. Berthier, T. Divoux, S. Manneville, Yield stress materials in soft condensed matter, Reviews of Modern Physics 89(3) (2017) 035005. https://doi.org/10.1103/revmodphys.89.035005.
[21] S.B. Balani, F. Chabert, V. Nassiet, A. Cantarel, Influence of printing parameters on the stability of deposited beads in fused filament fabrication of poly (lactic) acid, Addit. Manuf. 25 (2019) 112-121. https://doi.org/10.1016/j.addma.2018.10.012.
[22] T. Osswald, N. Rudolph, Polymer rheology, Carl Hanser, München (2015).
[23] S.A. Gulmus, U. Yilmazer, Effect of volume fraction and particle size on wall slip in flow of polymeric suspensions, J. Appl. Polym. Sci. 98(1) (2005) 439-448. https://doi.org/10.1002/app.21928.
[24] M. Mooney, Explicit formulas for slip and fluidity, Journal of Rheology (1929-1932) 2(2) (1931) 210-222. https://doi.org/10.1122/1.2116364.
[25] K. Kang, L.J. Lee, K.W. Koelling, High shear microfluidics and its application in rheological measurement, Exp. Fluids 38 (2005) 222-232. https://doi.org/10.1007/s00348-004-0901-4.
[26] D.M. Kalyon, S. Aktaş, Factors affecting the rheology and processability of highly filled suspensions, Annual review of chemical and biomolecular engineering 5 (2014) 229-254. https://doi.org/10.1146/annurev-chembioeng-060713-040211.
[27] T. Kaully, A. Siegmann, D. Shacham, Rheology of highly filled natural CaCO3 composites. I. Effects of solid loading and particle size distribution on capillary rheometry, Polym. Compos. 28(4) (2007) 512-523. https://doi.org/10.1002/pc.20308.
[28] J. Zhou, E. Sancaktar, Stable and unstable capillary flows of highly-filled epoxy/nickel suspensions, J. Adhes. Sci. Technol. 22(8-9) (2008) 983-1002. https://doi.org/10.1163/156856108X305426.
[29] M. Rides, C.R. Allen, G.D. Sims, Rheological characterisation of a highly filled curing system using a disposable extrusion rheometer, Polym. Test. 29(2) (2010) 164-169. https://doi.org/10.1016/j.polymertesting.2009.10.006.
[30] M. Shaw, S. Burkert, D. Sundstrom, Capillary viscometer for use with crosslinking polymer melts, American Institute of Physics, 1978. https://doi.org/10.1063/1.1135317.

[31] M. Zou, S. Cai, Z. Zhao, L. Chen, Y. Zhao, X. Fan, S. Chen, A novel polydimethylsiloxane microfluidic viscometer fabricated using microwire-molding, Rev. Sci. Instrum. 86(10) (2015) 104302. https://doi.org/10.1063/1.4933388.
[32] S.D. Hudson, P. Sarangapani, J.A. Pathak, K.B. Migler, A microliter capillary rheometer for characterization of protein solutions, J. Pharm. Sci. 104(2) (2015) 678-685. https://doi.org/10.1002/jps.24201.
[33] J.P. Reynolds, D.A. Rau, C.B. Williams, M.J. Bortner, A rheological method to predict printability of high solids content inks via ultraviolet-assisted material extrusion, Addit. Manuf. (2023) 103753.
[34] F.A. Morrison, Understanding rheology, Oxford university press New York 2001.

7. Conclusions and Recommendations for Future Work

7.1 Conclusions

1) While useful in many settings relevant to material extrusion, TPU has been shown to present complications when processing at elevated temperatures – often in excess of 200 °C. The similarity between the processing and degradation temperatures results in the buildup of solid particulate matter within the extrusion line, which has the potential to cause complete clogs, thus shutting down the process. The tendency for this solid-like buildup to occur depends not only on the manufacturer of TPU, but the specific lot of TPU from a given manufacturer. A unique approach to quantifying the degree of solidification was proposed, which tracked changes in the loss tangent at extrusion relevant residence times and temperatures. The worst performing lots of TPU were shown to have marked increases in the rate of solidification compared to better performing lots. This correlation was substantiated through a series of spectroscopic, calorimetric, and dissolution experiments. While FTIR and ^{1}H-NMR could not differentiate chemical differences between lots of TPU, they confirmed the presence of a (PTMO-BDO-MDI) polyurethane. DSC experiments confirmed that the presence of large endothermic peaks correlated strongly with poorer extrusion performance – likely a result of hard segment aggregation at processing temperatures. The extrusion line clogs are attributed to this aggregation. Further solubility studies confirmed that strong intermolecular forces in the form of hard segment aggregation caused the TPU to solidify over process-relevant timescales. The inability of THF or DMF to dissolve the poorest performing lot of TPU once again suggests that physical crosslinking, as opposed to covalent crosslinking, was the major caused of solidification. This was confirmed through subsequent successful dissolution in

DMF+LiBr, which effectively probed for strong intermolecular interactions. Dynamic light scattering studies provided evidence that the worst performing lots of TPU also possessed smaller hydrodynamic radii prior to high-temperature exposure. Smaller hydrodynamic radii are often associated with more branched polymer architectures, resulting from side reactions (e.g. biuret and allophanate linkages). These branched structures were presumably incorporated during the synthetic process, which predisposed the TPU to poor processability within the extruder. Resultingly, we have outlined a series of experiments that require limited sample quantities and can quickly predict processability concerns prior to extrusion, thus preventing potential extrusion line shutdowns while preserving valuable economic resources.

2) The thermosetting reaction between hydroxyl-terminated polybutadiene and isophorone diisocyanate, when uncatalyzed, takes multiple days or weeks to fully react depending on the temperature. Through a chemorheological analysis, we have shown that this reaction displays a unique, discontinuous cure pattern in an uncatalyzed setting which is attributed to thermal diffusion limitations of the monourethane prior to stage 2 of the reaction. Model fitting techniques such as the Kamal-Sourour autocatalytic model and Wynne-Jones-Eyring-Evans transition state model confirm the novel cure profile and highlight the autocatalytic nature of the reaction. When compared to cure studies using temperature controlled FTIR, it becomes apparent that spectroscopic techniques elicit early onset reaction rates about an order of magnitude larger than chemorheological results. However, when the data was truncated after the initial “stage 1” reaction (i.e. monourethane formation), chemorheology and spectroscopy results align. This finding highlights the ability of FTIR to screen more effectively for early, low molecular weight growth reactions

compared to chemorheology alone. Hence, the autocatalytic models likely capture mostly diurethane reaction progress during chemorheology. These findings highlight the advantages and shortcomings of each technique; while FTIR directly measures reactivity through isocyanate conversion, it can be costly to cure these materials onto transparent KBr plates, which currently cost hundreds of dollars per experiment. By contrast, chemorheology can be performed using disposable plates which are a fraction of the cost, although the molecular weight growth must be large enough to correlate with increases in viscoelastic properties. Hence, we have provided an accelerated method using small samples quantities to predict the cure progression of a slow reaction polyurethane, which has not been previously performed for the timescales presented here, and validated these findings through spectroscopic protocols.

3) The interparticle network disruption that occurs within the nozzle of an extrusion print head can cause highly filled inks to sag over time post-deposition, resulting in decreased build heights and build quality. To combat this issue, UV light can be actively shined onto the nozzle, which actively cures the ink *in-situ* resulting in bead shape retention. For highly filled inks below the percolation threshold (in this case, 60 vol%), UV light enabled single layer lines to reach their build heights. For inks above the percolation threshold, the presence of a strong interparticle network did not require such intervention since the printed lines can sustain their structure post-deposition. However, during multilayer builds, inks below the percolation threshold sagged and buckled due to the weight of subsequent layers, resulting in subpar build heights. The presence of UV light increased this height significantly. For multilayer builds of inks at the percolation threshold and above, UV light did not result in increased print heights; instead, UV light benefitted these high solids

content materials by increasing the quality/resolution of the printed parts. The novel rheological test proposed here – the UV-assisted three interval thixotropy test (UV-3ITT) – applied stepwise changes in strain, such that it mimicked the extrusion process. By optionally turning on UV light in the third interval (i.e. the recovery interval) using the capabilities of a photorheometer, improvements in viscoelastic recovery due to UV light post-deformation were quantified. Results highlighted that low vol% inks benefited from UV light due to increases in the rate of modulus recovery. In contrast, high solids content inks above the percolation threshold saw relatively higher increases in the recovered modulus. This finding highlights the ability for inks above the percolation threshold to withstand the weight of subsequent layers purely on the basis of a strong interparticle network and sufficient linear viscoelastic region modulus, such that UV light only provides improvements in build quality – not height. Thus, we have introduced a novel rheological method that can adequately assess the printability of high solids content inks for UV-DIW by exploiting small sample quantities using an accelerated characterization protocol.

4) High shear characterization of reactive, highly filled materials is notoriously burdensome when utilizing a traditional, full-scale capillary rheometer due to large sample requirements, cleaning challenges, economic burden, and the possibility of curing samples within the rheometer. The microcapillary rheometer device introduced here addresses these concerns by downscaling the instrument using common pieces of laboratory equipment at a fraction of the cost of a full-scale rheometer. Results illustrated the accuracy and precision of the microcapillary rheometer compared to the full-scale rheometer, such that corrections (Bagley and Weissenberg-Rabinowitsch corrections) could be successfully applied, enabling calculation of true shear viscosity. These findings were validated for three

different high solids content materials (60 vol% iM30k glass microbubble, 7 vol% fumed silica, and 20 vol% $CaCO_3$) which differed in particle shape, size, and concentration. As a result of this study, there is clear evidence that high solids content materials are able to be rapidly characterized using minimal sample quantities under high shear environments without the risks associated with clogging a full-scale capillary rheometer, which significantly improves efficiency when working with limited sample quantities of novel, reactive, and/or potentially hazardous materials.

7.2 Scientific Contributions

1) Introduced a unique rheological protocol to rapidly screen for potential extrusion line clogs of thermoplastic polyurethane batches using small sample quantities by analyzing the complex viscosity and loss tangent profiles at process-relevant temperatures. Short-term chemorheological protocols in the context of predicting degradation reactions have not been previously utilized, but researchers are now able to prevent a total shutdown of extrusion lines due to these side reactions.
2) Validated the presence of physical crosslinking during melt extrusion of thermoplastic polyurethane (i.e. hard segment aggregation) through a combination of viscoelastic, spectroscopic, calorimetric, solubility, and light scattering experiments, which was attributed to the proximity of the processing temperature to the degradation temperature. The culmination of these analytical techniques provides a novel understanding of degradation kinetics as well as root causes of TPU solidification.
3) Provided evidence that discontinuous cure profiles form during uncatalyzed synthesis of hydroxyl-terminated polybutadiene and isophorone diisocyanate, which is attributed to slow, thermal diffusion of the intermediate monourethane product. This phenomenon can

be effectively probed using chemorheological techniques and has been previously undiscovered. The analysis provided in this work can be generalized to any single- or multi-stage reactive system and is not limited to slow-reacting polyurethanes.

4) Elucidated the advantages and drawbacks of chemorheology and spectroscopy in terms of economics and accuracy when modeling/predicting multi-day thermosetting reactions. The effects of pathlength and flow field development explicitly revealed how these direct/indirect measurements of isocyanate conversion differed depending on conversion progress. The disagreement between conversion profiles for $\alpha_{NCO} < 50\%$ was largely attributed to limited MW growth during early stages of the reaction, causing chemorheological measurements to underestimate conversion, which is a novel insight for this field of research.
5) Created a novel rheological method termed the "UV-assisted three interval thixotropy test" which provides a fundamental, mechanistic understanding of printability during UV-DIW by quantifying the contributions of UV-induced crosslinking towards improvements in print height or print quality. A rheological protocol specifically representative of the UV-DIW AM process has not been developed until this point.
6) Identified a novel use of the mutation number by deconvoluting the effects of the final recovered modulus and rate of modulus recovery after periods of high strain, which is representative of DIW extrusion. The use of the mutation number enables researchers to identify the limits of free radical polymerization when improving print height retention, while also allowing the percolation threshold to be calculated.
7) Developed an affordable, downscaled version of the capillary rheometer which exploits small sample quantities while enabling high shear measurements of extremely viscous,

high solids content systems. This product substantially reduces the upfront cost of performing capillary rheometry, while facilitating rapid characterization of HF materials using only a few grams of material compared to the hundreds of grams required for full-scale capillary rheometry. This device specifically enables characterization of novel materials which might only be available in limited quantities, and allows printability maps to be created based on various geometric criteria (e.g. nozzle geometry, contraction ratio, solids loading level). These maps facilitate prediction of extrudability for any generalizable system appropriate for DIW.

8) Validated the true shear viscosity profiles of the microcapillary rheometer by providing a holistic comparison to the full-scale capillary rheometer. This finding provides evidence that capillary corrections such as the Bagley and Weissenberg-Rabinowitsch can be applied to the novel device with comparable accuracy and precision to a machine which currently costs nearly 100 times more to purchase. Several novel metrics to assess the accuracy of the microcapillary rheometer were also introduced, such as 1) comparisons of viscosity profiles before and after applying corrections, and 2) changes in the degree of shear thinning depending on material selection, device choice, and correction status.

7.3 Recommendations for Future Work

1) While methods have been developed to identify the cause and timescale associated with solid white particulate buildup during TPU extrusion, it is still necessary to identify the chemical composition of this material. This can be accomplished through a combination of TGA-IR, TGA-Mass spectrometry, and long term chemorheology. Additionally, there are early results suggesting that NMR can probe for differences in lot-dependent block lengths of the TPU chains, which positively correlate with solidification. This provides

the opportunity to develop rapid screening protocols which utilize spectrometry/NMR in addition to rheological analyses.

2) Further validation of the diffusion-controlled regime during HTPB+IPDI synthesis can be achieved by studying other aliphatic, asymmetric diisocyanates. However, aside from IPDI, these varieties of diisocyanates are uncommon, which grants the opportunity for synthetic discovery of chemically similar materials.
3) It is plausible that the diffusion-controlled regime can also be validated further by reacting a high MW ($\eta \approx 10{,}000$ Pa-s) monoisocyanate with HTPB across the 60-80 °C temperature range. If the plateau regions described in Chapter 4 are also present for this experimental setup, there would be clear evidence that thermal diffusion drives the sluggish reactivity during primary isocyanate conversion.
4) Mechanical testing (e.g. tensile testing) of partially reacted HTPB+IPDI materials at intermittent timescales would enable a working curve to be built which directly relates time and temperature to structural properties. As a result, the operating conditions of the thermal post-processing step during reactive extrusion could be tailored and predicted. This work would require several multi-day cures to occur at differing time lengths, such that the material is removed from the rheometer and placed into a tensile testing device or dynamic mechanical analyzer for (potentially) destructive characterization.
5) The novel UV-3ITT protocol introduced in Chapter 5 can predict printability of highly filled materials for UV-DIW extrusion processes, which is vital for understanding the dose-dependence effects of UV light on printability. This idea should also be extended to thermal energy dose dependence for reactive extrusion; currently, there is a lack of research identifying the amount of thermal energy required to build structural stability.

This is partially due to a lack of control over thermal dosing. Therefore, using a controlled heating method (e.g. printing in a heated oven or *in-situ* microwave curing), it is possible to apply the UV-3ITT analysis – specifically the mutation number analysis – to thermally curing systems for DIW additive manufacturing.

6) The height retention of UV-DIW prints can be effectively probed using the UV-3ITT method, but it neglects structural integrity via mechanical testing. A possible future endeavor is to identify the relationship between UV light dose and interlaminar adhesion strength. Multiple methods to quantify these findings are available, including a Trouser Tear Method (ASTM D1938), a 3-point Bend Short Beam Shear Test (ASTM D2344), or a variety of lap shear standards which effectively probe for differences in adhesive vs. cohesive failure (ASTM D1002).
7) The microcapillary rheometer has proven to be as accurate and precise as a full-scale capillary rheometer, at a fraction of the price of production. The studies presented in Chapter 6 can be extended to study the viscosity dependence of an ink at various concentrations, which would verify the device's ability to discern not just between materials, but between filler concentrations of a *given* material. For materials that exceed the current load cell's capabilities (e.g. 10 vol% fumed silica which behaves as a stiff solid), larger load cells which require amplification are an opportunity for future research and overall design improvement. This research would expand the material discovery capabilities of the microcapillary rheometer.
8) There are numerous other parameters which can be tailored during microcapillary rheometer measurements. For certain processes, such as injection molding, factors including the contraction ratio (barrel diameter relative to capillary die diameter) can

significantly impact performance. This idea can be extended to a Mooney analysis which quantifies wall slip using various diameter capillary dies. Because of the Luer-lock design, commercially available or machined capillary dies can be bought/constructed relatively easily to accomplish these goals.

9) For all extrusion related experiments, the presence of liquid phase migration (LPM) must be carefully considered, especially when working with HF inks that contain low-viscosity resins. The static zones in the corners of DIW nozzles contribute greatly to this migration progress. It is possible to calculate the degree of LPM by extruding under various conditions (e.g. print speeds, layer heights, and nozzle geometries using different materials), and then analyzing the solids content of the ink both 1) on the build bed and 2) in the barrel using thermogravimetric analysis. These experiments would confirm the presence of LPM and enable researchers to predict conditions that contribute to the building of static zones.

8. Publications

8.1 Peer Reviewed Publications

1. **John P. Reynolds**, Daniel A. Rau, Christopher B. Williams, Michael J. Bortner, "A rheological method to predict printability of high solids content inks via ultraviolet-assisted material extrusion", *Additive Manufacturing*, 103753 (2023).
2. Daniel A. Rau, Jackson S. Bryant, **John P. Reynolds**, Michael J. Bortner, Christopher B. Williams, "A dual-cure approach for the ultraviolet-assisted material extrusion of highly loaded opaque suspensions", *Additive Manufacturing*, 72, 103616 (2023).

3. J. Meier, **J.P. Reynolds**, S. Whalen, J. Patel, M.J. Bortner, and G. Young, "Improved Hybrid Rocket Performance by Additively Manufactured Gel-Infused Solid Fuels", *Journal of Propulsion and Power*, 1-9 (2022).
4. D.A. Rau, **J.P. Reynolds**, J.S. Bryant, M.J. Bortner, and C.B. Williams, "A Rheological Approach for Measuring Cure Depth of Filled and Unfilled Photopolymers at Additive Manufacturing Relevant Length Scales", *Additive Manufacturing*, 103207 (2022).

8.2 Manuscripts Currently Under Peer Review

1. **John P. Reynolds**, John Unterhalter, Mathieu Francoeur, Michael J. Bortner, Bart Raeymaekers, "Viscosity of monodisperse and polydisperse mixtures of photopolymer and rigid spheres for manufacturing of engineered composite materials using vat polymerization." *Under peer review in Advanced Engineering Materials.*
2. **John P. Reynolds**, Tiffany Thompson, John J. la Scala, Cailean Q. Pritchard, Michael D. Schulz, Michael J. Bortner, "Chemorheological Kinetic Modeling of Uncatalyzed Hydroxyl-Terminated Polybutadiene and Isophorone Diisocyanate." *Under peer review in Macromolecular Materials and Engineering.*

8.3 Manuscripts in Preparation for Peer Review

1. **John P. Reynolds,** Ray Peterson, Jackson S. Bryant, Michael J. Bortner, Christopher B. Williams, "Development of a Microcapillary Rheometer for High Shear Rheology of High Solids Content Polymers." *In preparation for submission to Polymer Testing.*
2. **John P. Reynolds**, James Brown, Timothy E. Long, Michael J. Bortner, "Characterization methods to predict extrusion performance in thermoplastic polyurethane batches." *In preparation for submission to Polymer Degradation and Stability.*

8.4 Conference Presentations

1. **John P. Reynolds**, Daniel A. Rau, Christopher B. Williams, Michael J. Bortner, "A rheological method to predict printability of high solids content inks via ultraviolet-assisted material extrusion", **Macromolecules Innovation Institute Technical Conference**, Blacksburg, VA, 10/04/2023. Poster.
2. **John P. Reynolds**, Daniel A. Rau, Christopher B. Williams, Michael J. Bortner, "A novel rheological method to predict printability of high solids content inks via ultraviolet-assisted material extrusion", **Chemical Engineering Graduate Student Association Symposium**, Blacksburg, VA, 04/13/2023. Oral presentation.
3. **John P. Reynolds**, Daniel A. Rau, Christopher B. Williams, Michael J. Bortner, "A novel rheological approach to assess printability improvements for UV-assisted direct ink write processes", **46th Annual Meeting of the Adhesion Society**, Orlando, FL, 02/20/2023. Oral presentation.
4. **John P. Reynolds**, Tiffany Thompson, Michael D. Schulz, Michael J. Bortner, "Chemorheological Analysis of Slow Reacting Polyurethanes", **Society of Plastics Engineers Annual Technical Conference**, Charlotte, NC, 06/13/2022. Oral presentation.
5. **John P. Reynolds**, Tiffany Thompson, Michael D. Schulz, Michael J. Bortner, "Chemorheological Kinetic Modeling of Uncatalyzed Hydroxyl-Terminated Polybutadiene and Isophorone Diisocyanate", **Chemical Engineering Graduate Student Association Symposium**, Blacksburg, VA, 03/29/2022. Oral presentation.
6. **John P. Reynolds**, Tiffany Thompson, Michael D. Schulz, Michael J. Bortner, "Chemorheological Kinetic Modeling of Uncatalyzed Hydroxyl-Terminated

Polybutadiene and Isophorone Diisocyanate", **Macromolecules Innovation Institute Technical Conference**, Blacksburg, VA, 02/15/2022. Poster.

7. **John P. Reynolds**, Daniel A. Rau, Jackson S. Bryant, Christopher B. Williams, Michael J. Bortner, "Mitigation of Hysteresis in High Solids Content Polymers Using Photorheometry", **American Institute of Chemical Engineers Annual Meeting**, Boston, MA, 11/07/2021. Oral presentation.
8. **John P. Reynolds**, Jackson S. Bryant, Daniel A. Rau, Saeid Biria, Michael J. Bortner, "Characterization of High Solids Content Materials for Additive Manufacturing via Rotational Rheometry", **National Graduate Research Polymer Conference**, Virtual, 7/29/2021. Poster.
9. **John P. Reynolds**, Michael J. Bortner, "Characterization of High Solids Content Materials for Additive Manufacturing" **Society of Plastics Engineers Annual Technical Conference**, Virtual, 04/19/2021. Poster.
10. **John P. Reynolds**, Michael J. Bortner, "Characterization of high solids content materials for additive manufacturing via rotational rheometry" **American Chemical Society Annual Meeting**, Virtual, 04/06/2021. Poster.

9. Appendix A – Supplementary Information

9.1 Supplementary Information: Chapter 3

The stress on a sample within the rheometer is either stored as elastic energy, or dissipated through viscous forces, as illustrated in Equations (S9.1.1) and (S9.1.2), respectively [1].

$$G' = \frac{\tau_0}{\gamma_0}\cos(\delta) \tag{S9.1.1}$$

$$G" = \frac{\tau_0}{\gamma_0}\sin(\delta) \tag{S9.1.2}$$

Here, *G'* is the storage modulus, *G"* is the loss modulus, τ_0 is the applied stress, γ_0 is the applied strain, and δ is the phase angle. Materials which are more solid-like will elicit relatively higher levels of *G'* compared to *G"*. Thus, the proportion of viscosity that is governed by in-phase (elastic) and out-of-phase (viscous) forces can be calculated using Equations (S9.1.3)-(S9.1.5) [1].

$$\eta' = \frac{G"}{\omega} \tag{S9.1.3}$$

$$\eta" = \frac{G'}{\omega} \tag{S9.1.4}$$

$$|\eta^*| = \sqrt{\eta'^2 + \eta"^2} \tag{S9.1.5}$$

η' is the dynamic viscosity, $\eta"$ is the out-of-phase component of complex viscosity, and η^* is the complex viscosity. The ratio of storage to loss modulus can be used as well to determine the relative levels of solidity and fluidity, as determined by the loss tangent in Equation (S9.1.6) [1].

$$\tan(\delta) = \frac{G"}{G'} \tag{S9.1.6}$$

The closer δ is to 0°, the more solid-like the material is. Conversely, δ=90° suggests that the material is entirely fluidic. The two parameters analyzed for these experiments were η^* and $\tan(\delta)$ since they most readily describe the solidity of a material.

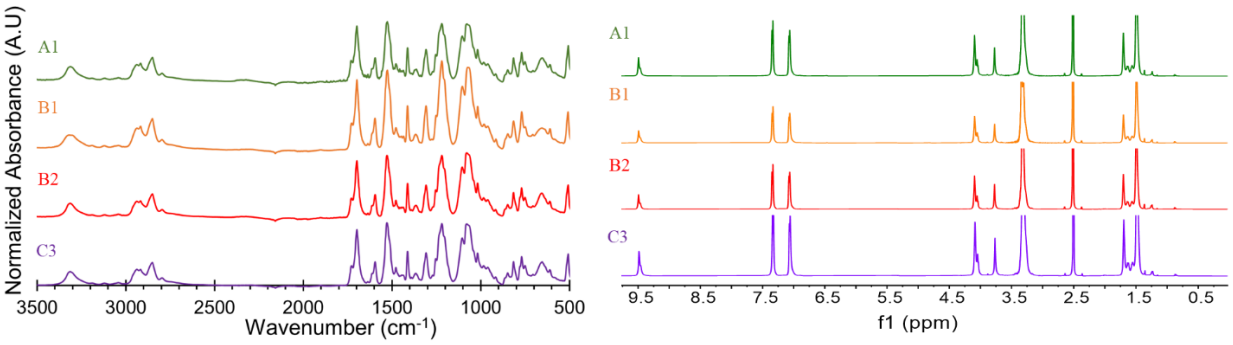

Figure S9.1.1: (Left) FTIR of four individual lots of TPU and (Right) subsequent ^{1}H-NMR of each lot.

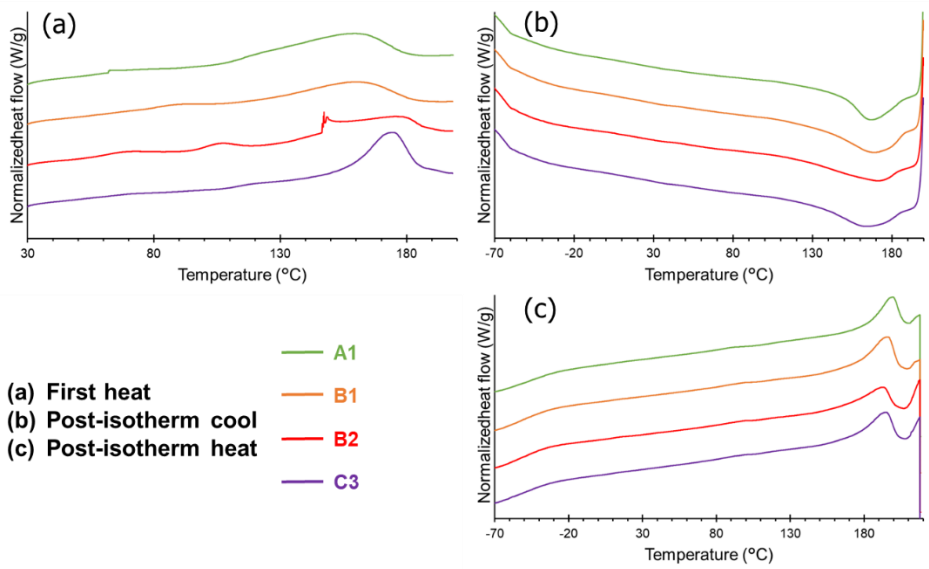

Figure S9.1.2: Heat-cool-heat DSC diagrams of four individual lots of TPU. (a) First heat, (b) cool, and (c) second heat procedures were performed on TPU pellets as received (endotherm in the positive direction).

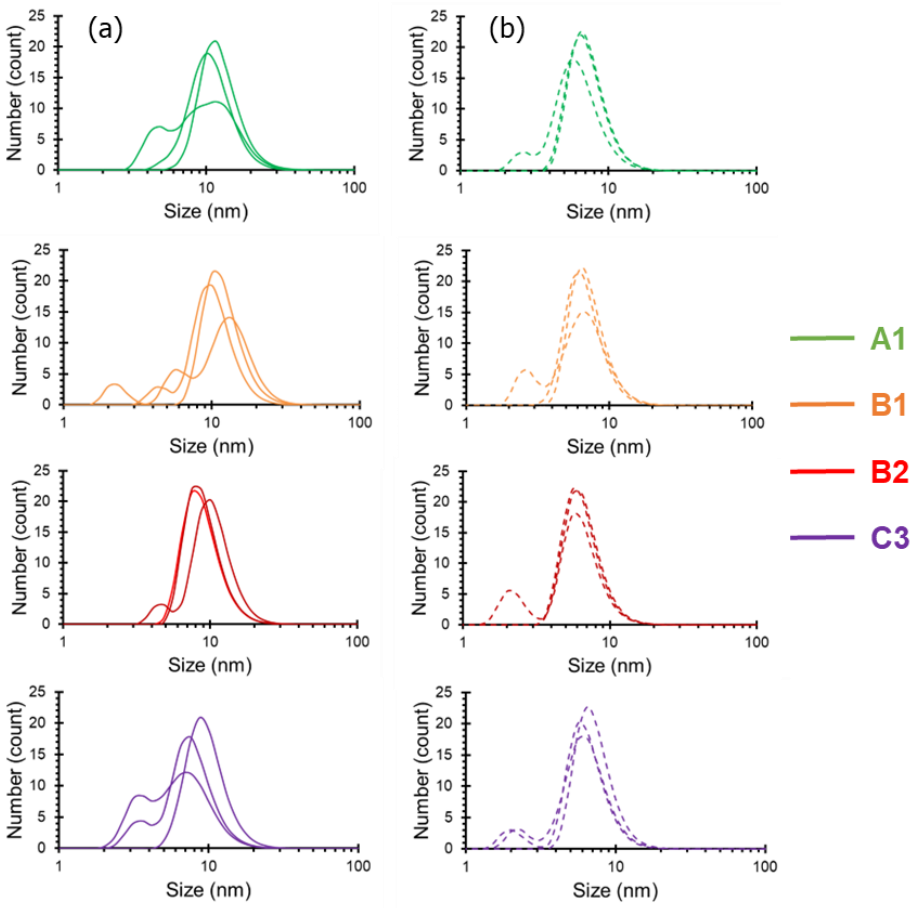

Figure S9.1.3: Dynamic light scattering studies of four lots of TPU (a) before and (b) after melt pressing at 5000 psi and 205 ºC.

9.1.1 References

[1] F.A. Morrison, Understanding rheology, Oxford university press New York 2001.

9.2 Supplementary Information: Chapter 4

Sestak-Berggren Equation

Beginning with the Prout-Tompkins method in Equation (S9.2.1), a common model-based approach to fitting curing/crosslinking reactions, the log term can be neglected on a system-dependent basis, which simplifies to Equation (S9.2.2): the Sestak-Berggren model [1]. Elimination of the log term reduces the complexity of the model, easing interpretation of parameters, and fits our system sufficiently well according to Figure S9.2.1.

$$\frac{d\alpha}{dt} = Ae^{\left(-\frac{E_a}{RT}\right)}\alpha^m(1-\alpha)^n(-\log(1-\alpha)^p) \quad \text{(S9.2.1)}$$

$$\frac{d\alpha}{dt} = Ae^{\left(-\frac{E_a}{RT}\right)}\alpha^m(1-\alpha)^n \quad \text{(S9.2.2)}$$

A is the pre-exponential factor, E_a is activation energy, and finally *m* and *n* are reaction orders. As shown in the main document with the Kamal-Sourour model, using a purely non-linear fitting approach without any rationale for initial guesses can incorrectly assume values of some parameters. For this reason, we approximate the value of activation energy by evaluating the slope of ln(*dα/dt*) as a function of the inverse of temperature at a low conversion. From here, the exponential term is known at each temperature, and non-linear fitting can be used to determine the reaction orders and pre-exponential factor [2]. Reaction rate as a function of conversion fit with the Sestak-Berggren equation can be found in Figure S9.2.1, with the parameters explicitly stated in Table S9.2.1.

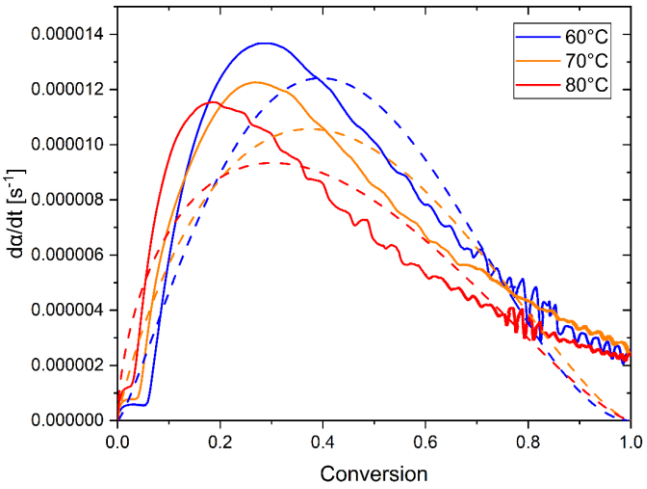

Figure S9.2.1: Reaction rate as a function of conversion, shown in solid lines (—) compared to the Sestak-Berggren equation, shown in dashed lines (- -).

Table S9.2.1: Parameters derived from the Sestak-Berggren equation. Note that activation energy is not temperature dependent according to the Arrhenius relationship.

Temperature [°C]	$A \times 10^5$ [s^{-1}]	E_a [kJ mol^{-1}]	m	n	r^2
60	7.04	34.1	1.28	1.95	0.86
70	4.31	34.1	0.87	1.46	0.84
80	4.03	34.1	0.60	1.38	0.79

The results of the Sestak-Berggren equation are remarkably similar to the Kamal-Sourour model. Sestak previously compiled a table of potential reaction orders, along with brief interpretations for each case [3]. For this case of apparently random reaction orders, the reaction is “arbitrary”, though some authors suggest that *m* can be a good descriptor of the intensity of the autocatalytic process [1]. As discussed in the main section of the text, the autocatalytic effect decreases with increasing temperature. Here, the intensity of autocatalysis *m* decreases with

temperature, which provides further evidence of a diminishing autocatalytic effect when temperature rises.

Conversion as a Function of Time Comparisons

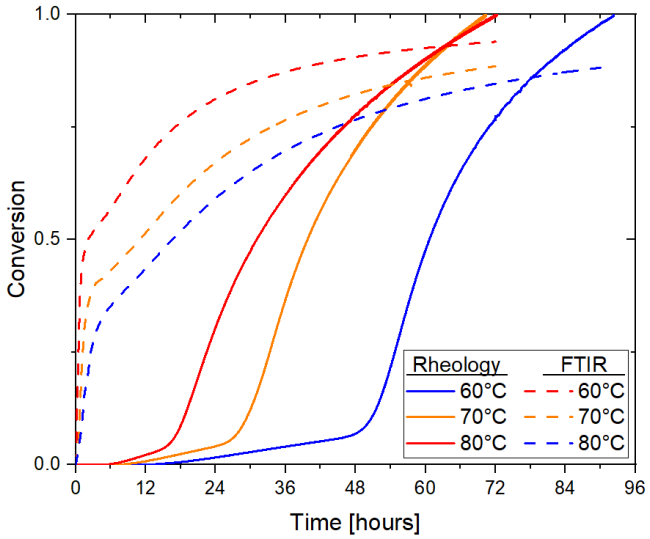

Figure S9.2.2: Conversion progress as a function of time comparing chemorheology and FTIR results.

Wynne-Jones-Eyring-Evans Plots

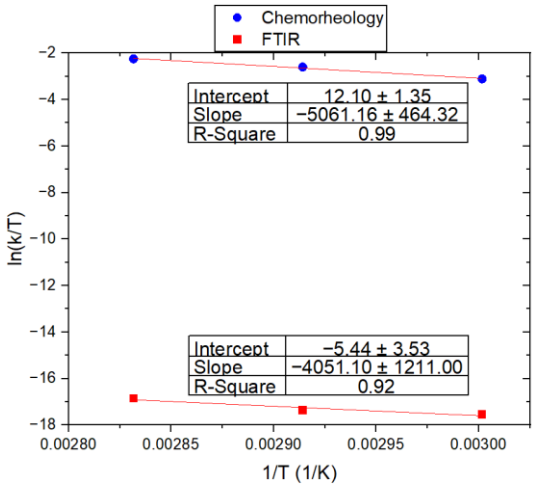

Figure S9.2.3: Wynne-Jones-Eyring-Evans theory plots for transition state analysis.

9.2.1 References

[1] A. Olejnik, K. Gosz, Ł. Piszczyk, Kinetics of cross-linking processes of fast-curing polyurethane system, Thermochim. Acta 683 (2020) 178435. https://doi.org/10.1016/j.tca.2019.178435.
[2] O. Yuksel, M. Sandberg, I. Baran, N. Ersoy, J.H. Hattel, R. Akkerman, Material characterization of a pultrusion specific and highly reactive polyurethane resin system: Elastic modulus, rheology, and reaction kinetics, Composites, Part B 207 (2021) 108543. https://doi.org/10.1016/j.compositesb.2020.108543.
[3] J. Šesták, Šesták–Berggren equation: now questioned but formerly celebrated—what is right, J. Therm. Anal. Calorim. 127 (2017) 1117-1123. https://doi.org/10.1007/s10973-015-4998-x.

9.3 Supplementary Information: Chapter 5

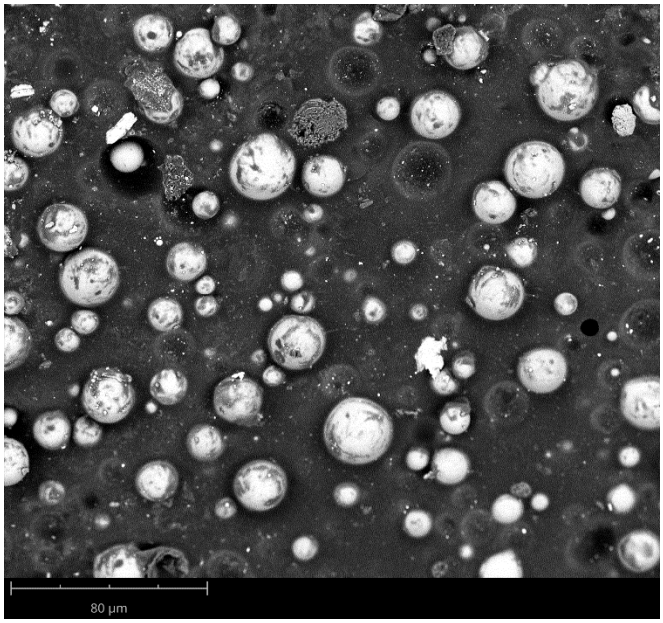

Figure S9.3.1: Scanning electron microscopy image of the lowest vol% ink post-mixing, indicating that the iM30k glass fillers remained intact.

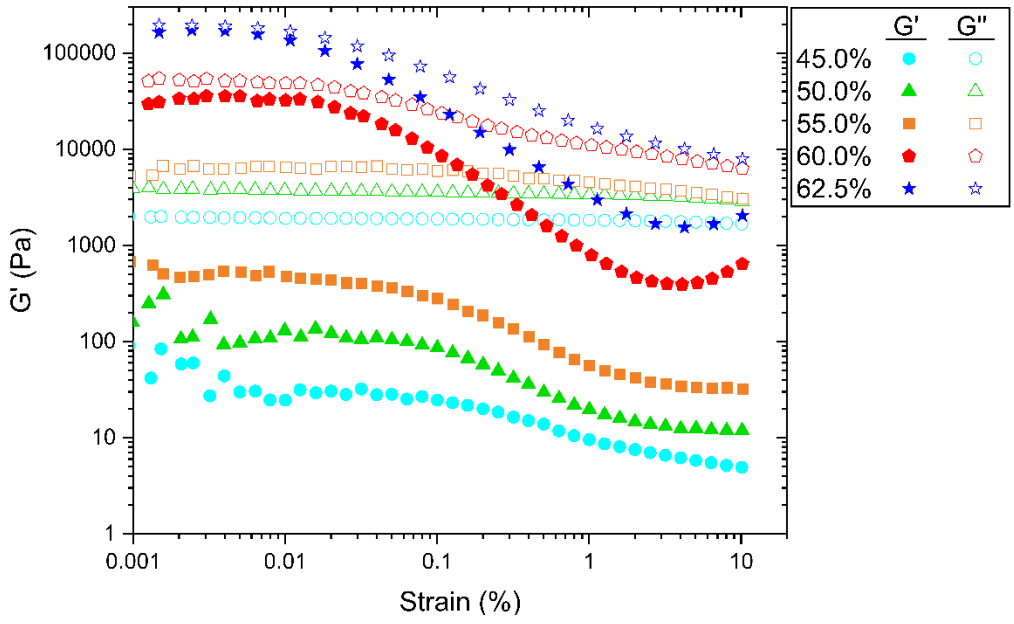

Figure S9.3.2: Storage modulus (filled shapes) and loss modulus (unfilled shapes) during strain sweeps of each ink at a given concentration.

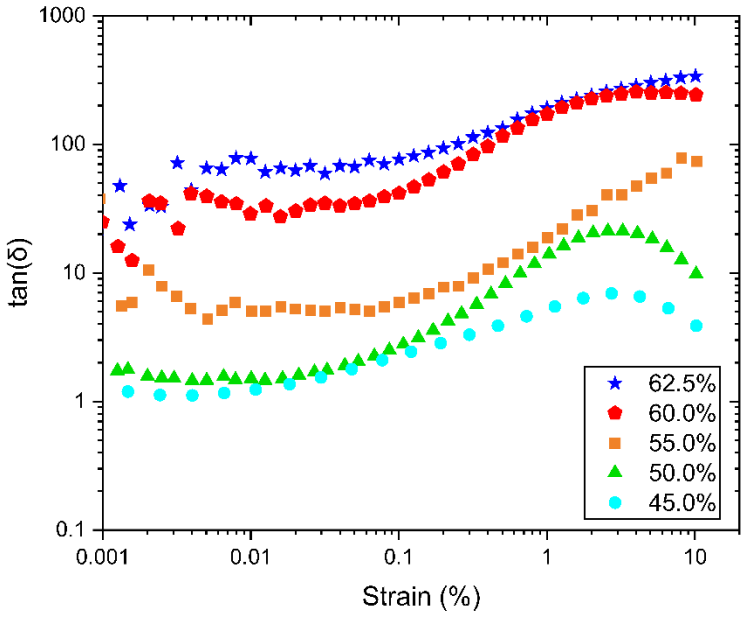

Figure S9.3.3: Loss tangent of each ink for a given concentration during strain sweeps.

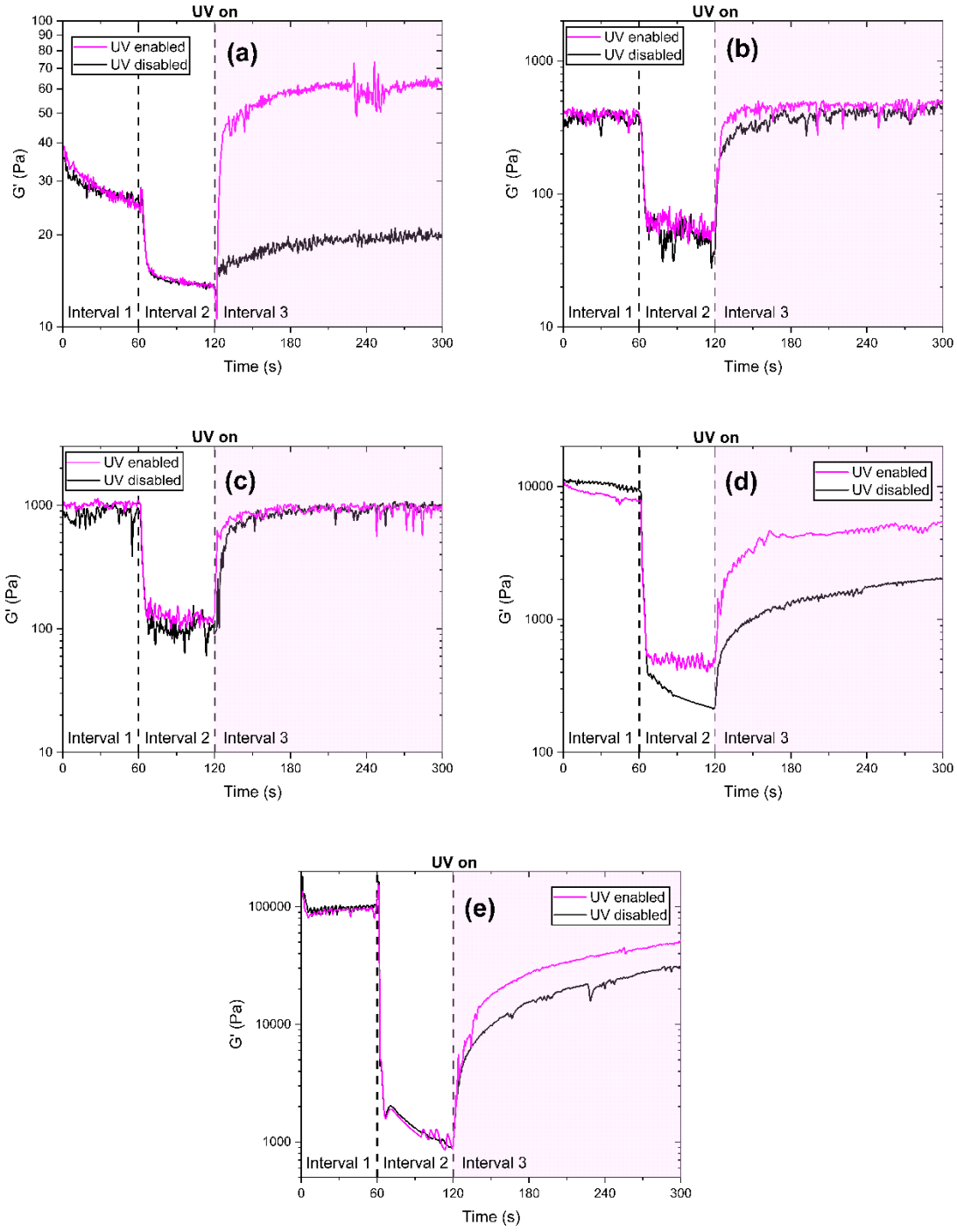

Figure S9.3.4: Examples of UV-3ITT experiments for (a) 45 vol%, (b) 50 vol%, (c) 55 vol%, (d) 60 vol%, and (e) 62.5 vol% inks. Note the difference in scale of the Y-axis for each plot.

9.4 Supplementary Information: Chapter 6

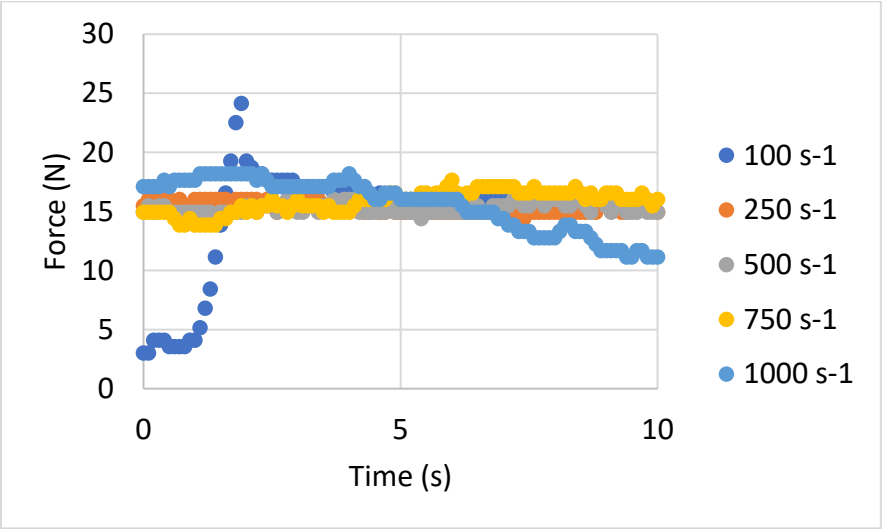

Figure S9.4.1: Frictional force as a function of time for different shear rates. Some variation was apparent near the start and end of the syringe barrel. To avoid these errors, testing was not conducted within 0.5 in of each end.